

**Ensuring the *in vitro* degradation
reproducibility of powder metallurgy
processed Mg-0.6Ca system**

Thesis submitted towards fulfilment of the requirements
for the degree of
Doctor of Philosophy (Dr. -Ing.)
At Technical Faculty
University of Kiel

Thesis submitted
by
Eshwara Phani Shubhakar Nidadavolu
Kiel, 2021

First reviewer: Prof. Regine Willumeit-Römer

Second reviewer: Prof. Mikhail Zheludkevich

Date of the examination: 23.08.2021

Abstract

Magnesium degradation is a complex phenomenon that is too difficult to be described by a single influential parameter. Magnesium degradation is often influenced by either overtaking or overlapping factors like the cell culture medium composition, physiological conditions, impurities, and material's internal microstructure, etc. This poses a challenge in obtaining the reproducible degradation results. Hence, in the present work, microstructural features like porosity and grain size distributions in powder metallurgy (PM) Mg-0.6Ca system were discretely evaluated for their roles in altering the specimen *in vitro* degradation rates. Importance was also given to the specimen impurity and mechanical properties. Based on the results, the limitations in PM processing conditions towards obtaining robust degradation results or, in other words, the material parameter thresholds to be realized for obtaining reproducible degradation profiles in PM Mg-0.6Ca specimens were put forth. Additionally, using literature evidence, the mechanisms governing pore closure and grain growth during liquid phase sintering of Mg-0.6Ca specimens from the PM processing perspective were determined.

PM Mg-0.6Ca specimens were fabricated via powder blending of pure magnesium and master alloy Mg-10Ca powders. Specimens of seven different porosities, from 3% to 21%, were produced by varying sintering temperatures. Specimens with heterogeneous grain size distributions were obtained by surface modification of pure magnesium powders by means of a mechanical sieving treatment. Degradation profiles were analyzed *in vitro* using a semi static immersion test for 16 days under physiological conditions of 37 °C, 20% O₂, 5% CO₂, 95% relative humidity. Dulbecco's modified Eagle's medium was used as cell culture medium with Glutamax and 10% fetal bovine serum as supplements. Mechanical properties were determined using micro tensile specimens. The results indicate that low mean degradation rates (MDR < 0.3 mm/year) with homogeneous and reproducible degradation are obtainable in PM Mg-0.6Ca specimens up to 10% porosity. The specimen porosity threshold to ensure degradation reproducibility is 12%, however, at the expense of an increased MDR (1.6 mm/year). μ CT characterized 12% as the transition porosity, where the specimen surface open pore fraction drops from > 95% to \leq 45% when falling below this value. Similarly, the pore interconnectivity sharply drops from > 95% to < 10% at this porosity, thereby enhancing the degradation reproducibility. From PM processing perspective, the sintering temperature of 570 °C is proven as beneficial to promote liquid fractions high enough to enhance specimen sinter density. The present work also showed that heterogeneous grain growth is prompted by the reduced oxide pinning effect at the grain boundaries during sintering of PM Mg-0.6Ca specimens. The heterogeneous grain growth additionally induced the formation of eutectic lamellar structure α -Mg + Mg₂Ca at certain grain boundaries throughout the microstructure, which is otherwise not evident in specimens with a homogeneous grain size. Based on the literature and results of the present work, it is postulated that this eutectic structure is the major reason for a non-reproducible degradation in PM Mg-0.6Ca specimens possessing a heterogeneous grain structure. Though mechanical properties are not majorly affected, it is recommended that heterogeneous grain growth is to be avoided in PM Mg-0.6Ca specimens. The presented results also implicitly conveyed the flexibility of PM as a viable technique to design Mg-Ca materials with tailor made degradation and mechanical strengths.

Zusammenfassung

Die Degradation von Magnesium ist ein Phänomen, welches zu komplex ist, um es mit nur einem Parameter zu beschreiben. Sie wird häufig von sich überlappenden oder gegenseitig beeinflussenden Faktoren wie z.B. der Zusammensetzung der Zellkultur beim biologischen Test, den physiologischen Bedingungen, Verunreinigungen, der Mikrostruktur des Materials usw. beeinflusst. Dies führt zu der Herausforderung, trotz der Komplexität reproduzierbare Ergebnisse in der Degradation zu erreichen. Daher wurden in der vorliegenden Arbeit mikrostrukturelle Eigenschaften, wie Porosität und Korngröße im pulvermetallurgischen (PM) Mg-0.6Ca System, einzeln in Bezug auf ihren Einfluss auf die *in vitro* Degradationsraten von Proben ausgewertet. Des Weiteren wurde ein besonderes Augenmerk auf Verunreinigungen und mechanische Eigenschaften der Proben gelegt. Auf Basis der Ergebnisse wurden die Grenzen der Bedingungen bei der PM Prozessierung in Bezug auf stabile Degradationsergebnisse erarbeitet oder, in anderen Worten, es wurden die Materialparametergrenzen, welche für wiederholbare Degradationsprofile im PM Mg-0.6Ca Proben gelten, aufgedeckt. Außerdem wurden die Mechanismen, welche für das Schließen der Poren und das Kornwachstum während des Flüssigphasensinterns von Mg-0.6Ca verantwortlich sind, unter Einbeziehung von Literaturnachweisen ermittelt.

Die PM Mg-0.6Ca Proben wurden durch Pulvermischen von reinem Magnesium- und Masterlegierungspulver (Mg-10Ca) hergestellt. Proben mit sieben verschiedenen Porositätswerten von 3% bis 21% wurden durch Anpassen der Sintertemperatur hergestellt. Proben mit heterogener Korngrößenverteilung wurden durch eine Oberflächenmodifikation von reinem Magnesiumpulver erzielt, die auf einem mechanischen Siebprozess beruhte. Degradationsprofile wurden *in vitro* in einem 16-tägigen semistatischen Immersionstest unter physiologischen Bedingungen von 37°C, 20% O₂, 5% CO₂ und 95% relativer Luftfeuchtigkeit analysiert. Als Zellkulturmedium wurde Dulbecco's Modified Eagle's Medium mit den Zusätzen Glutamax und 10% fötalem Kälberserum verwendet. Mechanische Eigenschaften wurden an Mikroflachzugproben bestimmt. Die Ergebnisse zeigen, dass niedrige mittlere Degradationsraten (MDR < 0,3 mm/Jahr) mit gleichmäßiger und reproduzierbarer Degradation bis zu einer Porosität von 10% bei PM Mg-0.6Ca Proben erzielt werden können. Der Grenzwert für die Porosität der Proben, bis zu dem eine reproduzierbare Degradation sichergestellt werden kann, liegt bei 12%, wobei dies zu Lasten einer erhöhten MDR von 1,6 mm/ Jahr geht. μ CT Messungen charakterisieren 12% als die Übergangsporosität, bei deren Unterschreitung der Anteil der Oberfläche der offenen Porosität von > 95% auf \leq 45% fällt. Gleichzeitig sinkt die Interkonnektivität der Poren drastisch von > 95% auf < 10% bei diesem Wert, was zu einer Verbesserung der Reproduzierbarkeit der Degradation führt. Aus Sicht der PM Prozessierung ist eine Sintertemperatur von 570 °C von Vorteil, bei der ein höheren Flüssigphasenanteil erzielt wird, welcher zu einer höheren Sinterdichte führt. Die vorliegende Arbeit zeigt außerdem, dass ein ungleichmäßiges Kornwachstum durch einen reduzierten Pinning-Effekt der Oxide an den Korngrenzen während des Sinterns von Mg-0.6Ca verursacht wird. Das ungleichmäßige Kornwachstum führt außerdem zu der Bildung der eutektischen lamellaren Struktur α -Mg + Mg₂Ca an bestimmten Korngrenzen entlang der gesamten Mikrostruktur, welche ansonsten nicht für Proben mit einer gleichmäßigen Korngröße von ca. 30 μ m nachgewiesen wurde. Auf Basis der Literatur und Ergebnissen dieser Arbeit wird vermutet, dass diese eutektische Struktur die Hauptursache für eine nicht reproduzierbare Degradation in PM Mg-0.6Ca Proben mit heterogener Mikrostruktur ist. Obwohl die

mechanischen Eigenschaften nicht wesentlich beeinflusst werden, sollte ein heterogenes Kornwachstum vermieden werden, um eine reproduzierbare Degradation in PM Mg-0.6Ca Proben sicherzustellen. Die vorliegenden Ergebnisse zeigen die Flexibilität von PM als aktuelle Technik, um Mg-Ca Materialien mit maßgeschneiderter Degradation und mechanischer Festigkeit herzustellen.

Declaration

I hereby declare that all content and the design of this thesis is the result of my own work, apart from the guidance provided by the supervisors, and was completed with authorized assistance. No other literature sources apart from the references listed were used.

The presented results, either in whole or in part, have never been submitted to another research body as part of a doctoral examination procedure, apart from the list of publications indicated in the section of this thesis. I also declare that I have no previous attempts at Doctoral degrees in other research bodies.

In addition, the research work was carried out in compliance with good scientific practices stipulated by the German Research Foundation.

I state that none of my previous academic degrees has been revoked.

(City, Date)

Eshwara P.S. Nidadavolu

Acknowledgements

I express my sincere gratitude to my supervisors Prof. Dr. Regine Willumeit-Römer, Dr. Thomas Ebel and Dr. Frank Feyerabend for providing me with an opportunity to work in their interdisciplinary research institute Metallic biomaterials at Helmholtz-Zentrum Geesthacht. Their pleasing demeanor and encouragement played a very crucial role in the successful completion of my research project. The research leading to these results has partly received funding from the Helmholtz Virtual Institute “*In vivo* studies of biodegradable magnesium-based implant materials (MetBioMat)” under grant agreement no. VH-VI-523. My special acknowledgements to Prof. Dr. Regine Willumeit-Römer for the extended funding in the form of institute’s internal budget.

I profusely thank Prof. Dr. Michael Dahms, Fachhochschule Flensburg, for his foundational guidance and motivation towards pursuing my PhD work in magnesium powder metallurgy. I extend my sincere thanks to Dr. Johannes Geronimo Schaper, Ms. Diana Krüger, Dr. Björn Wiese, Dr. Berit Zeller-Plumhoff, Dr. Domonkos Tolnai for their timely guidance with experimentation, results validation and importantly, the scientific discussions. Their contribution in the form of time they catered to the needs of my research work is highly acknowledged.

I highly regard my colleagues Mr. Martin Wolff, Mr. Wolfgang Limberg and Dr. Vasyl Mikhailovich Haramus for helping me mold my ideas and lending a supportive hand in the experimental works. I profusely thank Dr. Bérengère Luthringer-Feyerabend (Head, Department of biological characterization, HZG), Dr. Thomas Emmeler (Scientist, Department of polymer synthesis, HZG), Dr. Mikhail Zheludkevich (Head, Department of corrosion and surface technology, HZG), Dr. Norbert Hort (Acting director of the institute magnesium innovation centre, HZG) and Dr. Dietmar Letzig (Head, Department of Wrought magnesium alloys, HZG) for allowing me to perform experiments on their state of the art laboratory devices. I would like to acknowledge all laboratory technical personnel: Ms. Anke Schuster, Ms. Monika Luczak, Ms. Petra Fischer, Mr. Gert Wiese, Mr. Andreas Dobernowsky, Mr. Kai Steinberg, Mr. Nils Holländer, Mr. Daniel Strerath, Ms. Sabine Schubert, Ms. Angela Meyer-Rachner for their expertise in material handling and characterization techniques.

To all my present and former colleagues for providing a peaceful working atmosphere during my PhD. My heartfelt gratitude to my parents Ms. Aruna Sai Nidadavolu and Mr. Satya Sai Nidadavolu for their positivity and blessings and my brother Mr. Gnana Sreekar Nidadavolu for his continuous support. Finally, my deepest regards to my friends Ms. Lea Heinelt, Ms. Gowthami Pypalli, Dr. Sarkis Gavras, Dr. Nowfal Al-Hamdany, Mr. Vasilis Merziotis, Ms. Irene Provia for their constant understanding and support during stressful occasions of both my professional and personal endeavors.

List of Publications

- Eshwara Phani Shubhakar Nidadavolu, Diana Krüger, Berit Zeller-Plumhoff, Domonkos Tolnai, Björn Wiese, Frank Feyerabend, Thomas Ebel, Regine Willumeit-Römer, Pore characterization of PM Mg-0.6Ca alloy and its degradation behaviour under physiological conditions, Journal of Magnesium and Alloys (online, June 2020). <https://doi.org/10.1016/j.jima.2020.05.006>
- Jorge Gonzalez, Rui Qing Hou, Eshwara P.S. Nidadavolu, Regine Willumeit-Römer, Frank Feyerabend, Magnesium degradation under physiological conditions-Best practice, Bioactive Materials 2018 (3)2: p. 174. <https://doi.org/10.1016/j.bioactmat.2018.01.003>
- Eshwara Phani Shubhakar Nidadavolu, Frank Feyerabend, Thomas Ebel, Regine Willumeit-Römer, Michael Dahms, Degradation behaviour of as cast and powder metallurgy processed Mg-Ca alloys, Journal of Medical Materials and Technologies 2017 (1)2, p. 18: Proceedings of Euro BioMAT. <https://doi.org/10.24354/medmat.v1i2.19>
- Nidadavolu EPS, Feyerabend F, Ebel T, Willumeit-Römer R, Dahms M, On the determination of Magnesium degradation rates under physiological conditions, Materials 2016 (9)8: p. 627. [10.3390/ma9080627](https://doi.org/10.3390/ma9080627)

Contents

Abstract.....	I
Zusammenfassung	II
Declaration.....	IV
Acknowledgements	V
List of Publications	VI
Contents.....	VII
List of Tables	IX
List of Figures	X
Abbreviations.....	XIV
1 INTRODUCTION	1
2 STATE OF THE ART	3
2.1 Sintering of Mg.....	3
2.1.1 Calcium as an aid for magnesium sintering.....	3
2.1.2 Sintering atmosphere	4
2.2 Liquid phase sintering	6
2.2.1 Mg-Ca phase diagram	7
2.2.2 Evolution of liquid phase mass fraction with sintering temperature.....	8
2.2.3 Variation in density with sintering time and temperature.....	9
2.2.4 Grain growth	11
2.3 Mg in biomedical implant framework	13
2.3.1 Mg-Ca alloys.....	13
2.3.2 Magnesium degradation.....	14
2.3.3 Determination of mean degradation rate in Mg alloys.....	16
2.4 Critical factors affecting Mg degradation	18
2.4.1 Impurity concentrations	18
2.4.2 Porosity and pore features	20
2.4.3 Effects of grain size	22
3 AIMS OF THE EXPERIMENTS	25
4 EXPERIMENTAL	27
4.1 Powder metallurgy.....	27
4.1.1 Raw materials.....	27
4.1.2 PM Mg-0.6Ca powder mix preparation	28
4.1.3 Mechanical sieving treatment of as received pure Mg powder.....	29
4.1.4 PM Mg-0.6Ca green compacts preparation.....	29
4.1.5 Sintering process.....	30
4.2 Density and porosity measurements.....	31
4.3 Elemental composition analysis.....	33
4.4 Microscopy analysis	35

4.5	Computer tomography analysis.....	37
4.6	<i>In vitro</i> degradation testing	41
4.6.1	Specimen cleaning and sterilization	41
4.6.2	Semi static immersion test	42
4.6.3	Medium extract analysis.....	44
4.7	Mechanical property testing.....	44
5	RESULTS.....	46
5.1	Chemical analysis of PM Mg-0.6Ca specimens.....	46
5.2	Density development with sintering temperature.....	47
5.3	Microstructures of PM Mg-0.6Ca (Mg/Mg-10Ca).....	49
5.4	Tomography evaluation of PM Mg-0.6Ca (Mg/Mg-10Ca).....	53
5.5	Heterogeneous grain structures in Mg-0.6Ca (Mg _{sieved} /Mg-10Ca).....	59
5.6	Factors potentially affecting heterogeneous grain growth.....	64
5.6.1	Pure Mg powder surface morphology	64
5.6.2	Sintering time.....	66
5.6.3	Master alloy powder particle size.....	68
5.7	Semi static immersion test	69
5.7.1	Effect of porosity on PM Mg-0.6Ca specimen degradation	69
5.7.2	Effect of heterogeneous grain structure on Mg-0.6Ca specimen degradation..	73
5.8	Mechanical properties of PM Mg-0.6Ca.....	74
5.8.1	Dependence on Mg-0.6Ca specimen porosity.....	74
5.8.2	Dependence on Mg-0.6Ca specimen grain structure	76
6	DISCUSSION.....	77
6.1	Effective liquid phase mass fraction for pore closure	77
6.2	Influence of pore features on PM Mg-0.6Ca degradation.....	79
6.2.1	Surface open pore fraction and pore interconnectivity	79
6.2.2	Pore shape and pore size distribution	82
6.3	Generalized criterion for degradation reproducibility in view of magnesium material porosity.....	83
6.4	Surface oxide and grain boundary pinning effects in PM Mg-0.6Ca	84
6.5	Effect of heterogeneous grain structure on PM Mg-0.6Ca degradation.....	87
6.6	Degradation reproducibility in relation to grain size of PM Mg materials.....	90
6.7	Strength profiles of PM Mg-0.6Ca in relation to microstructure	91
6.8	Basic suitability of PM Mg-0.6Ca as bone implant material.....	92
7	CONCLUSIONS.....	94
	Outlook	95
	References	96

List of Tables

Table 1: Typical equilibrium potential values of common engineering metals in aqueous solutions [88].	15
Table 2: Brief overview of the development of porous magnesium materials using various production techniques.	20
Table 3: Elemental composition of the raw powders used in PM processing of Mg-0.6Ca specimens.	27
Table 4: Calcium and impurity element concentrations ($n= 3/\text{category}$) of Mg-0.6Ca (Mg/Mg-10Ca) and Mg-0.6Ca ($\text{Mg}_{\text{sieved}}/\text{Mg-10Ca}$) specimens in their sintered condition.	46
Table 5: Quantitative pore parameters obtained from three different μCT volumes (each of $700\ \mu\text{m} \times 700\ \mu\text{m} \times 500\ \mu\text{m}$) of porous Mg-0.6Ca (Mg/Mg-10Ca) specimens sintered at different temperatures.	53
Table 6: Sintering time for onset of heterogenous grain growth in porous Mg-0.6Ca ($\text{Mg}_{\text{sieved}}/\text{Mg-10Ca}$) specimens when sintered at $627\ ^\circ\text{C}$ under argon atmosphere.	67
Table 7: Linear regression fit parameters obtained from the degradation profiles of porous Mg-0.6Ca specimens (Mg/Mg-10Ca) specimens.	70
Table 8: Linear regression fit parameters obtained from the degradation profiles of Mg-0.6Ca ($\text{Mg}_{\text{sieved}}/\text{Mg-10Ca}$) specimens compared to Mg-0.6Ca (Mg/Mg-10Ca) specimens.	73
Table 9: Tensile strength and elongation to fracture values ($n= 5$) recorded for Mg-0.6Ca (Mg/Mg-10Ca) specimens with varying porosities in their sintered condition prior to immersion degradation test.	75

List of Figures

- Figure 2-1: Schematic of the crucible setup designed for successful magnesium sintering by Wolff et al. [32]. Specimens in crucible number 1 sinter superior compared to the specimens in crucible number 2. With permissions to reprint from WILEY-VCH Verlag GmbH.....4
- Figure 2-2: (A) Point contact between magnesium particles after sintering that are free from oxygen getter material. (B) Sinter neck formation between magnesium particles when surrounded by oxygen getter material [32]. With permissions to reprint from WILEY-VCH Verlag GmbH.....5
- Figure 2-3: Schematic illustration of different stages involved in liquid phase sintering based on [41].6
- Figure 2-4: Calculated Mg-Ca phase diagram using PanMagnesium 8 database [13].7
- Figure 2-5: Magnesium rich side of Mg-Ca equilibrium phase diagram showing isothermal lines at different sintering temperatures above the eutectic temperature of 516 °C. ..8
- Figure 2-6: (A) Increase in relative sinter density with increasing sintering time in alumina-glass liquid phase sintering with varying initial particle sizes [44]. With permissions to reprint from WILEY-VCH Verlag GmbH. (B) W-Ni-Fe alloy system densification until reaching liquid phase sintering temperature and during isothermal holding period [45]. With permissions to reprint from the Minerals, Metals & Materials Society and ASM International.10
- Figure 2-7: (A) Schematics of macro and micro galvanic corrosion in magnesium alloys in presence of other metals and secondary phases within the magnesium matrix [86]. With permissions to reprint from WILEY-VCH Verlag GmbH. (B) Influence of different commercial elements on degradation rate of magnesium alloys [89, 90]. With permissions from Elsevier.15
- Figure 2-8: (A) Schematic of possible degrading scenarios shown via mass loss vs time curves for a degrading magnesium alloy and (B) Degradation profile for Mg-2Ag immersed in DMEM + 10% FBS cell culture medium where blue triangles represent degradation rates measured according to ASTM equation and blue line is the regression fit for the experimental red points [11].....17
- Figure 4-1: Raw powders used in the study. (A) Gas atomized pure magnesium powder with near spherical morphology (B) Mg-10Ca master alloy powder with spherical to ellipsoid morphology. Both powders exhibit fine satellite particles attached to their surfaces. Occasionally powder clusters could be seen.27
- Figure 4-2: Schematic of the vibratory mechanical sieve shaker used for sieving pure magnesium powders in the present study.....29
- Figure 4-3: Representative compacts of compressive (immersion test) and microtensile test geometries of PM Mg-0.6Ca specimens. (A) After uni-axial hand pressing prior to sintering. (B) After sintering. The microtensile specimen shown in (B) is cut out from a thicker sintered part and, therefore, does not directly relate to the green part shown in (A).30
- Figure 4-4: Schematic of sintering setup for PM Mg-0.6Ca specimens illustrating basic parts of the crucible.....30
- Figure 4-5: Schematic of sintering runs employed to generate porosity in PM Mg-0.6Ca specimens.....31

- Figure 4-8: Representative microstructure of a sintered Mg-0.6Ca (Mg/Mg-10Ca) specimen possessing 3% porosity with (A) Hand marked grain boundaries and pores, (B) Thresholded image of the inset in (A); matrix (binary value 255), pores and grain boundaries (binary value 0) and (C) Grain areas analyzed using software Fiji [162]. Arrow indicates a pore that has been hand marked in (A) and segmented (B) but not interpreted as a grain during the grain size analysis in (C).37
- Figure 4-9: Representative μ CT slice/image pertaining to Mg-0.6Ca (Mg/Mg-10Ca) specimen with 12% porosity (A) After reconstruction, (B) After 3D median filtering and (C) After thresholding where the pores are shown in white (binary value 255) and matrix in black (binary value 0).38
- Figure 4-10: Representative shape descriptors that can be assessed from the combined mean and Gaussian curvature values [167]. With permissions from Elsevier.....39
- Figure 4-11: Process flow routine employed in Avizo[®] 9.3.0 software to analyze the pore curvatures and 3D pore structures in Mg-0.6Ca (Mg/Mg10Ca) specimens.40
- Figure 4-12: Schematic of ultrasonic cleaning procedure for Mg-0.6Ca specimens used in the present work.42
- Figure 4-13: Schematic of immersion degradation test setup for Mg-0.6Ca specimens used in the present work.42
- Figure 4-14: Flow sheet of immersion degradation test used for Mg-0.6Ca specimens in the present work.43
- Figure 5-1: (A) Relative density change before and after sintering of porous Mg-0.6Ca (Mg/Mg-10Ca) specimens as a function of sintering temperature. (B) Comparison of relative sinter densities between pure magnesium reference specimens and Mg-0.6Ca (Mg/Mg-10Ca) specimens under same sintering conditions. Arrow in (A) indicates the sharp increase in specimen density after sintering at 570 °C.48
- Figure 5-2: Fraction of closed pores formed and specimen porosity change as a function of sintering temperature in porous Mg-0.6Ca (Mg/Mg-10Ca) specimens. Arrow indicates the sharp increase in the closed pore fraction at 570 °C.49
- Figure 5-3: Representative optical images of sintered Mg-0.6Ca (Mg/Mg-10Ca) specimens with porosities of (A) 21%, (B) 18%, (C) 12%, (D) 10%, (E) 8%, (F) 6% and (G) 3%. Specimen sintering temperatures are mentioned in respective images.....50
- Figure 5-4: BSE images indicating the pore nature and phases formed in Mg-0.6Ca (Mg/Mg-10Ca) specimens with porosities of (A) 21%, (B) 12%, (C) 10% and (D) 3%. Specimen sintering temperatures are mentioned in respective images.....51
- Figure 5-5: BSE images of Mg-0.6Ca (Mg/Mg-10Ca) specimens 21%. White boxes indicate dense regions within the same cross section of the specimen.51
- Figure 5-6: Electron microscopy images of Mg-0.6Ca (Mg/Mg-10Ca) specimens with porosities of (A) 21%, (B) 12%, (C) 10% and (D) 3% indicating different phases formed with evolving pore morphology. Images are taken using BSE mode except for image (D), which is in SE mode.52
- Figure 5-7: Rendered 3D images of pores after image segmentation from similar μ CT volumes in Mg-0.6Ca (Mg/Mg-10Ca) specimens with (A) 21%, (C) 18%, (E) 12%, (G) 8% and (I) 3% porosity values. (B), (D), (F), (H) and (J) represent the 3D images of the largest pore detected in these specimens corresponding to the aforementioned porosity levels.....55
- Figure 5-8: Combined mean and Gaussian curvatures of pores after segmentation of similar μ CT volumes in Mg-0.6Ca (Mg/Mg-10Ca) specimens with (A) 21%, (C) 18%, (E) 12%,

- (G) 8% and (I) 3% porosity values. (B), (D), (F), (H) and (J) represent curvature distributions of the largest pore detected in these specimens corresponding to the aforementioned porosity levels. The shape descriptors corresponding to the signs of mean and Gaussian curvatures are shown in (A).....57
- Figure 5-9: (A) Normalized pore frequency as a function of pore diameter for porous Mg-0.6Ca (Mg/Mg-10Ca) specimens with cut off in pore diameter at 50 μm . (B) Normalized pore surface area of all segmented pores in porous Mg-0.6Ca (Mg/Mg-10Ca) specimens vs the actual pore diameters formed in these specimens.....58
- Figure 5-10: EBSD maps and grain size distribution of Mg-0.6Ca specimens produced using (A, B) (Mg/Mg-10Ca) powder mix and (C, D) ($\text{Mg}_{\text{sieved}}$ /Mg-10Ca) powder mix. Arrows in (D) indicate the grain sizes of the heterogeneously coarsened grains in (C).....60
- Figure 5-11: (A, B) BSE overview images and (C, D) Close up images of Mg-0.6Ca ($\text{Mg}_{\text{sieved}}$ /Mg-10Ca) specimens indicating different grain size regions and phases within the same specimen cross section after polishing.61
- Figure 5-12: Microstructural features of Mg-0.6Ca ($\text{Mg}_{\text{sieved}}$ /Mg-10Ca) specimens. (A) Overview image. (B, C) are inset pictures of (A) showing eutectic lamellar structures at certain boundaries of heterogeneously coarsened grains and the presence of Mg/Ca/Si and MgO phases, respectively.62
- Figure 5-13: EDX map of eutectic lamellar structure in Mg-0.6Ca ($\text{Mg}_{\text{sieved}}$ /Mg-10Ca) specimens. (A) Overview image. (B) Inset of figure (A) showing the eutectic lamellar α -Mg + Mg_2Ca along with Mg/Ca/Si phase. EDX maps of (B) are shown in the second row.....63
- Figure 5-14: EDX map at the site of Mg/Ca/Si phase along with a former particle boundary in heterogeneous grain structure of Mg-0.6Ca ($\text{Mg}_{\text{sieved}}$ /Mg-10Ca) specimens. (A) Overview image and (B) is the inset of figure (A). EDX maps are shown in the second row.....63
- Figure 5-15: Surface morphologies of gas atomized pure magnesium powders used in the study. (A-E) Secondary electron images indicating particulate and patch form of oxide surface. (F) Corresponding oxygen map for image (E) by EDX analysis.....65
- Figure 5-16: Secondary electron images of pure magnesium powders after mechanical sieving treatment used in the study. (A-E) Powder surface view indicating particulate oxide form. (F) Corresponding oxygen map of image (E) by EDX analysis.....66
- Figure 5-17: Optical microstructures of porous Mg-0.6Ca ($\text{Mg}_{\text{sieved}}$ /Mg-10Ca) specimens after sintering at 627 $^{\circ}\text{C}$ for different durations of (A) 3 h (B) 12 h and (C) 18 h under argon atmosphere. (D, E, F) BSE images of the specimen shown in image (C). Arrows in (F) show the eutectic lamellar structure of the inset in image (E).....68
- Figure 5-18: Microstructures of Mg-0.6Ca ($\text{Mg}_{\text{sieved}}$ /Mg-10Ca) specimens with pure magnesium (< 45 μm) blend with Mg-10Ca master alloy powder with varying sizes of (A, B, C) < 32 μm and (D, E, F) 180 – 250 μm . (A, D) Optical microscope images after etching treatment. (B, C, E, F) BSE images prior to etching. Arrows in (F) indicate a eutectic lamellar structure.68
- Figure 5-19: Degradation profiles of porous Mg-0.6Ca (Mg/Mg-10Ca) specimens obtained via semi static immersion test. Straight lines indicate linear regression fit for the experimental data. The specimen porosities are correspondingly shown to the right of the graph.69

- Figure 5-20: (A) Incremental change in the extract osmolality of degrading Mg-0.6Ca (Mg/Mg-10Ca) specimens with varying porosities during semi-static immersion test. (B) Variation in the mass of the formed degradation layer with immersion time. 71
- Figure 5-21: Degraded surface morphologies of Mg-0.6Ca (Mg/Mg-10Ca) specimens with varying porosities after chromic acid treatment at different immersion durations. ... 72
- Figure 5-22: Degradation profiles of Mg-0.6Ca (Mg_{sieved} /Mg-10Ca) specimens shown in violet obtained after 16-days immersion degradation test. Green line represents Mg-0.6Ca (Mg/Mg-10Ca) specimens with 3% porosity shown for comparison..... 73
- Figure 5-23: Variation in the mass of the formed degradation layer with immersion time of Mg-0.6Ca (Mg_{sieved} /Mg-10Ca) Mg-0.6Ca (Mg/Mg-10Ca) specimens with heterogeneous and homogeneous grain structures, respectively. 74
- Figure 5-24: (A) Representative tensile curves for Mg-0.6Ca (Mg/Mg-10Ca) with varying porosities. (B) UTS and elongation to fracture values in Mg-0.6Ca (Mg/Mg-10Ca) specimens as a function of porosity..... 75
- Figure 5-25: Mechanical properties of porous Mg-0.6Ca (Mg_{sieved} /Mg-10Ca) specimens with heterogeneous grain structure compared with Mg-0.6Ca (Mg/Mg-10Ca) specimens with homogeneous grain structure..... 76

Abbreviations

DMEM	Dulbecco's Modified Eagle's Medium
FBS	Fetal Bovine Serum
DNA	Deoxyribonucleic acid
RNA	Ribonucleic acid
AAS	Atomic absorption spectroscopy
AES	Atomic emission spectroscopy
MIM	Metal injection molding
HBSS	Hank's balanced salt solution
EBSD	Electron back scattered diffraction
CCD	Charged couple device
PMT	Photo multiplier tube
PI	Pore interconnectivity
K	Gaussian curvature
H	Mean curvature
SE	Secondary electron
BSE	Back scattered electron
EDX	Energy dispersive x – rays
LPS	Liquid phase sintering
PM	Powder metallurgy
AM	Additive manufacturing
MDD	Mean degradation depth
MDR	Mean degradation rate
ρ_{geo}	Geometric density
P_{spec}	Specimen porosity
ρ_{th}	Theoretical density
MgP	Magnesium phosphate
CaP	Calcium phosphate
ECAP	Equal channel angular processing
ASTM	American society for testing materials
Emf	Electro motive force
μ CT	Micro tomography
DR	Degradation rate
MAP	Master alloy powder
XPS	X-ray photoelectron spectroscopy

1 Introduction

Magnesium and its alloys have the capacity to completely degrade when exposed to biological media while showing appropriate biomechanical and biocompatibility properties as implant materials [1, 2]. This decreases the morbidity and health costs incurred through second surgeries that are generally associated with the conventionally used metallic implants like stainless steel, titanium and cobalt-chromium based materials [3]. The reliability of degradable implant materials, like magnesium alloys, for bone healing applications is primarily characterized by their homogeneous and low degradation rates when exposed to physiological body fluid environments combined with adequate mechanical properties [4]. In this regard, the chain of material processing may hugely alter the resultant microstructure and therefore the final desired material properties.

PM processing offers the benefits of near net shape part production and homogeneous microstructures. With their natural surface oxide, however, pure magnesium powders behave reluctant to sintering [5]. That has been overcome when a novel sintering technique employing high purity argon atmosphere with the use of loose magnesium fines as oxygen getter material has been developed [6, 7]. Additionally, the use of calcium is reported to enhance sinter densification through liquid phase formation at sintering temperatures [8, 9]. In fact, PM Mg-Ca specimens produced by conventional press and sinter technique following these recommendations have shown low degradation rates when tested under *in vitro* physiological cell culture conditions with mechanical properties comparable to the as-cast counterparts [10, 11]. However, the discrete effects laid out by PM Mg-Ca material parameters like residual porosity and grain size on the material degradation behavior has not been thoroughly investigated. Realizing these implications is an important task as this decides how robust the degradation property of PM Mg-Ca materials is against the variations in processing conditions. This understanding of material robustness can further help to ascertain material parameter thresholds to ensure a homogeneous and reproducible degradation. This is the main objective of the present thesis where PM Mg-0.6Ca specimens possessing variable porosities and grain structures were immersion degradation tested to find out limitations from the processing perspective to ensure degradation reproducibility.

Conventional press and sinter Mg-Ca materials differ from the common behavior of other sintering systems like titanium in that PM Mg-Ca materials do not exhibit either a significant porosity decrease or grain growth with increasing sintering time [6, 12]. This has to be first addressed to be able to produce specimens required for analysis. Based on the literature guidance, different sintering temperatures were chosen to generate PM Mg-0.6Ca specimens with varying porosities. However, to achieve efficient densification, calcium rich liquid phase shall be made use during sintering and thus the sintering temperatures were chosen in the two phase α -Mg + liquid region of Mg-Ca equilibrium phase diagram [13]. In porous magnesium materials, the characteristics of the pore features are reported to vary with overall porosity [14, 15]. In this regard, an extensive μ CT analysis was carried out for

each specimen porosity level. The obtained data was correlated to the specimen degradation and mechanical property profiles both qualitatively and quantitatively.

Surface alteration of pure magnesium powders seems to be the practical way to introduce grain size variations in the microstructures of PM Mg-0.6Ca specimens. This is due to the possibility of the presence of oxides in both natural and impurity particulate forms on gas atomized powder surfaces [8, 16]. From previous reports, the grain coarsening observed in MIM processed AZ81 material was attributed to the reduced grain boundary pinning effect of the precipitates [1, 7]. However, no such effect has ever been reported for conventional press and sintered Mg-Ca materials. The present work uses physical aberrations created by the mechanical sieving device to alter surface oxide condition of the pure magnesium powder surfaces. The results of such an effect on the microstructure of PM Mg-0.6Ca specimens and therefore on their *in vitro* degradation behavior have been investigated. The specimens used in the present work are also systematically tested for their impurity element concentrations. This gives precedence to the idea of investigating the effects that originate solely either from porosity or grain size variations on PM Mg-0.6Ca specimen degradation. The degradation rates of these specimens are determined via a linear regression fit for the obtained experimental data during *in vitro* immersion degradation test [11]. Simultaneously, tensile tests are performed to investigate its dependence on microstructure. Finally, the link between material parameters like porosity and grain size on the specimen degradation has been understood and clarified with additional processing limitations to be adhered towards achieving a homogeneous and reproducible degradation.

2 State of the art

2.1 Sintering of Mg

Sintering of magnesium powders is greatly inhibited by the formed MgO layer on their surfaces [17, 18]. In air, the thickness of the oxide layer is reported to be 3 - 6 nm when measured on melt spun magnesium ribbons [5]. However, Burke et al. have documented this layer to be nearly 10 - 20 nm thick when measured on pure magnesium powder particles of 1 - 50 μm sizes [18, 19]. This layer prevents inter-diffusivity between the particles during solid state sintering and provides only a point contact between them [17]. This results in poor sinter densities and therefore poor mechanical properties. In order to make the sintering between magnesium particles feasible, the diffusivity between the particles has to be enhanced. Preliminary magnesium sintering studies performed by Wolff et al. and Burke et al. showed alternative ways to circumvent this problem and make sintering of magnesium feasible [20-22]. Wolff et al. initially reported the formation of sintering necks between magnesium powder particles by using oxygen getter material surrounding and protecting the magnesium specimens from oxygen attack during sintering. When such protection does not exist, only point contacts and weak specimen stability were reported [20]. Additionally, reduction of the surface oxide of magnesium powders using alloying additions that are more oxygen affine than magnesium itself have been investigated [21, 23]. Burke et al. investigated the effect of yttrium additions in reducing the surface oxide of magnesium alloy powders. In their testing, they found that yttrium additions in fact reduced the surface oxide enabling sintering. However, they reported swelling of these specimens and a decrease in the final sinter density compared to the green state. Burke et al. attributed this swelling to the abrupt excess of liquid phase created by 2 wt.% yttrium additions in their magnesium alloy powder [24]. Lithium in its hydride and metallic form was investigated by Wolff et al. as a sintering aid for magnesium. They reported positive sintering results with LiH addition resulting in homogeneous microstructure and residual porosity of 13.5% whereas metallic lithium addition resulted in porosities greater than 20% and point contacts between magnesium particles [20].

2.1.1 Calcium as an aid for magnesium sintering

Calcium is considered as a potential alloying element because of its ability to reduce not only the surface oxide but also hydroxides and carbonates at elevated temperatures [8]. CaO has a lower enthalpy of formation (-635 kJ mol^{-1}) compared to MgO (-601 kJ mol^{-1}) [25]. This is presumed to help in minimizing the reactions of magnesium with oxygen during sintering. Additionally, based on the nature of calcium addition and the sintering temperature, transient and persistent liquid phase sintering mechanisms are reported that may help in sinter densification [6]. The idea of sintering of magnesium using calcium as liquid forming additive is similar to the use of magnesium to sinter aluminum which is always considered problematic due to the stable oxide layer on the surfaces of aluminum

powder particles [26]. The advantages of using master alloy route in promoting liquid phases or transient liquid phases have been reported in the literature [27, 28]. The main advantage being the flexibility in tailoring the alloy composition and in achieving homogeneous microstructures in case of base materials that are sensitive to oxygen [16, 29]. Using 1wt.% calcium as an alloying element, Burke et al. reported a density increase and also the possible presence of CaO at the grain boundaries of sintered magnesium specimens indicating the disruption of MgO during sintering under argon [24]. In former works, Wolff et al. also thoroughly investigated the effects of calcium additions to pure magnesium powder sintering in its hydride and master alloy powder forms. They reported positive sintering effects in both cases. However, they recommended calcium additions via master alloy Mg-7Ca to yield beneficial sintering results as the hydride form of calcium caused the formation of large pores nearing 400 μm in size [20]. Later experiments performed using Mg-10Ca master alloy powder also reported good sinter density values for PM Mg-Ca specimens [10, 30]. This was possible also due to the novel labyrinth crucible set up designed for magnesium specimen sintering as shown in Figure 2-1. This setup employs the use of loose and fine magnesium powder as an oxygen getter material surrounding Mg specimens of interest thereby preventing oxygen intake by the specimens during sintering [21]. If specimens are not completely surrounded by oxygen getter material then sintering efficiency decreases (crucible number 2 in Figure 2-1). Experimental investigations on binder development for MIM of magnesium that followed after this development also reported high sintering efficiencies [9, 31].

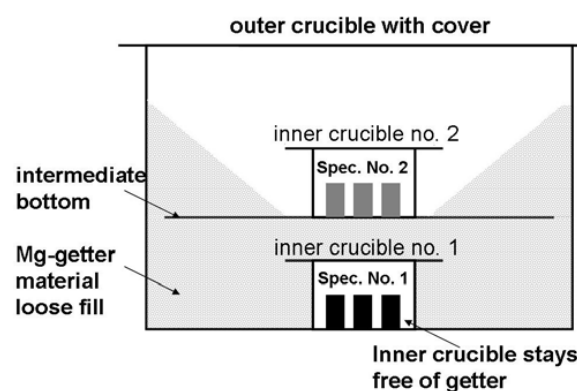


Figure 2-1: Schematic of the crucible setup designed for successful magnesium sintering by Wolff et al. [32]. Specimens in crucible number 1 sinter superior compared to the specimens in crucible number 2. With permissions to reprint from WILEY-VCH Verlag GmbH.

2.1.2 Sintering atmosphere

For oxygen sensitive materials like magnesium, sintering atmosphere has to be regulated to promote optimal sintering conditions. Nitrogen as sintering atmosphere for magnesium sintering has been investigated by Burke et al. In their testing with Mg-Al alloy with 2 wt.% yttrium additions, they reported an increased density under nitrogen sintering atmosphere compared to green state. They theorized that the yttrium nitrides formed due to the nitrogen sintering atmosphere enhanced the wetting characteristics between liquid

phase and magnesium matrix leading to densification [24]. Hydrogen as sintering atmosphere may cause formation of water vapor due to oxygen byproducts during sintering. This can lead to swelling of the components and weaken the mechanical properties of sintered parts [33]. Adapting vacuum or inert gases appears to be a promising alternative to removing moisture hindrance during sintering [34]. However, in case of magnesium sintering, use of vacuum at sintering temperatures may cause loss of magnesium owing to its low vapor pressure at elevated temperatures [35].

Schaper et al. investigated the influence of hydrogen on thermal debinding and sintering of MIM Mg-0.9Ca specimens prepared with polyethylene and polypropylene based binder feedstock systems. They reported an improved longitudinal shrinkage value nearing 12% by the use of hydrogen atmosphere (using polyethylene binder complex) compared to argon atmosphere where the shrinkage values were found to be lower than 2%. They attributed the benefits of hydrogen sintering for MIM Mg-0.9Ca specimens to the removal of carbon byproducts/residuals (from the thermal debinding step) in the form of methane [36]. However, the usage might be limited to the magnesium specimens with alloying additions that do not form hydrides [37]. Typically, Ar + 5% H₂ gas combination is reported to use for MIM processed magnesium specimens during thermal debinding step with alternating pressures between 0 and 800 mbars to reduce reactive monomer residuals [9].



Figure 2-2: (A) Point contact between magnesium particles after sintering that are free from oxygen getter material. (B) Sinter neck formation between magnesium particles when surrounded by oxygen getter material [32]. With permissions to reprint from WILEY-VCH Verlag GmbH.

Argon gas sintering is employed where the formation of hydrides or nitrides due to the alloying additions are to be minimized. Furthermore, preparation of the furnace by leakage checks, cycles of evacuation and flooding with argon gas before the commencing of sintering and utilizing high purity argon during sintering are reported to minimize the oxygen content in the furnace [6]. Wolff et al., utilizing the crucible setup shown in Figure 2-1, illustrated the extreme scenarios of the effect of oxygen by altering the oxygen getter material (loose magnesium powder) around the specimens. The resulting effect is shown in Figure 2-2 A, where only point contacts are visible when specimens are directly exposed to furnace residual oxygen. In contrast, sintering necks are visible when oxygen getter material offers protection, as in Figure 2-2 B. Sintering is sluggish and initial necking takes place around 8 h sintering. At ambient pressures, the sintering is slow as the calcium has to

reduce the oxide and sintering has to forward leading to longer sintering times. Vacuum can be used to speed up the process but attention shall be given to magnesium sublimation at the cold furnace parts [38].

2.2 Liquid phase sintering

Liquid phase sintering involves the coexistence of liquid and particulate solid phases during a particular thermal cycle. Typically, the liquid phase exists throughout the isothermal holding period providing rapid densification and pore closure [39]. One classical example would be the heating of clay bricks, which produces a glassy liquid phase at sintering temperatures. These were known to be produced several centuries ago indicating the early applications of liquid phase sintering. Liquid phase sintering generally involves heating of compacts made of either pre-alloyed powders or a mixture of two constituents (powders of different chemistries or a mix of powder and liquid forming additive), to liquid forming temperatures followed by a certain holding duration. One constituent has a lower melting temperature or helps in the formation of a eutectic phase which generates the necessary liquid phase at sintering temperatures [40]. Depending on the temperature employed and inter-diffusivity of the two components, pore free dense structures in the final material can be obtained [39].

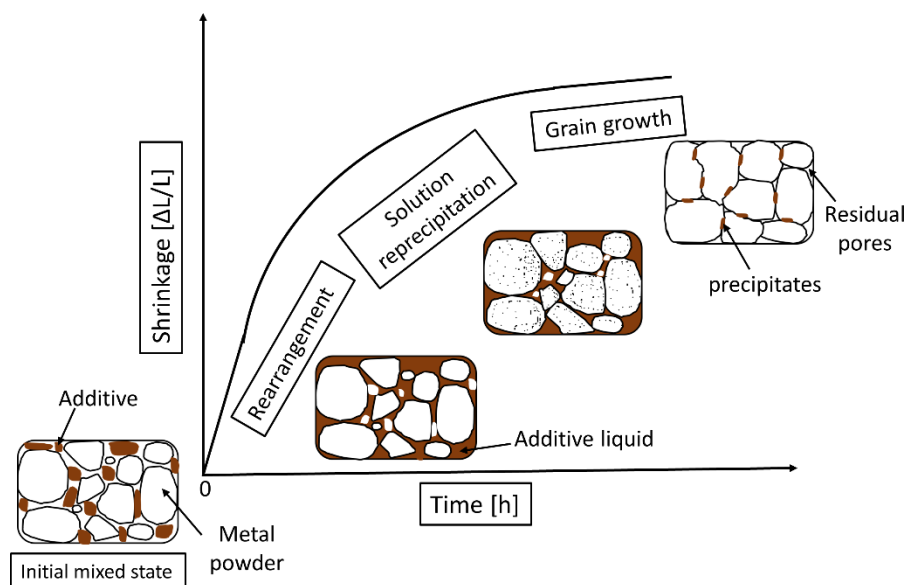


Figure 2-3: Schematic illustration of different stages involved in liquid phase sintering based on [41].

Liquid phase sintering is generally proposed to have four stages. First, the melting of the liquid forming additive and redistribution of the liquid. Second, the solid particle rearrangement by the capillary action of the formed liquid. Third stage is the shape accommodation of the solid phase and therefore densification by solution-precipitation mechanism, where the solid solubility in the adjacent liquid films favors the transport of the solid to the adjacent solid particles. This causes the dissolution of small grains on to the adjacent large particles. Fourth stage is the final densification of the material leaving behind

the residual porosity followed by grain growth [41, 42]. The exact differentiation between these different stages with sintering time is not simple and often they overlap depending on the initial powder particle sizes, sintering temperature, heating rate and liquid phase amount etc. The schematic of typical liquid phase sintering system is shown in Figure 2-3. It is reported that the solid phase should have a high solubility in the formed liquid to promote densification as this enhances solution reprecipitation step in liquid phase sintering systems. At the same time, the amount of liquid phase should not be too high that the solid phase may not maintain the structural stability to the compact during sintering [42, 43].

2.2.1 Mg-Ca phase diagram

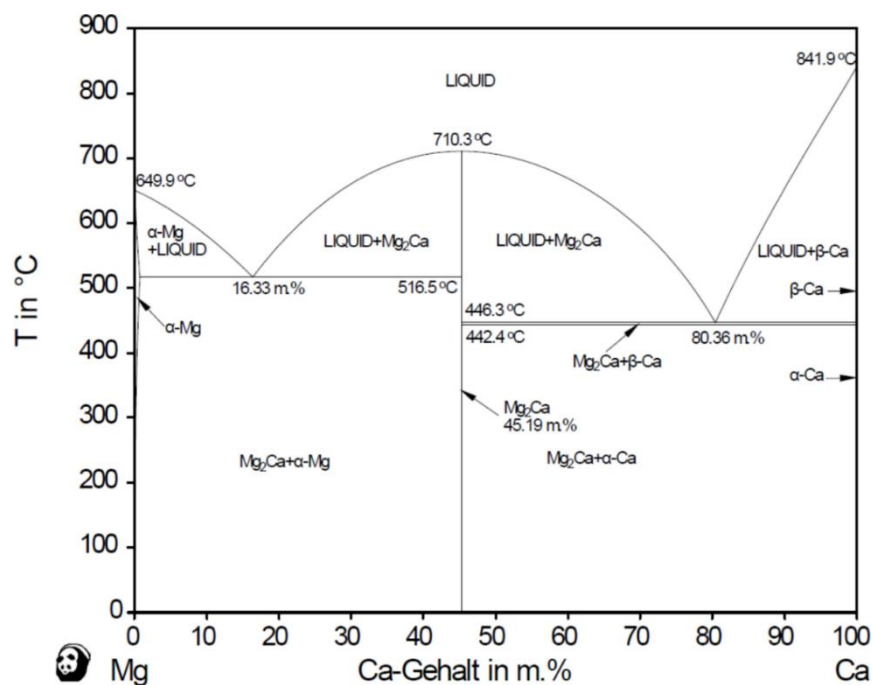


Figure 2-4: Calculated Mg-Ca phase diagram using PanMagnesium 8 database [13].

As indicated in section 2.1.1 and section 2.1.2, calcium promotes magnesium sintering by forming liquid phase at elevated temperatures. This effect can be brought out by blending pure magnesium with calcium rich master alloy powder, like Mg-10Ca, and then choosing the sintering temperatures in the two phase α -Mg + liquid region of the Mg-Ca equilibrium phase diagram (Figure 2-4). The phase diagram on the magnesium rich side indicates a narrow single phase α -Mg solid solution with maximum solubility of 0.74 wt.% calcium at 516 °C. Above and below this temperature, the maximum solid solubility of calcium decreases following the solidus and the solvus lines, respectively. Two invariable eutectic reactions can be seen; one occurring at nearly 16.3 wt.% Ca at 516 °C and the other at 80.3 wt.% Ca at 446 °C. Wolff et al. fabricated Mg-1Ca alloy and Mg-1.4Ca alloy by powder blending pure magnesium and eutectic Ca-18Mg master alloy powder and reported liquid phase formation upon holding at 445°C for a short duration. Positive sintering results are shown in their works at the expense of the formation of brittle Mg₂Ca phases in the

sintered microstructures as dictated by the room temperature phases in Mg-Ca phase diagram [6, 20]. The phase diagram has an intermediate compound Mg_2Ca occurring at nearly 45 wt.% Ca. The magnesium rich side of the phase diagram also indicates that the dominant room temperature phases are $\alpha\text{-Mg} + \text{Mg}_2\text{Ca}$.

2.2.2 Evolution of liquid phase mass fraction with sintering temperature

Lever rule provides an estimation for the mass fraction of the different phases in a binary equilibrium phase diagram for a given composition and temperature. A tie line or an isothermal line is drawn across the length of the phase diagram. A vertical line is then drawn at the desired binary composition on the phase diagram to intersect the tie line. The estimation for the particular phase fraction, for example liquid phase, is then computed by taking the length of the tie line situated away from the desired phase and dividing it with the total length of the tie line along the phase borders. This is illustrated in Figure 2-5, using Mg-10Ca alloy as an example.

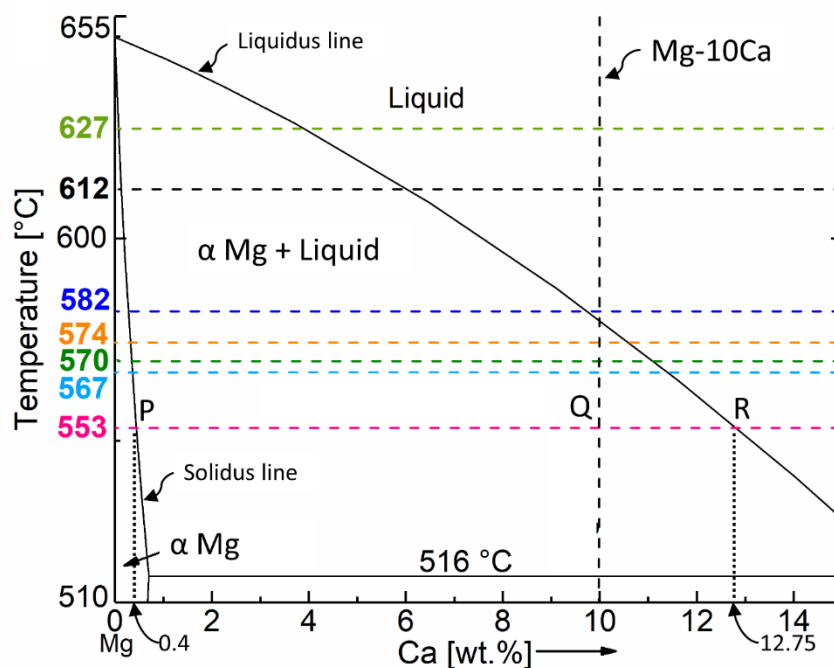


Figure 2-5: Magnesium rich side of Mg-Ca equilibrium phase diagram showing isothermal lines at different sintering temperatures above the eutectic temperature of 516 °C.

At the sintering temperature of 553 °C, the Mg-10Ca binary composition intersects the tie line (shown in pink) at point Q in Figure 2-5. The tie line intersects the solidus and liquidus at the points P and R, respectively. The corresponding compositional values at these intersection points are at 0.4 wt.% Ca and 12.75 wt.% Ca, approximately. This is shown by the dotted vertical lines drawn at points P and R to the x axis. The mass fraction of liquid phase present at this sintering temperature is given by,

$$\% \text{ mass fraction of liquid} = \frac{\text{length of tie line away from liquid phase} * 100}{\text{total length of the tie line}} \quad (1)$$

$$\% \text{ mass fraction of liquid} = \frac{(10 - 0.4) * 100}{12.75 - 0.4}$$

$$\% \text{ mass fraction of liquid} = 77.7 \%$$

The α -Mg phase mass fraction can be then estimated as 22.3%. From Figure 2-5 it can be seen that by heating to just above 516 °C, nearly 50% of Mg-10Ca alloy transforms to liquid and continues to increase thereafter. At sintering temperatures near and above 579 °C, master alloy transforms to complete liquid. At other intermediate sintering temperatures like 567 °C, 570 °C and 574 °C shown in Figure 2-5, the mass fraction of liquid formed is nearly 85%, 90% and 94%, respectively. Lever rule can also be useful in cases where sintering has to be performed for different alloy compositions, however, with constant amount of liquid phase in the chosen alloy compositions. In such cases, using the lever rule would yield different sintering temperatures for these different alloy compositions so that the equal amounts of liquid phase exists during sintering [10].

2.2.3 Variation in density with sintering time and temperature

It is reported in liquid phase sintering systems that, analogous to solid state sintering, either with increasing sintering time and/or temperature, the density of the compact increases. The most effective way to promote sinter densification is to use high sintering temperatures that favor high amounts of liquid phase as illustrated in the previous section. Kwon et al. used alumina-magnesium aluminosilicate glass system to evaluate the kinetics of sintering densification during liquid phase sintering [44]. Their findings revealed that at a liquid phase fraction of 20 vol.% (glass component), the relative sinter density of > 95% was attained for sintering duration < 3 min. On the contrary, nearly 300 min sintering durations are required to reach similar density levels when liquid volume fraction is 3 vol.%. In the same study, they also reported an increase in relative sinter density for short sintering durations when the starting alumina powder size decreased from 5.9 μm to 2.1 μm as shown in Figure 2-6 A. The common observation in the two above mentioned scenarios is the increase of relative sinter density with increasing sintering time. The factors of high liquid phase amount and fine starting powder size shortened the sintering time for full densification. They reported extensive overlapping of particle rearrangement and solution-precipitation densification mechanisms between relative sinter densities of 66% and 96% in this alloy system [44].

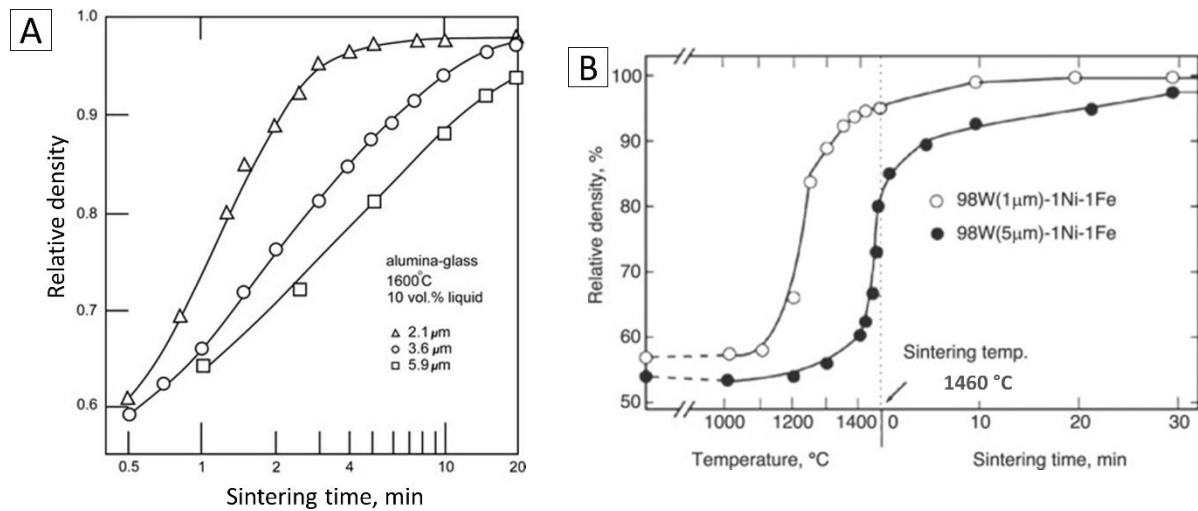


Figure 2-6: (A) Increase in relative sinter density with increasing sintering time in alumina-glass liquid phase sintering with varying initial particle sizes [44]. With permissions to reprint from WILEY-VCH Verlag GmbH. (B) W-Ni-Fe alloy system densification until reaching liquid phase sintering temperature and during isothermal holding period [45]. With permissions to reprint from the Minerals, Metals & Materials Society and ASM International.

Similar observations were made by Dong et al. during air sintering of alumina-10 vol.% glass systems where relative sinter densities increased rapidly from 80% till 95% with 5 min till 1440 min of sintering durations. They reported a slow densification during the intermediate to final stages of sintering owing to the slow rate of pore closure due to the trapped gases inside the closed pores [46]. Also in solid state sintering systems, for example, in mechanically alloyed iron based powders, increasing sintering time from 5 to 30 h at 1150 °C increased the specimen relative sinter density from 79% till 87% [47]. Park et al. reported that majority of densification in 98W(1μm)-1Ni-1Fe alloy was reached during heating stages of liquid phase sintering where relative density increased from green state at 57% till 95% before even formation of liquid phase as shown in Figure 2-6 B. Only a slight increase in sinter density is witnessed during further isothermal holding at liquid phase sintering temperature of 1460 °C. They indicated that the initial state at the onset of liquid phase sintering under normal heating rates can be different to that of a presumed green compact state [45]. The increased density in solid state with increasing sintering temperature, however, can be related to the presence of 1 wt.% Ni which is reported to promote activated sintering in W-Ni systems. The grain boundary diffusivity induced by small additions of nickel (~ 0.4 wt.%) on tungsten grain boundaries is active at sintering temperatures above 1200 °C and is reported to promote densification in these alloys in solid state sintering [48].

In magnesium sintering systems, however, such behavior of rapid increase in relative density with increasing sintering time is reported rarely. Aghion et al. performed sintering of MRI 201S magnesium alloy powder produced after 10 h blade milling of machined chips in temperature ranges of 500 - 640 °C for 3.5 h [49]. Their reported porosity values are 15.2% and 14.6% at 500 °C and 640 °C, respectively, which is only a slight decrease given the vast

temperature difference. They additionally reported the oxide layer thickness to be 20 nm from their XPS depth profiling measurements that might have played a role in hindering densification. Oxide layer presence is evident despite their blade milling of magnesium alloy chips taking place essentially under argon atmosphere [49]. Čapek et al. investigated the effect of sintering time on the densification of porous magnesium at sintering temperature of 550 °C. Their reported porosities ranged from 24 vol.% till 29 vol.% with the sintering time increase from 3 h till 24 h. No reasoning has been given as per the choice of 550 °C as the set sintering temperature in their work [50]. In the former works with master alloy blending route to produce dense PM Mg-0.6Ca and Mg-1Ca alloys, Wolff et al. reported the formation of closed pores at 64 h sintering durations. When sintered for 4 h, they reported the presence of open pore structures [21]. In their follow up work, they observed neck formation in MIM Mg-0.9Ca specimens after 8 h of sintering followed by a sharp decrease in residual porosity from nearly 20% to 15% after 8 h sintering time. The specimen porosity was reported to further reduce to below 5% at extended 64 h sintering duration at 635 °C [38]. They attributed the need for long sintering times to the slow process of destabilizing and reduction of oxide layer by calcium rich liquid phase .

2.2.4 Grain growth

Grain growth is a natural occurrence in sintering where the high temperature thermal energy promoting sinter bonding by atomic motion also promotes atomic transport across the grain boundaries leading to grain growth [51]. Grain growth during sintering can be characterized into normal and abnormal. In the former, the mean grain size increases with sintering time while the average number of grains decreases. The normal grain growth is reported to follow a power law $G^n \propto t$, where G is the grain size at given sintering time t . The exponent n is reported to be 3 indicating grain volume increases linearly with time [52, 53]. In case of abnormal grain growth, only a few grains grow at the expense of others leading to bimodal grain size distributions with sintering time [54, 55]. During liquid phase sintering, early grain growth during initial stages is reported to be slow due to the presence of pores effectively reducing the solid liquid interfacial area. As densification proceeds and pore closure occurs, the reduced pore-drag on the grain boundaries and high diffusion rates of the solid in the liquid at high interface area leads to rapid grain growth at later stages of sintering. This also implies that the densification and grain growth often have overlapping consequences and that grain growth may still occur after reaching the maximum sintering densification [52, 53]. Additionally, when high liquid contents are available during sintering, large grains adjacent to each other are reported to merge due to coalescence process when their grain boundary misorientation angles are less than 10° [56].

Abnormal grain growth is reported in cases where the matrix grain boundaries may be pinned by second phase particles or impurities [57]. This is ironic as these static particles exert a pinning force that is reported to counteract the grain boundary interfacial free energy and therefore should prevent even normal grain growth [58]. As a moving grain boundary encounters with these pinning particles, it dissipates more free energy to

overcome these particles and hence becomes difficult to move. However, due to the thermal fluctuations of grain boundary away from its particles, coarsening or dissolution of the precipitates or the formation of glassy phases at grain boundaries due to impurities, the abnormal grain growth is reported to initiate and progress [55, 58, 59]. Additionally, abnormal grain growth is reported in materials with minority texture, grain boundary diffusivity activations, rough or smooth crystallographic interfaces of the grains in liquid matrix, preexisting grains with size advantage etc. [60, 61]. Subsequently, different mechanisms are proposed that best describe the abnormal grain growth behavior depending on the compositional variations, texture or anisotropy in the microstructure, grain boundary structural transformations due to impurities etc. [62, 63]. It is reported that abnormal grain growth prevents high sinter densities in ceramic materials, for example, alumina due to the entrapment of pores in the large grains that are often too difficult to remove [64, 65].

In alumina sintering systems, the addition of MgO is reported to promote particle pinning effect at the grain boundaries and promote normal grain growth. However, CaO or SiO₂ additions in trace amounts nearing 30 ppm and 300 ppm, respectively, promote abnormal grain growth in alumina. These impurities form glassy phases enough to wet the grain boundaries of alumina, for example, 3 - 5 nm thick for a SiO₂ doping concentration initiating abnormal grain growth in alumina [64]. In Sr-Ba-Nb ceramic oxide systems, the grain boundaries enriched with Nb₂O₅ rich and BaO deficient regions caused low temperature liquid forming zones compared to the sintering temperatures and promoted an abnormal grain growth behavior in these systems [63]. In Fe-20 wt.% Cr alloy system, different concentrations of nitrogen in the melt at 65 ppm, 250 ppm and 490 ppm caused the initiation of abnormal grain growth after the nitride precipitate dissolution at sintering temperatures nearing 1200 °C. Similarly, in MIM nickel base super alloys, the grain size restriction due to mixed refractory metal Ta MC carbides at the grain boundaries of nickel was lost after heat treating above the solidus temperature during super solidus liquid phase sintering [66].

In magnesium liquid phase sintering systems, the oxide particle pinning effect as the reason for restricted grain growth behavior was anticipated since the preliminary successful magnesium sintering results [21]. Providing long sintering durations nearing 64 h under argon atmospheres, nearly homogeneous microstructures were reported with no apparent grain growth, irrespective to conventional press and sinter or MIM techniques [30, 38]. Certain grains, insignificant in number, possessing grain sizes nearing 100 µm were observed in Mg-1Ca alloy system produced by powder blending pure magnesium and Mg-7Ca with powder sizes less than 45 µm and 75 µm, respectively [6]. However, such grain growth observations were not reported in their later works, presumably due to the randomness/inconsistency in their occurrence. In a recent work by Schaper et al., grain growth in MIM AZ81 specimens was reported following a heat treatment at 420 °C for 10 h and was attributed to the reduced oxide pinning effect during the heat treatment [7].

2.3 Mg in biomedical implant framework

Magnesium and its alloys are candidate materials for degradable implant applications where they stay in human body temporarily for bone healing purposes while providing sufficient mechanical strength during healing. With bulk densities ranging between 1.74 - 1.8 g/cm³, they are the closest to that of natural bone at 1.8 - 2 g/cm³. Additionally, magnesium alloys have the potential to reduce the mismatch in mechanical properties between the bone and magnesium implant making them a better choice over stainless steel or titanium for temporary implant applications. It is reported that this reduced strength mismatch between the input implant and the targeted bone may reduce the stress shielding effect, a non-desirable phenomenon that is otherwise seen in bone implants with high strength profiles, leading to bone refracture at the implantation site [67]. Magnesium finds its use in over 300 enzymatic reactions in the human body especially in host tissue interactions. It is also an important co-factor for DNA and RNA synthesis. It promotes the supply of purine and pyrimidine nucleotides during cell proliferation for synthesis of DNA and RNA [68]. The reported total body magnesium content is 25 g, 67% of which is stored in bone. One third of this is exchangeable and is present on the skeletal bone surface making a reservoir to maintaining extracellular magnesium concentrations [69]. Magnesium is released in conjunction with other elements like calcium, sodium and phosphorous during bone growth and healing stages. This makes magnesium an important constituent in every day diet (300 - 400 mg/day) along with the intake of other nutrients [70].

2.3.1 Mg-Ca alloys

Calcium alloying addition was intentionally developed in the view that it is a major component of human bone in the form of bone mineral hydroxyapatite. Bone mineral constitutes to 40% of bone weight indicating that it is an important reservoir of calcium [71]. Calcium alloying is reported to improve the mechanical properties and degradation resistance of pure magnesium [72-75]. The density of calcium is 1.54 g/cm³ which endue Mg-Ca system with a density similar to bone. Also, the release of magnesium and calcium ions during bone healing process is proven non-detrimental to the physiology of the body [76]. Keeping these aspects in view, several investigations were made to evaluate the structure property relations in this alloy system. Particularly interesting is the *in vitro* and *in vivo* degradation behavior of Mg-Ca alloys [74, 77, 78].

Rad et al. investigated the microstructure of Mg-xCa (x = 0.5, 1.25, 2.5, 5.0 and 10 wt.%) alloys in their cast conditions and indicated that an increase in calcium concentration led to a decrease in the grain size of the alloy. This microstructure also composed of huge volume fraction of Mg₂Ca phase leading to improved strength profiles via solid solution and precipitation strengthening, however, at the cost of ductility with increasing calcium in the alloy [75]. Similarly, Li et al. reported in Mg-xCa (x = 1 - 20 wt.%) alloys that the formation of brittle Mg₂Ca phase serves as a source for cracking and therefore negatively impacts material ductility. They reported 1 wt.% Ca as the optimal concentration to maintaining both mechanical and degradation properties [77]. Mohamed et al. reported excellent

biocompatibility for Mg-0.8Ca alloy in HBSS cell culture media due to the formation of hydroxyapatite type structure on the degrading Mg-Ca surfaces. They reported Mg-0.8Ca degradation rate nearing 1 mm/year and attributed the degradation to the anodic dissolution of the formed Mg_2Ca phase, leaving the matrix grains unsupported until they detach with progressive degradation [79]. Similar anodic dissolution effect of Mg_2Ca phase was reported by Liu et al. in their specially designed Mg_2Ca/Mg galvanic couple where high anodic current density, elevated Mg^{+2} and high pH values were found [80]. This is an opposite behavior with respect to the secondary phases in other magnesium alloy systems where the secondary phases act as cathodic sites initiating magnesium degradation in the vicinity of these phases [81].

MgF_2 coated Mg-xCa (0.4 - 2 wt.%) alloys are reported to provide optimized degradation and biocompatibility with human smooth cells and endothelial cells [82]. Wan et al. postulated 0.6 wt.% Ca as an optimal composition for compression strength and degradation resistance from their investigated Mg-xCa (x= 0.6 - 2.0 wt.%) alloys [83]. Microalloying of calcium is also reported to induce impurity stabilization promoting microstructural homogeneity. Deng et al. fabricated cast lean Mg-xCa (x= 0.05 - 0.15 wt.%) alloys with impurities iron and silica contents at 14 - 16 ppm and 34 - 97 ppm, respectively. However, they reported no detrimental effect arising due to the possible formation of Fe-Si phase in all their investigated alloys. They postulated that calcium hinders the formation of iron containing particles prompted by silicon presence by forming CaMgSi phase [84]. These reports show promising *in vitro* degradation results in magnesium alloys with potentially < 1 wt.% calcium concentrations.

2.3.2 Magnesium degradation

The degradation mechanism in magnesium alloys involves the presence of the formed secondary phases and/or impurity elements with the magnesium matrix. Although these phases are the prime reason for improvement of mechanical properties, they are also the reason for the retarding degradation resistance in magnesium alloys. In most cases, a galvanic circuit is formed between the magnesium matrix and the secondary phase in the presence of a cell culture medium acting as an electrolyte. Such a circuit would preferentially protect one species of the electrodes resulting in dissolution or degradation of the other; in this case the magnesium matrix [85]. Magnesium possesses the lowest electrochemical corrosion potential value of -1.65 V. Pertaining to electro motive force (emf) series, magnesium is regarded to be an active metal (-2.37 V_{nhe}). The formation of MgO or $Mg(OH)_2$ layer on the surface of magnesium causes the difference in its emf and actual corrosion potential values [86, 87]. In either case, magnesium is an active metal that preferentially dissolves in electrolytic type media making it anodic to almost any metal that comes in contact with. This can be seen as macro galvanic corrosion between magnesium and other engineering metal in Figure 2-7 A. The rate depends on the difference of electrode potential values between the adjoining phase and magnesium matrix. The equilibrium potential values of some commercial metals are shown in Table 1.

Table 1: Typical equilibrium potential values of common engineering metals in aqueous solutions [88].

Element	Potential value (V)
$\text{Mg}^{+2} + 2\text{e} = \text{Mg}$	- 2.4
$\text{Zn}^{+2} + 2\text{e} = \text{Zn}$	- 0.76
$\text{Al}^{+3} + 3\text{e} = \text{Al}$ (0.1 M NaOH)	- 1.71
$\text{Fe}^{+2} + 2\text{e} = \text{Fe}$	- 0.41
$\text{Cu}^{+2} + 2\text{e} = \text{Cu}$	+ 0.34
$\text{Ni}^{+2} + 2\text{e} = \text{Ni}$	- 0.23

In case of micro galvanic corrosion, the adjacent β -phase or impurity phases form localized corrosion cells leading to pitting type of corrosion in magnesium alloys. There is evolution of hydrogen commonly involved in magnesium degradation process. Impurity elements even in trace quantities are reported deleterious for magnesium degradation resistance as shown for iron, copper and nickel compared to calcium, zinc, silver in magnesium in Figure 2-7B.

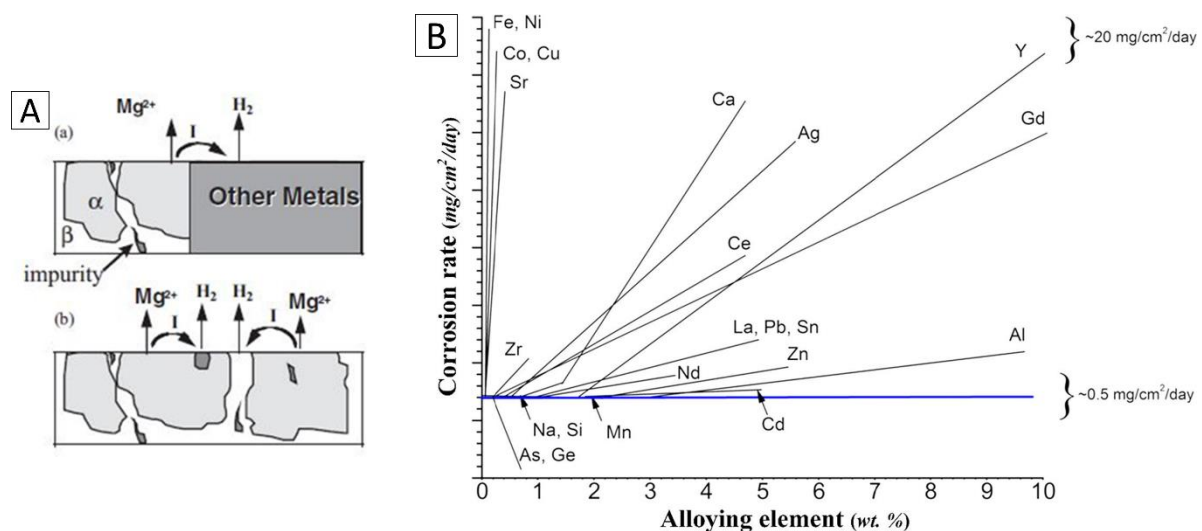
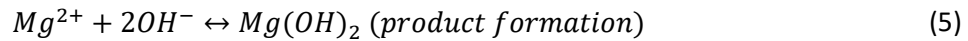
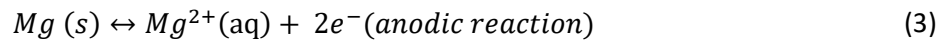
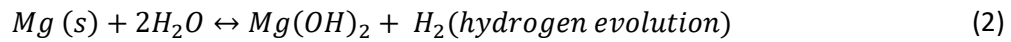


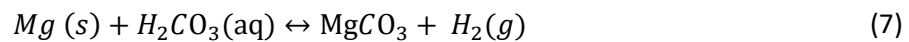
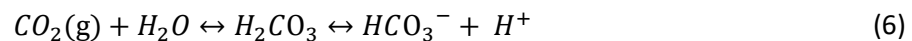
Figure 2-7: (A) Schematics of macro and micro galvanic corrosion in magnesium alloys in presence of other metals and secondary phases within the magnesium matrix [86]. With permissions to reprint from WILEY-VCH Verlag GmbH. (B) Influence of different commercial elements on degradation rate of magnesium alloys [89, 90]. With permissions from Elsevier.

Magnesium degradation mechanism *in vitro*

The degradation of magnesium alloys when exposed to cell culture medium *in vitro* shows a series of chemical reactions which occur at different stages of exposures [77, 78, 91]. The following reactions encompass magnesium degradation mechanism when exposed to aqueous environments:



It can be seen that magnesium degradation produces H_2 gas and $Mg(OH)_2$ as the main degradation product. However, it is also reported that a bilayer composing of thick MgO and porous $Mg(OH)_2$ forms that has a semi protective behavior depending on the surrounding media that the magnesium alloy is immersed in. Presence of chlorine in the physiological media is reported to form $MgCl_2$ upon reaction with $Mg(OH)_2$. $MgCl_2$ is highly soluble in aqueous environments that promotes rapid dissolution of Mg and a simultaneous H_2 evolution. The presence of carbon during in incubation stages of *in vitro* degradation testing combined with the choice of buffering cell culture media like DMEM or HBSS facilitates the following reactions [92]. In ambient air, these reactions would not occur.



The formed products are $Mg(OH)_2$ and $MgCO_3$ in the form of layer during initial exposures to cell culture medium. $MgCO_3$ has a high solubility of 220 mg/L and is reported to precipitate in the degradation layer only when the surrounding aqueous solution is saturated. However, due to the continuous supply of CO_2 by buffering cell culture media in semi static test conditions and in the testing incubator environments, the deposition of $MgCO_3$ is observed as the main degradation product [93, 94]. Additionally, the presence of phosphate and calcium in the physiological fluid and protein complex through FBS is also reported to cause the formation of amorphous calcium/magnesium carbonate and phosphate related degradation products [95].

2.3.3 Determination of mean degradation rate in Mg alloys

Standard immersion tests involve the magnesium material exposure to the cell culture medium for a particular duration (ex. 3 days) and the degradation rate is estimated using the equation proposed in the ASTM NACE/ASTM G31-12a standard [96]. This equation conveniently transcribes this single time point measurement to the order of a year as shown below.

$$\text{Degradation rate, } DR = \frac{\Delta m \cdot k}{A \cdot t \cdot \rho} \quad (8)$$

Where, A is the surface area (cm²), ρ is the specimen density (g/cm³), t is the immersion time (h) and k is the constant 8.79 x 10⁴ that expresses the rate value in mm/year. However, this approach is flawed as magnesium degradation behavior over the testing duration can potentially change. This indicates that a certain magnesium alloy may behave better, equal or worse in terms of its time dependent degradation when compared to another magnesium alloy. This is shown in Figure 2-8 A where different lines represent different degradation behaviors as follows (1) linear degradation (2) low degradation rate at the beginning, increasing at the end (3) initial linear degradation, increasing degradation at the end (4) initial high degradation, linear at the end (5) initial high degradation, zero degradation at the end [11]. This is a crucial step in new magnesium alloy development where various magnesium alloys are primarily categorized for their suitability as implant materials based on their *in vitro* degradation rate values.

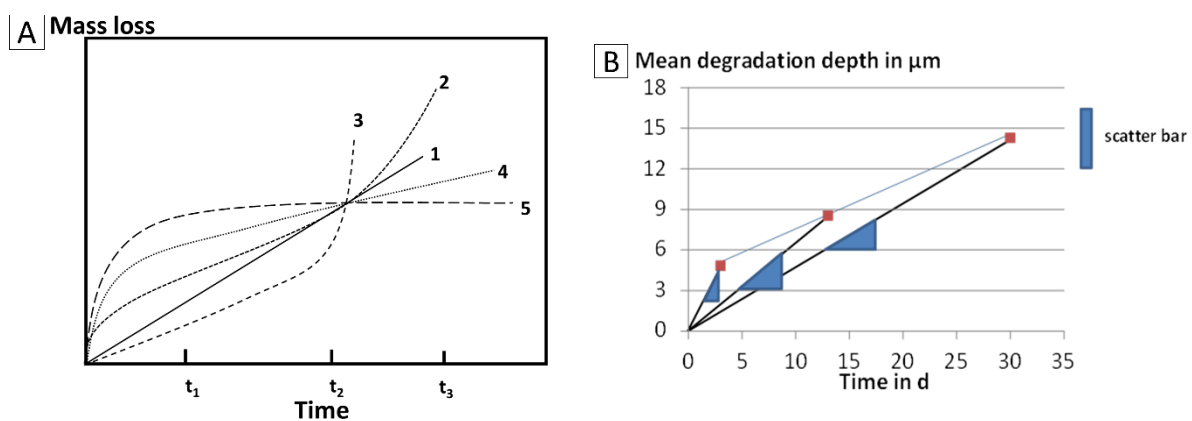


Figure 2-8: (A) Schematic of possible degrading scenarios shown via mass loss vs time curves for a degrading magnesium alloy and (B) Degradation profile for Mg-2Ag immersed in DMEM + 10% FBS cell culture medium where blue triangles represent degradation rates measured according to ASTM equation and blue line is the regression fit for the experimental red points [11].

Additionally, the degradation rates measured using above equation at different incremental immersion time points (ex. seventh day) represent the degradation happening from initial immersion (near zero time point) to that particular time point of interest (seventh day). This excludes the information on the perennial degradation behavior with respect to the previous measured time points (ex. third day through seventh day). This is shown in Figure 2-8 B for Mg-2Ag alloy where a decrease in the slope value of the degradation rate is observed with increasing immersion time as indicated by the ASTM standard. However, the linear fit for the experimental mass loss data shows a unique slope value which takes into account the average degradation occurring at all the measured former time points. The decrease in degradation rate with immersion duration is a reported consequence in magnesium degradation studies [97, 98].

Based on the literature observations on magnesium degradation, Dahms et al. proposed an analytical equation that can describe magnesium degradation behavior from the initial point of immersion till long immersion durations in weeks. They introduced mean degradation depth (μm) which is a purely material parameter and their model included an analytical equation that represents exponentially high degradation upon initial immersion followed by a steady state degradation during later stages of immersion as dictated by the equation given below [99]:

$$h = h_0 \cdot \left(1 - e^{-\frac{h}{h_0}}\right) + \dot{h}_\infty \cdot t \quad (9)$$

The parameter h_0 represents the degradation depth attributing to initial reactions (μm), \dot{h}_∞ represents the magnesium alloy degradation rate at higher immersion times ($\mu\text{m}/\text{day}$), h is the mean degradation depth obtained from mass loss experiments (μm) and t is immersion time (days). In practical relevance, the degradation rate is obtained by the slope value of the linear regression fit for the experimental mean degradation depth vs time plot as shown in Figure 2-8B. Due to the complex nature of reactions occurring at the magnesium and fluid interface during immersion, this mathematical description of magnesium degradation has limitations in that these electrochemical processes are described by a single parameter effective layer thickness. This over simplification may not contribute towards quantifying single effects happening at the interface. However, the authors proposed that this model enables fast screening of magnesium materials with reliable degradation test results under defined test conditions [99].

2.4 Critical factors affecting Mg degradation

2.4.1 Impurity concentrations

It is well understood from several studies on magnesium degradation that the impurity concentrations of iron, copper and nickel should be kept as low as possible to prevent localized galvanic corrosion in magnesium specimens. Being present in trace amounts, the lowered degradation resistance has been attributed to severe pitting and surface erosion occurring due to impurity particles [100-103]. Though a surface protective $\text{Mg}(\text{OH})_2$ layer forms during progressive degradation under aqueous environments, the impurities present in the material bulk still pose a threat because of the electrochemically driven degradation nature of magnesium alloys. Hence, new alloy designs have been developed by microstructural modifications to improve the impurity tolerances in magnesium [104, 105]. These include slower solidification rates during casting to prevent impurity segregations, addition of suitable alloying elements which may form compounds that reduce the negative impact of impurities. For example, zinc is expected to increase the tolerance of copper levels in magnesium [106], so as manganese, aluminum and yttrium to improve iron tolerance in magnesium [107-109].

Depending on the alloy type and processing conditions, the tolerance values for impurities in magnesium materials are reported to change. The tolerance values for iron, nickel and copper in cast pure magnesium listed in the literature are 170 - 180 ppm, 20 - 50 ppm and 300 ppm, respectively [91, 105, 110]. However, more acceptable values for iron and nickel are reported to be 50 ppm and 10 ppm, respectively by Marco et al. by their *in vitro* degradation testing of Mg-Ag and Mg-Gd alloys [111]. Decrease in impurity content is in general reported to improve degradation resistance in magnesium alloys. For example, Dai et al. reported that with a decrease in iron content from 150 ppm to 10 ppm in solution treated AZ61 alloys, the degradation rates decreased from nearly 8.6 mm/year to 0.2 mm/year. Furthermore, this improved degradation rate with reduced iron content is observed to be superior to that witnessed in their as cast counterparts [112]. Matsubara et al. reported that degradation accelerated in the microscopic vicinity of iron rich particles in magnesium matrix, which further enhanced with increased inclusions containing high iron contents [113]. However, sometimes the impurity concentrations obtained via chemical analysis (ppm) may not directly suggest the rejection of the investigated material prior to degradation studies. It is reported that iron in form of compounds can be less detrimental to magnesium degradation compared to free standing iron in the magnesium matrix [111, 114, 115]. Harmuth et al. observed that the degradation rate in extruded Mg-10Gd alloy was not affected by nearly 120 ppm iron content. Irrespective to iron concentration, all their Mg-xGd alloys (x = 2, 5, 10 wt.%) showed degradation rates lower than 0.3 mm/year in their study [114]. Thermodynamic phase calculations revealed that alloying additions like manganese in magnesium can improve the degradation resistance despite iron presence by reducing the precipitation of iron rich phases respective to casting temperature [105]. In other works, Ca/Si rich phases observed in the microstructures of Mg and Mg-Zn alloys are reported to have negative effects on degradation [116-118]. A contamination of Mg-Ca-Zn alloy with nearly 150 ppm silicon resulted in Mg/Ca/Si phase and is reported to be cathodic in nature within the first 24 hour immersion in NaCl solution [117]. Na et al. reported that silicon contamination as high as 5 wt.% to have only limited deleterious effect on magnesium degradation due to the low difference in volta potential values of Mg₂Si and magnesium matrix [119, 120]. However, in presence of calcium, the formation of Ca/Si/Mg phases are again cathodic and accelerated magnesium corrosion [116]. Some studies indicated that the critical factor for magnesium degradation may not directly be the impurity quantity itself but the reaching of breakdown potential of the surface film created by impurities with degradation progress [121]. Therefore, the necessity of documenting the precise chemical composition and technique employed for the magnesium alloys under investigation has hence been suggested [85].

With respect to magnesium powders, the nature and/or the content of impurities in the produced powders may vary from their initial cast material state as the impurity particles may act as favorable sites for compound formation during high degree of undercooling involved in gas atomization processes [122, 123]. Additionally, post processing treatments like analytical sieving treatment of gas atomized powders may add impurities

from the contact materials [124]. This would mean that the specimens produced from these magnesium powders may constitute to a different degradation compared to their bulk forms and therefore chemical analysis investigation of the starting powders becomes necessary when producing magnesium alloys using PM techniques.

Most reported works on PM of Mg focused on sinterability of magnesium and/or the suitability of produced porous magnesium parts as scaffold materials from a mechanical property standpoint. Therefore, these works made use of starting pure magnesium powders with technical grade purities $\geq 99.5\%$ [6, 50, 125-128]. In one work by Wolff et al. spark emission spectroscopy results reported for iron, copper and nickel were 11, 37 and 26 ppm for EZK400 alloy produced by PM press and sinter technique [129]. Majority of the literature on porous magnesium materials designed for degradation testing did not report on the detailed impurity analysis of the tested specimens under investigation [14, 97, 130, 131]. This leads back to the condition that no stringent tolerance limits for impurities may yet exist for porous magnesium materials arising the question of robustness in the processing and final material degradation properties. However, the general criterion that the impurity concentrations in magnesium alloys should be low is still valid and has to be abided, irrespective to the processing condition when aiming for biomedical related applications.

2.4.2 Porosity and pore features

Porous magnesium materials reported in the literature possess majorly open pore structures and were evaluated for their degradation and mechanical properties [97, 126, 132, 133]. A brief overview of the developed porous magnesium materials can be found in Table 2. Only a handful of research exists on PM magnesium materials produced with high sinter densities [9, 127, 134].

Table 2: Brief overview of the development of porous magnesium materials using various production techniques.

Material	Production type	Pore sizes generated	Reported porosity [%]	Reference
Pure magnesium	Carbamide space holder	70 - 400 μm	35 - 55	[126]
AZ91D	Negative salt pattern molding	-	72 - 76	[132]
Mg and Mg-Ca	Powder press and sinter technique	-	< 10	[6]
Pure magnesium and Mg-Al (Al < 17 wt.%) foams	Normal and pressure induced foaming	mm sized pores	60 - 70	[135]
Mg-4Y	Melt extracted short fibers	-	58 - 63	[136]
Pure magnesium	Ammonium bicarbonate space holder	-	12 - 38	[125]

Pure magnesium with Hydroxyapatite coating	NaCl space holder	~ 240 μm	50 - 70	[137]
MRI 201S magnesium alloy	Ammonium bicarbonate space holder	-	14 - 19	[49]
Pure magnesium	Ammonium bicarbonate space holder	-	29 - 31	[50]
Pure magnesium	PMMA space holder	-	1 - 40	[127]
MgP ceramic scaffolds	NaCl template	0 μm , < 25 μm , 25 - 53 μm	-	[15]
Pure magnesium	Naphthalene space holder	~ 60 μm	20 - 40	[14]
Pure magnesium	NaCl space holder	-	14 - 29	[138]
Pure magnesium with β -Tricalcium phosphate coating	Laser perforation technique	-	42 - 51	[139]
Pure magnesium	GASAR	170 μm	28	[140]
Pure magnesium	Multi - step infiltration casting	0.8 - 1.4 mm	35 - 80	[141]
Pure magnesium	Fiber deposition hot pressing	110 - 300 μm	33 - 54	[131]
Pure magnesium	Carbamide space holder	200 - 400 μm	7 - 55	[142]
Pure magnesium	Camphene space holder	5 - 15 μm	28 - 62	[143]
Pure magnesium	NaCl template replication technique	750 μm	68 - 76	[97]

GASAR: metal/gas eutectic unidirectional solidification process.

PMMA: Polymethyl methacrylate material

The use of space holder particles is considered as a fast and efficient way to generate open porous magnesium structures [50]. In the analysis of Dutta et al., the use of 30 vol.% naphthalene resulted in 40 vol.% bulk magnesium porosity with a huge pore connectivity and open pore structure. The connected porosity was visually presented in their work with no quantification [14]. Majority of pores were reported to be connected in Mg-Zn alloy prepared by powder metallurgy with 30% bulk porosity [144]. In another study by Čapek et al., in pure magnesium with 38 vol.% porosity, high pore connectivity was confirmed via cross sectional electron microscopy images of the produced specimens. However, the closed and open pore nature of porosity was not detailed in their work [125]. Due to the use of space holder materials, generally two types of pore structures were reported in porous magnesium materials [14, 97, 126, 127]. Smaller isolated pores that form due to inherent nature of pure magnesium powder sizes after sintering and large sized pores formed due to

evaporation of space holder particles from the green compact after sintering. In fact, the published literature on porous magnesium materials majorly reported on the pore sizes and volume fraction of the pores formed with only qualitative description of either pore connectivity or the open/closed nature of pores.

The *in vitro* degradation behavior of porous magnesium materials was reported to depend on the porosity, pore morphology, coatings, media compositions etc. [15, 97, 137, 145]. In open porous pure magnesium scaffolds, Jia et al. have observed that the degradation rates between the tested scaffolds with spherical and irregular pore shapes varied by 1.3 mm/year and 0.5 mm/year, respectively. They attributed this change to the faster thinning of the pore struts in spherical pore shaped scaffolds compared to the irregular pore shaped scaffolds during degradation in DMEM cell culture medium [97]. Kang et al. have reported that hydroxyapatite coating of porous magnesium materials improved the degradation resistance when immersed in SBF media. They characterized the degradation resistance by evaluating the pH difference between the hydroxyapatite coated and uncoated porous magnesium materials, which were nearly 8.25 and 10, respectively [137]. Similarly, a combination of polycaprolactone and bioactive glass coating on porous magnesium scaffolds has shown a mass loss of 12% after 144 h immersion while the uncoated porous magnesium degraded completely after 96 h immersion in SBF cell culture medium [145]. Bobe et.al have reported a difference in the *in vivo* and *in vitro* degradation rates of porous Mg alloy W4 produced by melt spun fiber technique. Their reported degradation rate *in vivo* was 0.16 mm/year which was significantly lower to that of the degradation rate measured by hydrogen evolution technique *in vitro*, which was greater than 3.9 mm/year. They attributed this change in degradation rates mainly to the variations in test conditions and environments [136]. Such disparity between the *in vivo* and *in vitro* degradation results have indeed been reported for magnesium alloys, irrespective to the porous or bulk nature of the specimens [111, 146]. In general, though various production routes for porous magnesium materials and subsequent degradation analysis has come forward, the thorough investigation of their degradation rates in relation to the combined effect from the pore features is still reported to be at its beginning stages [147].

2.4.3 Effects of grain size

In magnesium alloys, process conditions and the chosen alloying elements are known to alter the grain sizes [148, 149]. A wide amount of literature exists on how grain size variations may affect magnesium degradation with very different results indicating from none to significant effects. In AZ61 magnesium alloy, the ultra-fine grain sizes of 1 - 1.5 μm has improved degradation resistance due to the enhancement in passive film formation in NaCl solution. The low micro galvanic corrosion activity associated with grain refinement in this study was attributed to the refinement of $\beta\text{-Mg}_{17}\text{Al}_{12}$ phases at the grain boundaries [150]. In Mg-Y-RE magnesium alloy with varying grain sizes of 70 - 0.7 μm , a decrease in degradation rate was reported between coarse and fine grain structures when immersion tested in 3.5 wt.% NaCl solution. An improved positive pitting potential was observed for

fine grain structures indicating high resistance to pitting compared to coarse grain structure in this alloy [148]. Grain refinement achieved either by rapid solidification techniques during casting or surface alteration by selective laser melting were also reported to improve corrosion resistance in magnesium alloys [151, 152].

Marco et al. observed that grain sizes of nearly 43 μm deteriorated degradation performance in extruded Mg-2Ag alloy in all HBSS, DMEM and PBS cell culture media. In the same work, extruded pure magnesium and Mg-10Gd specimens with grain sizes less than 22 μm also showed enhanced degradation resistance for the same testing media. This enhanced degradation was, however, related to the higher concentration of manganese detected in Mg-10Gd and pure magnesium specimens counteracting the iron presence rather than to the smaller grain sizes [111]. Minárik et al. reported that after eight passes of ECAP, ultra-fine grains of same sizes were achieved in both their AE21 and AE42 magnesium alloys. In AE42 alloy, the degradation resistance was reported to improve due to the ultra-fine grains. However, in AE21 alloy the degradation resistance decreased. The improved degradation resistance in AE42 alloy, despite its higher alloying contents, was attributed to the better dispersion of secondary aluminum particles [153].

Harmuth et al. reported that the grain size variations of 2 - 27 μm in Mg-xGd alloys (x= 2, 5, 10 wt.%) brought out by the variations in extrusion parameters has no significant effect on specimen degradation in DMEM cell culture media after 7 days immersion [114]. Wang et al. reported that the grain size of AZ31 alloy decreased from 450 μm to 15 μm in its cast and hot rolled condition, respectively. They reported minimized pitting corrosion with grain refinement when immersion tested in Hank's solution. The mass loss during initial immersion days was reported high for cast AZ31 specimens compared to hot rolled AZ31 specimens though both conditions exhibited comparable degradation rates nearing 0.74 - 0.87 $\mu\text{m}/\text{day}$ after 20 days immersion [154].

On the other hand, Li et al. reported that grain refinement did not improve the degradation resistance through their heat treatment experiments on Mg-Ca-Zn alloys [155]. Bimodal grain size distribution obtained via friction stir processing in AZ31 alloy showed weak degradation resistance (0.445 mm/year) that had finer grain structure. In the non-processed AZ31, the degradation rate was found to be 0.134 mm/year [156]. Song et al. have also reported for pure magnesium grain refined by ECAP process that the strain energy induced at the grain and subgrain boundaries due to ECAP deteriorated degradation resistance in their NaCl immersion testing. Their as cast pure magnesium had 800 - 1500 μm grain size and was reduced to 50 - 100 μm after six passes of ECAP [157].

As indicated in section 2.4.2, PM techniques for producing magnesium materials was aimed at generating dominant porous structures suitable for scaffold related investigations and therefore grain size measurements were of less significance in these works. Limited literature exists in relevance to grain size effect of PM magnesium materials on their degradation performance. For example, in PM Mg-xCa (x= 0.3, 0.6, 0.9 wt.%) specimens with relative sinter densities greater than 95%, the grain sizes reported were 18 - 22 μm , irrespective to calcium concentrations and sintering time. The observed increase in the mass

loss values after three days of immersion in DMEM cell culture media was attributed to the increasing calcium concentration and the effect of grain size was not discernable in the study [10]. Other works related to PM magnesium materials with high sinter densities reported mostly homogeneous microstructures with no significant grain growth [38]. Therefore, the knowledge on the effect of grain size on degradation in PM magnesium materials is still at its infancy. However, the literature evidence suggests that the grain size variations may be associated with the changes in microstructural phases which, in combination, may either show no or significant effect on the final magnesium material degradation [149].

3 Aims of the experiments

Calcium aided liquid phase sintering of PM Mg-Ca materials has been proven beneficial for developing high density sintered parts. However, the actual effect of liquid phase on the relative sinter density of PM Mg-0.6Ca materials due to the variations in sintering parameters has not been thoroughly investigated. Therefore, in the present work, different sintering temperatures within the two phase α -Mg + liquid region of the Mg-Ca equilibrium phase diagram are chosen to elucidate the effects of mass fraction of calcium rich liquid on the relative sinter densities. The aim is to identifying the threshold sintering temperature for enhanced sinter densification when prepared via powder blending route.

Furthermore, the present work aims at resolving the nature of porosity i.e., the fraction of closed and open pore nature formed in PM Mg-0.6Ca specimens at different sintering temperatures. Based on the current results and literature reports, the possible mechanisms for the pore closure owing to the effective liquid phase mass fraction at the chosen sintering temperatures are qualitatively discerned.

Porosity in magnesium materials is considered disadvantageous as it can negatively impact specimen degradation compared to their dense counterparts. However, the detailed analysis on the critical pore features that affect magnesium degradation and the porosity threshold that may still permit the use of magnesium in degradable implant applications is not reported. In this regard, porous PM Mg-0.6Ca specimens of seven different porosities are immersion degradation tested under physiological cell culture conditions to understand and clarify the role of porosity in affecting the *in vitro* degradation profiles of these specimens.

To determine the discrete effects of morphological pore features on PM Mg-0.6Ca specimen degradation, an ex-situ μ CT analysis has been carried out. The results aimed at revealing the key pore features that affect degradation homogeneity and reproducibility in these specimens.

PM Mg-0.6Ca specimens possessing both homogeneous and heterogeneous grain structures are immersion degradation tested to reveal a mechanistic understanding of the differences in grain sizes and subsequent phase change effects induced by grain growth, if any, on the specimen *in vitro* degradation behavior. Additionally, efforts are made through electron microscopy investigations and literature evidence, to detect the possible mechanism favoring grain growth in liquid phase sintered PM Mg-0.6Ca specimens and in relation to the powder surface oxide content of pure magnesium powders.

Impurity particles like iron, copper and nickel in magnesium-based materials are detrimental to magnesium degradation resistance and their tolerable levels (ppm) reported in the literature are prone to vary depending on the base magnesium alloy composition and process conditions. Therefore, the present work constantly aimed at monitoring the impurity uptake, if any, from raw powders (pure magnesium and Mg-10Ca master alloy

powders) till the sintered Mg-0.6Ca specimen production and their degradation tests. This also mitigates the detrimental effects arising from the impurities thereby making it feasible to relate the observed degradation to either porosity or grain structures of PM Mg-0.6Ca specimens.

For biomedical implant applications, mechanical properties often play a crucial role for providing structural strength during implantation and patient healing. Therefore, tensile strength and elongation tests for PM Mg-0.6Ca specimens with varying porosities and grain structures are performed to assess their basic suitability as bone implant materials in combination with their degradation profiles.

Despite the reports of successful sintering results with improved mechanical properties, the question still remains whether PM is a suitable technique for fabricating magnesium alloys for biomedical implant applications. As the present work employs a master alloy blending route for PM Mg-0.6Ca fabrication without additional effects of binder materials, efforts are made to answer this question with necessary process limitations.

4 Experimental

4.1 Powder metallurgy

4.1.1 Raw materials

Powders produced by gas atomization technique were used as starting materials as shown in Figure 4-1 A and B for pure magnesium (< 45 μm) and master alloy (45 - 63 μm) powders, respectively. For pure magnesium powder (Société pour la Fabrication du Magnésium, Martigny, Switzerland), size fractions of < 45 μm were considered due to their higher green density after initial compaction compared to coarser powder size fractions. Calcium was added in the form of a pre-alloyed Mg-10Ca master alloy powder (Zentrum für Funktionswerkstoffe gemeinnützige GmbH, Clausthal, Germany) with a particle size of 45 - 63 μm . The chemical composition of the powders used in the present work is listed in Table 3. The analysis was performed in-house using Flame AAS and Spark AES techniques (see section 4.3) and the compositions indicated in this thesis are in wt.% unless otherwise stated.

Table 3: Elemental composition of the raw powders used in PM processing of Mg-0.6Ca specimens.

Material	Elemental composition [wt.%]							
	Fe	Cu	Ni	Si	Ca	Mn	Zn	Mg
Pure magnesium (as received) (< 45 μm size; $d_{50} = 22 \mu\text{m}$)	0.0018	0.0002	0.0006	0.0221	0.0041	0.0110	0.0027	Bal.
Pure magnesium (sieved condition) (< 45 μm size)	0.0025	0.0004	0.0005	0.0084	0.0051	0.0110	0.0029	Bal.
Master alloy powder; Mg-10Ca (45 - 63 μm size)	0.0021	0.0012	0.0003	0.0200	10.214	0.0150	0.0034	Bal.

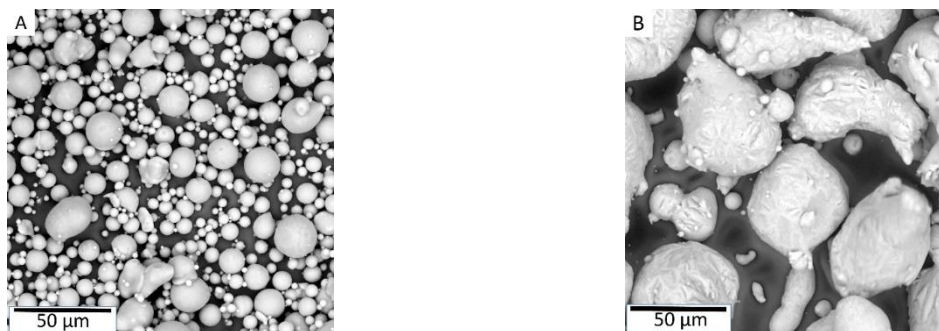


Figure 4-1: Raw powders used in the study. (A) Gas atomized pure magnesium powder with near spherical morphology (B) Mg-10Ca master alloy powder with spherical to ellipsoid morphology. Both powders exhibit fine satellite particles attached to their surfaces. Occasionally powder clusters could be seen.

4.1.2 PM Mg-0.6Ca powder mix preparation

The starting powders indicated in Table 3 are stored in an argon glove box compartment (MBraun, Garching, Germany) operating under Ar 4.6 atmosphere and nearly 5 mbar overpressure relative to atmospheric pressure conditions outside the box. This provides oxygen free atmosphere (oxygen < 5 ppm, water vapor < 0.1 ppm) and safety during handling of the fine powders. The initial Mg-0.6Ca powder mix is produced by blending pure magnesium powder and master alloy powder Mg-10Ca that are mentioned in Table 3, following the rule of mixtures. This means, the production of a certain quantity of Mg-0.6Ca powder mix requires, in weight proportions, 93.87% pure magnesium powder component and 6.13% master alloy (Mg-10Ca) powder component. Distilled cyclohexane was added to this mix followed by manual stirring for 3 - 5 min to obtain a homogeneous gel. The gel was allowed to dry overnight in the argon compartment until further use during compaction. Several batches either 15 g or 20 g of such Mg-0.6Ca powder mixes were prepared to suffice for the number of Mg-0.6Ca specimens required for analysis during the work. In addition to the above-mentioned master alloy particle size of 45 - 63 μm (Table 3), additional master alloy powder particle sizes of < 32 μm and 180 - 250 μm were used at a special instance to produce Mg-0.6Ca powder mix.

The only alloy composition investigated during the framework of the thesis was Mg-0.6Ca that is fabricated by PM technique. This remains unaltered for all the results and analysis produced in this work. However, two slightly different process routes were chosen for producing Mg-0.6Ca powder mixes. These process routes differed in their condition of the used pure magnesium powder during powder mixing step while the condition of master alloy powder remained unaltered. In the first instance, the as-received pure magnesium powder was directly used in producing Mg-0.6Ca powder mix. In the second instance, the as-received pure magnesium powder was subjected to a mechanical sieving treatment (section 4.1.3) and then used to produce Mg-0.6Ca powder mix. The powder mix preparation yet again followed the rule of mixtures mentioned in the previous paragraph. Hereafter, the markers (Mg/Mg-10Ca) and (Mg_{sieved}/Mg-10Ca) will be indicated adjacent to Mg-0.6Ca wherever necessary, to signify the production route of the specimens under scrutiny. Hence, the following terms are presented:

- Mg-0.6Ca (Mg/Mg-10Ca) → Sintered Mg-0.6Ca specimens produced by mixing the as-received pure magnesium powder and Mg-10Ca master alloy powder.
- Mg-0.6Ca (Mg_{sieved}/Mg-10Ca) → Sintered Mg-0.6Ca specimens produced by mixing the mechanically sieved pure magnesium powder and Mg-10Ca master alloy powder.

The additional terms, Mg-0.6Ca powder mix (Mg/Mg-10Ca) and Mg-0.6Ca powder mix (Mg_{sieved}/Mg-10Ca) represent the powder mixes produced by mixing Mg-10Ca powder and pure magnesium powder in its as received and sieved conditions, respectively. It should be noted that the master alloy Mg-10Ca powder remains unaltered and was used in its available gas atomized condition.

4.1.3 Mechanical sieving treatment of as received pure Mg powder

Mechanical sieving was carried out initially to produce pure magnesium powder particles of different sizes. To do this, sieves with openings of 20 μm , 36 μm (Linker Industrie Technik, Kassel, Germany) and 45 μm (Retsch GmbH, Haan, Germany) were placed in a bottom-up fashion with a collecting pan at the very base of a vibrational mechanical sieve shaker (Analysette 3 Pro, Fritsch, Idar-Oberstein, Germany) as shown schematically in Figure 4-2.

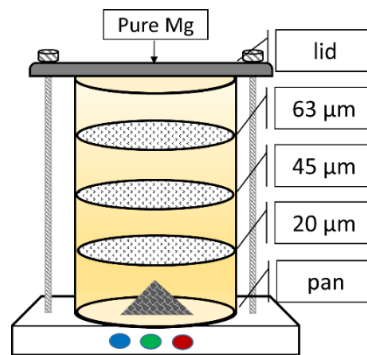


Figure 4-2: Schematic of the vibratory mechanical sieve shaker used for sieving pure magnesium powders in the present study.

During each sieving cycle, approximately 5 g of pure magnesium powder (in its as received condition) with particle size $< 45 \mu\text{m}$ (Table 3) was sprinkled uniformly on the top most sieve. Each cycle lasted for 20 min with 1 mm sieving amplitude inside the argon compartment. After automatic sieving, a manual tapping of the sieves was performed at the end of each sieving cycle to settle down very fine powders sticking to the sieves due to static forces. The sieved powders were stored in the argon compartment until further use. The sieves were cleaned ultrasonically (Elmasonic S50 R, Elma Schmidbauer GmbH, Singen, Germany) with hot water and citric acid combination and vacuum dried until later use. Mg-0.6Ca powder mix produced using these sieved magnesium powders were designated as Mg-0.6Ca powder mix ($\text{Mg}_{\text{sieved}}/\text{Mg-10Ca}$) as indicated in section 4.1.2. Chemical analysis data for pure magnesium powder after mechanical sieving is also shown in Table 3.

4.1.4 PM Mg-0.6Ca green compacts preparation

Two specimen geometries were designed using the dried Mg-0.6Ca powder mixes ($\text{Mg}/\text{Mg-10Ca}$ and $\text{Mg}_{\text{sieved}}/\text{Mg-10Ca}$) from section 4.1.2 and section 4.1.3. Cylindrical specimens of dimensions 11 mm x 11 mm (diameter x height) were fabricated to serve the needs of degradation experiments and microstructure investigations. In addition, pure magnesium cylindrical specimens were prepared for reference during sintering experiments. Micro tensile specimens were produced for mechanical property testing. The green compacts were mechanically hand pressed with a uni-axial load of 100 MPa (1.07 Tonf; Enerpac RC55, Milwaukee, USA) inside the argon compartment (see Figure 4-3 A). Prior to operation, the dies were cleaned off any residual magnesium and dust by treating them with hot water and citric acid combination for 15 min. They were promptly dried with

compressed air gun and stored under vacuum to prevent atmospheric corrosion on the die surfaces. The green compact's dimensions (precision calipers WTN-MS02, Mahr GmbH, Göttingen, Germany) and weights (FZ 300i, A&D Company Limited, Tokyo, Japan) were recorded prior to sintering step. The green compacts are stored in argon compartments prior to sintering.



Figure 4-3: Representative compacts of compressive (immersion test) and microtensile test geometries of PM Mg-0.6Ca specimens. (A) After uni-axial hand pressing prior to sintering. (B) After sintering. The microtensile specimen shown in (B) is cut out from a thicker sintered part and, therefore, does not directly relate to the green part shown in (A).

4.1.5 Sintering process

In the present work, sintering was carried out under high purity argon 6.0 at elevated temperatures to facilitate oxygen free atmosphere and liquid phase activity (MUT RRO350-900, Jena, Germany). The furnace was regularly checked for leakage rates to ensure clean sintering atmospheres. The leakage rates monitored were in the range of $8 \cdot 10^{-5}$ mbar l/s. It was also observed that the recorded sample sintering temperatures were 7-9 °C lower in comparison to set furnace temperatures. Therefore, in the present thesis, the sample sintering temperatures are mentioned. However, it should be noted that the recorded sintering temperatures may still not represent the exact sample sintering temperatures as the position of thermocouple is still not close enough to the actual samples in the current furnace setup as shown schematically in Figure 4-4.

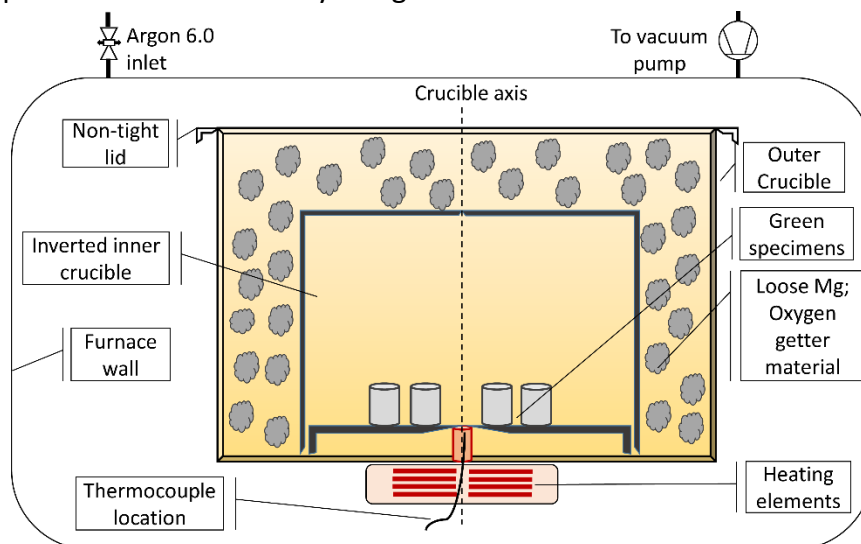


Figure 4-4: Schematic of sintering setup for PM Mg-0.6Ca specimens illustrating basic parts of the crucible.

The sintering run started with a pre-processing step of crucible configuration. The green Mg-0.6Ca powder mix compacts from section 4.1.4 were placed on circular layers inside the square shaped crucible. The layers were surrounded with magnesium oxygen getter material with random particle sizes to entrap oxygen residuals from reaching the samples during sintering. To prevent the samples from getting into contact with the getter material, an inverted crucible was placed over the circular layers. The schematic setup is shown in Figure 4-4. The representative samples after sintering are shown in Figure 4-3 B. The sintering run comprised of three stages as shown in Figure 4-5. The first stage (I) involved gradual heating of the green Mg-0.6Ca powder mix compacts to an intermediate temperature at 10 K/min. The last 100 degrees to the desired sintering temperature were slow heated at 1 K/min to prevent shape distortion in sintered alloy specimens. Heating stage started under vacuum to prevent atmospheric contamination. Prior to heating, the furnace was degassed and purged with argon 4.6 gas. The second stage (II) involved sintering which took place at the desired sintering temperature for 63 h. To generate different porosities in the sample, sintering temperatures were altered as shown in Figure 4-5. The third stage (III) involved furnace cooling of the sintered parts to room temperature.

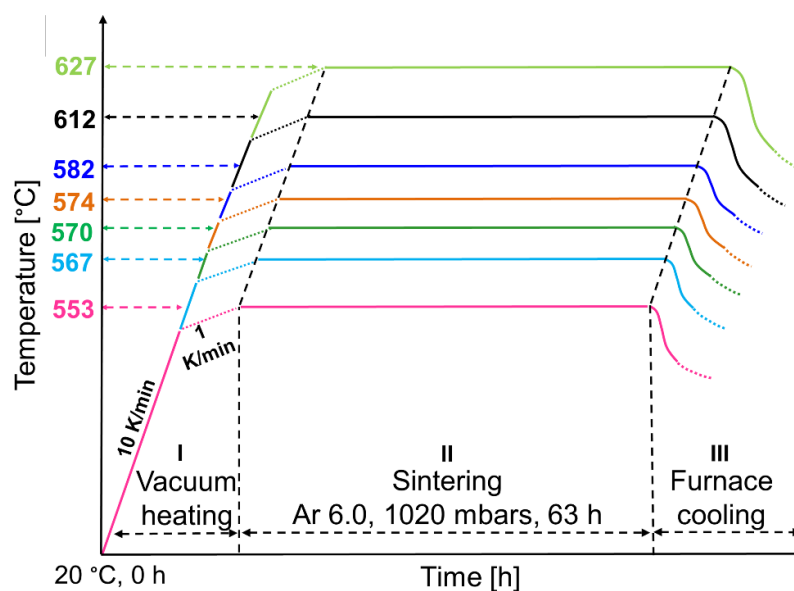


Figure 4-5: Schematic of sintering runs employed to generate porosity in PM Mg-0.6Ca specimens.

4.2 Density and porosity measurements

The geometrical density (ρ_{geo}) was measured using equation (10) after obtaining the volume (V) and mass (M) of sintered porous Mg-0.6Ca specimens. Specimen volume was obtained via the dimensional measurements using calipers (16EX, Mahr Metering Systems GmbH, Göttingen, Germany) and mass was determined using an analytical weighing balance with 0.0001 g precision (LA320S, Sartorius AG, Göttingen, Germany). The percentage error in the measured diameter and length of sintered specimens was less than 1% and 5%, respectively. Specimen porosity (P_{spec}) was then calculated using equation (11). An average for 14 samples was recorded for this purpose. It should be noted that a resublimed

magnesium layer appeared on Mg-0.6Ca specimens after sintering. The intensity and therefore the thickness of this layer increases with increasing temperature of sintering. This increased the dimensions of the sintered specimens compared to the green compacts which is not realistic if specimen shrinkage is to be expected after sintering. Therefore, each sintered Mg-0.6Ca specimen was ground on all sides in a way that shape integrity of the specimens is not lost. Since grinding was manually hand done, errors are to be expected and hence the same is reflected as percentage error in measured diameter and length as mentioned before. Theoretical density value (ρ_{th}) for Mg-0.6Ca alloy used was 1.75 g/cm³ as determined by Helium gas pycnometer (AccuPyc II 1340, Micromeritics GmbH, Aachen, Germany) measured directly on Mg-0.6Ca (Mg/Mg-10Ca) powder mix prior to compaction. In the present work, the fraction of closed pores formed in the specimens of Mg-0.6Ca (Mg/Mg-10Ca) sintered at different temperatures was assessed from their segmented μ CT pore volumes.

$$\rho_{geo} = \frac{M}{V} \quad (10)$$

$$P_{spec} = 1 - \frac{\rho_{geo}}{\rho_{th}} \quad (11)$$

The Archimedes density measurement working on the physical principle of buoyancy (LA320S, Sartorius AG, Göttingen, Germany) was attempted to measure the closed porosity in the alloy specimens. In brief, the Archimedes density measurement takes into account the volume of the displaced fluid (absolute ethanol) which is directly proportional to the apparent change in the weight of the immersed object (sample) from its weight in air. This fluid wets all the accessible pores to the surface and the resultant volume change is due to the upward buoyancy of the closed pores. This leads to an accurate measurement of the closed porosity in the specimens. However, in the present work, application of Archimedes technique to detect closed porosity in highly porous specimens of Mg-0.6Ca (Mg/Mg-10Ca) failed as the obtained closed porosity values in these specimens were slightly negative. This means that a higher specimen density is measured by Archimedes technique than the theoretical density value of Mg-0.6Ca alloy leading to negative closed porosity values in the investigated highly porosity specimens of Mg-0.6Ca (Mg/Mg-10Ca). This, however, is not the case in the specimens of Mg-0.6Ca (Mg/Mg-10Ca) with lower porosities. Due to these ambiguous results from the measurement technique, the formed closed pore fraction of porous specimens investigated in this thesis was assessed from the μ CT data for Mg-0.6Ca (Mg/Mg-10Ca) specimens of each porosity category. The porosities of Mg-0.6Ca (Mg/Mg-10Ca) specimens measured according to equation 11 (geometrical porosity) and measured using Archimedes principle are indicated in the thesis, wherever necessary.

In general, the percentage error in density measurements by Archimedes technique is lower than 0.6%. To calculate porosity from Archimedes measurements it is necessary to know the density of the material with no porosity. An attempt to produce completely dense

Mg-0.6Ca specimens failed when the hot isostatic pressing procedure on low porosity Mg-0.6Ca (Mg/Mg-10Ca) specimens still resulted in residual porosity after the treatment. The use of density values of extruded Mg-0.6Ca specimens with zero porosity was another viable option. But, the presence of oxide on the raw Mg powder surfaces resulted in the formation of oxides in the sintered microstructures which are otherwise not prominent in extruded Mg-0.6Ca specimen microstructures. So, choosing the density values of extruded specimens as the theoretical density value for sintered specimens can be misleading. Archimedes technique for density measurements directly on Mg-0.6Ca powder mix (Mg/Mg-10Ca) is non-practical. For these reasons, in the present work, the measured true density value of Mg-0.6Ca (Mg/Mg-10Ca) powder mix by Helium gas pycnometer (AccuPyc II 1340, Micromeritics GmbH, Aachen, Germany) was taken as the theoretical density of the alloy, which is 1.75 g/cm^3 .

4.3 Elemental composition analysis

Chemical analysis was performed using spark AES (SpectroLAB, SPECTRO Analytical Instruments GmbH, Kleve, Germany) and flame AAS (240 FS AA, Agilent technologies Deutschland GmbH, Waldbronn, Germany). Depending on the constraints in calibration and detection limits, both techniques were employed in determining the elemental composition in Mg-0.6Ca powder mixes and in the sintered Mg-0.6Ca specimens. Specifically, for Ca detections in specimens before and after sintering flame AAS was chosen due to limitations in the element sensitivity with Spark AES.

Flame AAS

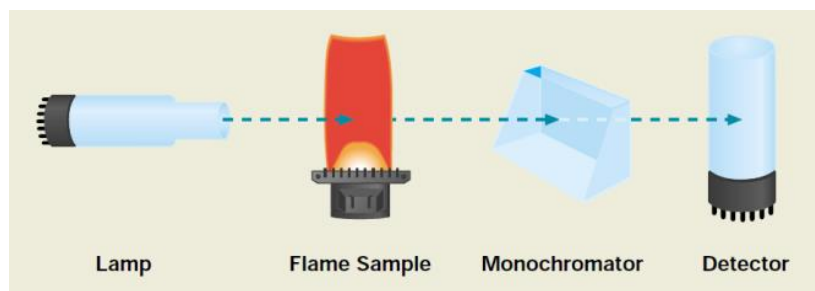


Figure 4-6: Schematic of a single beam flame atomic absorption spectroscopy showing important components of the machine [158].

AAS technique detects the chemical element of interest in the sample by measuring the amount of light absorbed by the element when illuminated using an external lamp source. The cloud of atoms necessary for these measurements are produced by supplying enough thermal energy to the sample so its compounds dissociate into their respective free atoms. This could be easily done by aspirating the solution form of the sample using high strength flames like air-acetylene or nitrous oxide as shown in Figure 4-6. When light passes through such an aspirating solution, the atoms in the ground state are capable of absorbing the analytical wavelength of the light source and get excited. A monochromator is designed

to receive the selected wavelength of light that is characteristic of the element of interest and therefore isolates all the other wavelengths. A detector then compares the transmitted light to that of the incident light and this entity is termed as the absorbance of the sample. Using Beer-Lambert's law, which states a linear relationship between the absorbance and the elemental concentration, the final concentration of the element of interest in the sample is recalculated using the calibration data [159].

In the present work, flame AAS (240 FS AA, Agilent technologies Deutschland GmbH, Waldbronn, Germany) was operated with air-acetylene flame with a flow ratio of 6.75:1. Sample solution feed in rate was 4.8 mL/s through the nebulizer nozzle. Nine seconds of measurement time was given for each sample feed. Both the calibration standards and the sample solutions were normalized for the same magnesium matrix using $\text{MgCl}_2 \cdot 6\text{H}_2\text{O}$ salt solution. The bulk or powder samples (amount in g depending on the element under investigation) were dissolved into the matrix solution by addition of 8 mL Nitric acid (37 vol. %) per 100 mL of prepared sample solution. New methods respective to the elements under determination were written before analysis. A quadratic origin fit is performed on the resulting absorbance values measured for the calibration standards. Calcium was analyzed with 422.7 nm, iron with 248.3 nm, copper with 324.8 nm, nickel with 232 nm specific wavelengths that are generated by hollow cathode lamps in AAS system.

Spark AES

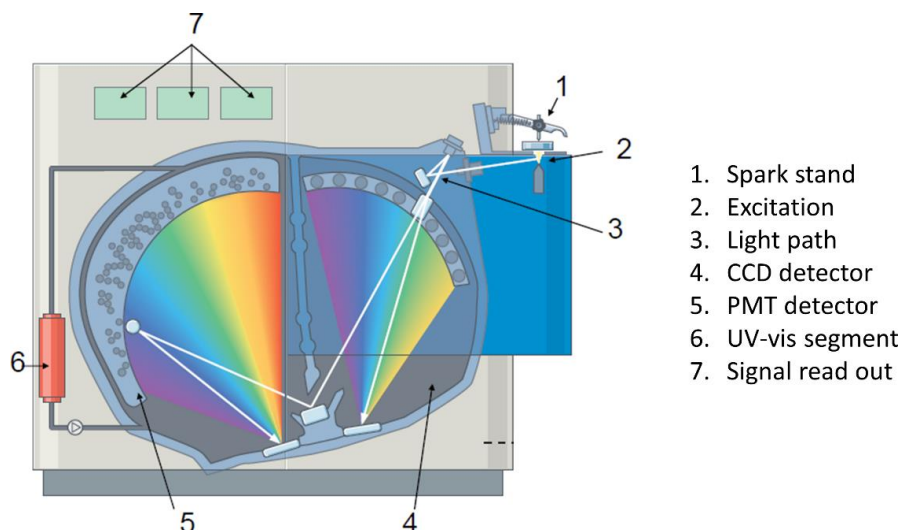


Figure 4-7: Schematic of spark spectrum analyzer indicating basic components of the machine and path of light [160].

Spark AES technique involves the electrical energy in the form of spark generated between the spark tip electrode and the sample to be investigated in presence of an inert gas environment. The generated spark causes vaporization of the sample and the atoms in this high temperature discharge plasma are brought into their excited energy states. The spontaneous decay of atoms to their ground states produces emission spectral lines pertaining to the different energy configurations for each element of the sample. This is

shown as the light path in Figure 4-7. So, a cluster of spectral lines can be generated due to different elements present in the sample making a simultaneous multi-element analysis feasible. A high-resolution spectrophotometer separates these lines into individual spectral components. A charge coupled device (CCD) or a photo multiplier tube (PMT) detector is then used to determine qualitatively the element through the characteristic emission spectra. The intensity of radiation, which is directly proportional to the concentration of the element is then recalculated from the stored set of calibration data [160, 161].

In the present work, the spectrometer (SpectroLAB, SPECTRO Analytical Instruments GmbH, Kleve, Germany) is supplied with a continuous flow of argon gas where plasma is generated at the spark tip to create temperatures (above 4000 K) sufficient for ionizing the elements in the sample. The calibration is performed using two pure magnesium standards (with trace elements of zinc, iron, nickel, silicon, tin, zirconium and yttrium), ZE464, AZ442 and strontium 1.8 standards. For every new calibration performed, the system generates a factor by comparing the obtained intensity values to the manufacturer prescribed default intensity values respective to each element. Ideally this factor should be closer to 1 for a good calibration. The calibration is additionally proved by testing the intensity values and therefore the composition of the known AM50 and AZ91 specimens. This helps also in choosing the required in built system method for performing elemental analysis. The standard deviations arise from the deviations in results within each individual sample analyzed.

4.4 Microscopy analysis

Cold embedding was carried out on the sintered Mg-0.6Ca (Mg/Mg-10Ca) and Mg-0.6Ca (Mg_{sieved}/Mg-10Ca) specimens using Demotec 30 (Demotec, Nidderau, Germany) polymer resin to facilitate microscopic investigation. Samples were then ground using SiC sand papers starting from 500 grit till 4000 grit on an automatic grinding machine (Motopol 2000, Buehler, Lake Bluff, Illinois, USA). Grinding was carried out for 2 min on each sand paper in presence of water. Polishing was performed manually on a microfiber cloth (PT chem S, Clarence Technology GmbH, Wegberg, Germany) with water free solutions of alkaline SiO₂ (0.05 μm particle size in 70% Ethanol) and diamond suspension (0.25 μm particle size in 70% Ethanol). Timely addition of water free lubricant (ethylene to ethylene glycol in 10:1) was carried out to ensure cloth wetness at all times. Depending on the required surface finish, automatic polishing was performed (Kurth Autopol, Industrieservice Siegmund Bigott, Kaarst, Germany) on the ground samples to get rid of mechanical twins. For electron microscope investigations, samples are made conductive using either carbon or silver coatings. Gold sputtering option for improving conductivity was avoided to prevent detection of gold particles (~ 2 μm in size) during electron dispersive x-ray analysis.

Preliminary surface investigations took place with an optical microscope (Olympus PMG3, Tokyo, Japan and Leica DM/LM, Leica Microsystems, Wetzlar, Germany). To investigate the grain boundaries and powder particle surfaces, scanning electron microscopy was employed. Surface profiles were visualized in both secondary electron (SE)

and back scattered electron modes (BSE). Elemental mapping was performed at 15 kV and 15 beam intensity settings (VEGA3 TESCAN, Brno-Kohoutovice, Czech Republic and Phenom PRO-X, Phenom-World BV, Eindhoven, The Netherlands). Field emission SEM equipped with an electron backscattered diffraction detector was used to visualize grain structure via electron backscattered diffraction (EBSD) maps and to obtain images of particle surfaces at a higher resolution (Zeiss Ultra 55, Carl Zeiss AG, Oberkochen, Germany).

Grain size distributions of the sintered Mg-0.6Ca (Mg/Mg-10Ca) and Mg-0.6Ca (Mg_{sieved} /Mg-10Ca) specimens were obtained by analyzing the grain boundaries of both optical microstructures after etching treatment and from the EBSD measurement maps. Firstly, the grain boundaries in the chosen microstructures were marked by hand on an A4 size print. Simultaneously, the visible pores were painted black. The marked A4 print was then scanned at 100 dpi resolution and the saved image '.tiff' file was loaded in software Fiji [162]. This highlights the grain boundaries during image thresholding and prevents background error arising from polishing medium deposited inside the pores. Additionally, the misinterpretation of a large sized pore as a grain can be prevented, which may not possible with the commonly used intercept method for grain size measurements. This is shown in Figure 4-8 A-C, where the same microstructure is shown after hand marking, thresholding and grain analysis using 'analyze particles' plug-in in Fiji software, respectively. Equivalent grain diameters were calculated by the maximum diameter of the circle inscribed for the measured grain area. The presented approach for grain size analysis becomes essential as the sintered microstructures often comprised of pores that are larger than the grains and vice versa. Differentiating these two features requires their careful segmentation along with less interference from left over polishing medium on specimen surface. Therefore, hand marking method for the microstructural features was adopted as the software often ignored this difference when direct images from the microscope were used. Because the image analysis relies on the available pixel information of the microstructural feature, a certain loss in the grain area to its grain boundary was observed which might lead to an underestimate in the measured equivalent grain diameters. This is shown in Figure 4-8 C, where the grain boundary was analyzed by the software as a double line corresponding to the thickness of the marker used during hand marking the grain boundaries. In order to minimize this error, a minimum of 650 grains were analyzed to obtain the grain size distributions.

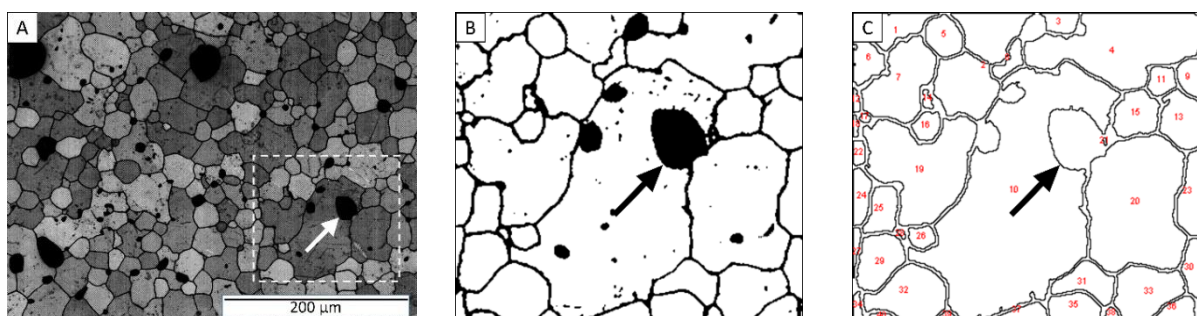


Figure 4-8: Representative microstructure of a sintered Mg-0.6Ca (Mg/Mg-10Ca) specimen possessing 3% porosity with (A) Hand marked grain boundaries and pores, (B) Thresholded image of the inset in (A); matrix (binary value 255), pores and grain boundaries (binary value 0) and (C) Grain areas analyzed using software Fiji [162]. Arrow indicates a pore that has been hand marked in (A) and segmented (B) but not interpreted as a grain during the grain size analysis in (C).

4.5 Computer tomography analysis

Tomography works on the simple principle of x-ray attenuation as they pass through a rigid object. The differences in the x-ray attenuation provided by different material features favor the determination of the density and internal structure analysis of that object. In benchtop μ tomography systems, the object rotates along its longitudinal axis. With the x-ray beam impinging the object, a series of 2D projects is generated using the x-ray intensities at the detector which later can be converted to 3D representation using image reconstruction techniques. The intensity of the incident x-ray beam is diminished according to the following equation [163]:

$$\text{Intensity, } I_x = I e^{-\mu x} \quad (12)$$

Where, I is the intensity of the incident beam, x is the distance from the source, I_x is the intensity of the beam at the distance x from the source, μ is the linear attenuation coefficient.

In the present work, for tomography analysis porous specimens of Mg-0.6Ca (Mg/Mg-10Ca) of approximately 1 mm x 1 mm x 10 mm (length x breadth x height) were machined and specimen surface was prepared using a 4000 SiC sandpaper. Samples were imaged using a Phoenix Nanotom benchtop μ CT (GE inspection and sensing technologies, Wunstorf, Germany) at an operating voltage of 100 kV at 70 μ A current discharge. In total, 2300 projections (2.3 mm length at the center section of the actual specimen) were obtained with an exposure time set to 1500 ms/projection and image averaging set to 4. The effective pixel size was 1 μ m. The detector calibration was performed, which provided the optimization of the image quality. Image acquisition and reconstruction software used was Phoenix Datos|x CT software. After the data reconstruction, image analysis software Fiji [162] and Avizo[®] 9.3.0 (FEI, Thermo Scientific[™], France) were used for 3D characterization of pores. Of the total reconstructed volume, three similar volumes each of 700 μ m x 700 μ m x 500 μ m were chosen for specimens of each porosity category in order to reduce computational time.

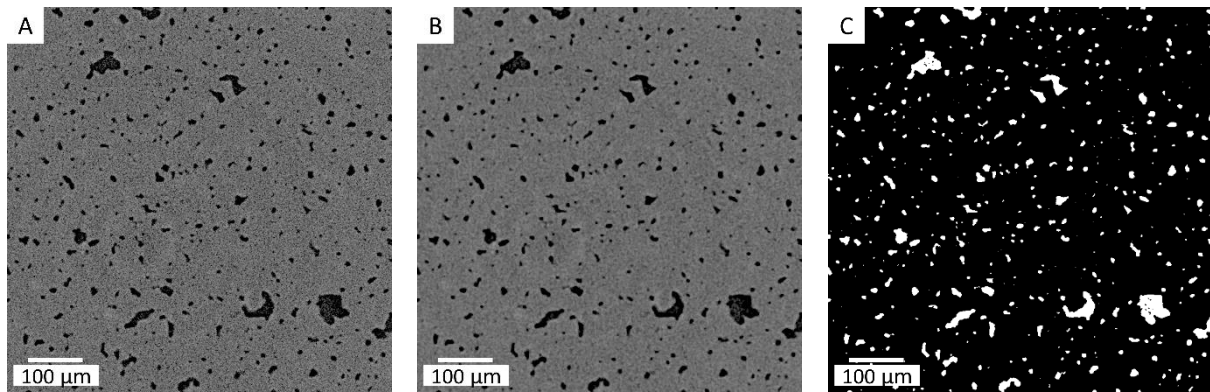


Figure 4-9: Representative μ CT slice/image pertaining to Mg-0.6Ca (Mg/Mg-10Ca) specimen with 12% porosity (A) After reconstruction, (B) After 3D median filtering and (C) After thresholding where the pores are shown in white (binary value 255) and matrix in black (binary value 0).

Image processing started by converting the 32-bit raw data to 8-bit raw data in Fiji, again to reduce the computational time. Three desired tomographic volumes each of $700\ \mu\text{m} \times 700\ \mu\text{m} \times 500\ \mu\text{m}$ were then chosen and a 3D median filter of size $2 \times 2 \times 2$ was applied thereafter. The size of the filter was chosen as a compromise based on reduction in background noise without substantial blurring of the image. This is shown in Figure 4-9 A to B from raw image to median filtered image for specimen porosity of 12% [164]. Thresholding segmentation based on an iterative algorithm IsoData or k-means clustering was performed for pore segmentation. The algorithm calculates the segmentation threshold as mid value of average background and the foreground object pixels. [165]. As an example, the pores after thresholding for specimens with 12% porosity are shown in Figure 4-9 C. After pore segmentation in the desired tomographic volumes, the quantitative parameters of the number of pores and their respective pore volumes were characterized by a two stage connectivity analysis using 3D objects counter plugin in Fiji [166]. For calculating the closed pore fraction, firstly, the volume of the closed pores in the chosen tomographic volume ($700\ \mu\text{m} \times 700\ \mu\text{m} \times 500\ \mu\text{m}$) was computed. This was done by subtracting the pore volumes touching the boundaries (i.e., pores exclusively open to surfaces) from the obtained total pore volume in this chosen tomographic volume. The closed pore fraction was then calculated by dividing this result by the total pore volume. Only the objects greater than $27\ \mu\text{m}^3$ were considered for analysis.

The segmented 8-bit raw data of pores from Fiji was loaded in Avizo[®] 9.3.0 to assess the pore surface curvature and to generate 3D images. The surface morphology of the segmented pores was assessed from their combined Mean and Gaussian curvature distributions [167, 168]. Based on a triangulation approximation, the voxel-based surface of the segmented pores is generated and the local principal radii values (smallest and largest radii of the circle touching all the points on the curved surfaces of the pores) were computed and averaged up to the fifth neighbor. The reciprocal values of these respective local radii yield curvature values k_1 and k_2 , which can be translated into the Mean and Gaussian curvatures using the following equations:

$$\text{Mean curvature, } H = \frac{k_1 + k_2}{2} \tag{13}$$

$$\text{Gaussian curvature, } K = k_1 k_2 \tag{14}$$

A matrix of the mean and Gaussian curvatures is then generated and contour plotted using Origin 2017 software (OriginLab Corporation, Wellesley Hills, USA). Since huge surfaces generate huge data, the number of curvature data points was limited to one million which were selected randomly by a Python script. For the sake of clarity during visual demonstration, the lower frequency limit in the contour plots was manually raised in Origin software so as to obtain a white background.


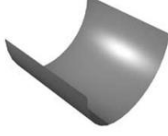






Sign	$K < 0$	$K = 0$	$K > 0$
$H < 0$	<p>Concave saddle In one orthogonal axis the slope increases rapidly (concave) whilst in the other the slope slightly falls away.</p> 	<p>Trough Negative shape of cylinder: In one orthogonal direction there is an increase of slope (concave) whilst in the other there is no slope.</p> 	<p>pit Negative of spheroid shape. Form is concave. The slope increases in all directions.</p> 
$H = 0$	<p>symmetric saddle</p> 	<p>flat surface</p> 	
$H > 0$	<p>convex saddle In one orthogonal axis the slope falls away rapidly (convex) whilst in the other direction the slope slightly increases.</p> 	<p>convex cylindrical Cylindrical shape. In one orthogonal direction the slope falls away (convex) and in the other orthogonal direction there is no slope.</p> 	<p>spheroid Form is convex. The slope falls away in all directions.</p> 

Figure 4-10: Representative shape descriptors that can be assessed from the combined mean and Gaussian curvature values [167]. With permissions from Elsevier.

The negative to positive mean curvature implies a transformation from concave to convex surfaces of the objects. The negative to positive Gaussian curvature indicates a surface shape change from saddle type to spherical or pit type surfaces. The combined 2D histogram representation of the mean and Gaussian curvatures allows for real surface approximation of the measured surfaces as shown in Figure 4-10. Z-axis plot profiling was utilized in Fiji to the segmented data of 1900 μ CT slices which gives an average pixel value across all the segmented slices. In z-axis plot profiling, the pixel value of each segmented slice is obtained as the sum pixel values of black (matrix, 0 value in Figure 4-9 C) and white (pores, 255 value in Figure 4-9 C) areas divided by the total number of pixels. This process is

repeated for each segmented slice throughout 1900 slices and the final average pixel value is measured in an Excel® 2016 spreadsheet. This was performed to check the porosity distribution and therefore pore homogeneity in the produced Mg-0.6Ca (Mg/Mg-10Ca) specimens.

To represent the pores in 3D, firstly, a ‘connected component’ algorithm has been performed on the segmented pore 8-bit raw data. This generates the result spreadsheet of all face-connected pore components along with their respective volume information and center of mass coordinates of their respective locations. This made it feasible to identify the location of the largest pore volume and isolate it from the rest of the pores in the chosen tomographic volume of 700 μm x 700 μm x 500 μm . In addition, iso-surface plugin was used to generate 3D view of all connected pores and of the largest pore volume. The curvature operation was also performed on these generated surfaces. Schematic of the process flow routine in Avizo® 9.3.0 is shown in Figure 4-11.

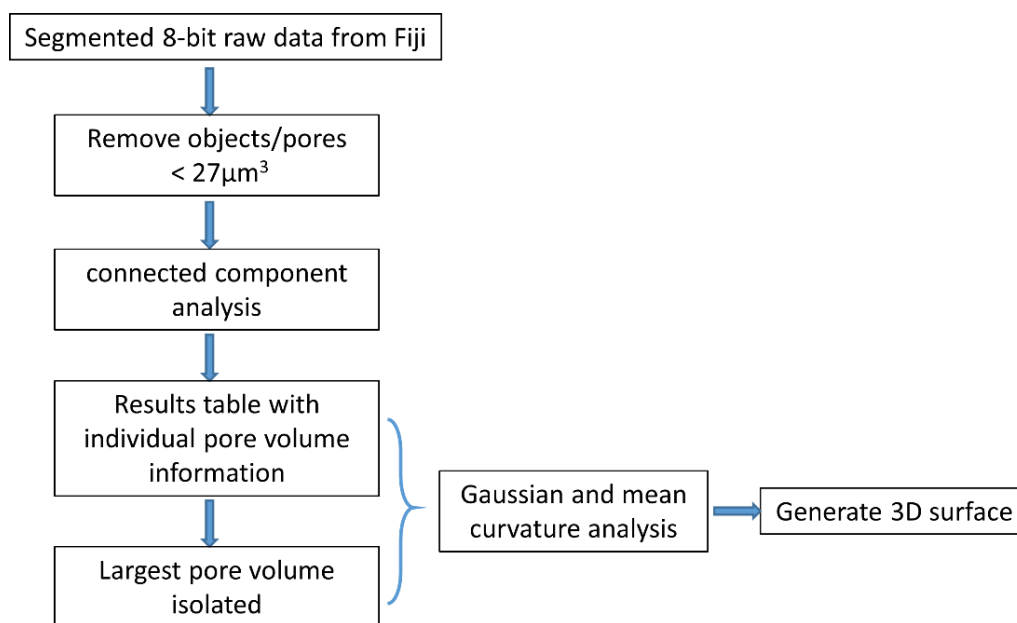


Figure 4-11: Process flow routine employed in Avizo® 9.3.0 software to analyze the pore curvatures and 3D pore structures in Mg-0.6Ca (Mg/Mg10Ca) specimens.

During the present pore characterization, objects smaller than 27 voxels (27 μm^3) were excluded from the analysis. Equivalent pore diameters were determined for the maximum inscribed sphere corresponding to each segmented pore volume. Pore interconnectivity in Mg-0.6Ca (Mg/Mg-10Ca) specimens sintered at different temperatures was calculated using the formula [167]:

$$\text{Pore interconnectivity, } PI = \frac{V_l}{V_t} \quad (15)$$

Where, V_l and V_t are the largest pore volume and total pore volume of the sample, respectively.

4.6 *In vitro* degradation testing

4.6.1 Specimen cleaning and sterilization

After sintering, the specimens of both Mg-0.6Ca (Mg/Mg-10Ca) and Mg-0.6Ca (Mg_{sieved}/Mg-10Ca) in cylindrical form were characterized for their density and porosity as mentioned in section 4.2. At this stage, the specimens were approximately 10 mm in length and diameter as shown in Figure 4-3 B. To produce samples for immersion degradation test, the sintered cylindrical specimens were mounted to the holder of a precision sectioning saw with Diamond wafering blade as a cutting aid in presence of water (Isomet 4000, Buehler, Lake Bluff, Illinois, USA). The rotational speed of the blade was set to 4000 rpm with sample feeding rate of 4 mm/min. The dimensions of the cut samples were approximately 1.5 mm x 10 mm (length x diameter). All surfaces of the cut Mg-0.6Ca specimen discs were further ground using 4000 SiC sandpaper to promote a similar surface profile to all discs. Prior to immersion degradation test, all the cut discs were ultrasonically cleaned (Sonorex RK510S, Bandelin electronic GmbH & Co. KG, Berlin, Germany) using organic solvents such as cyclohexane and acetone for 20 min each and in 70% ethanol for 3 min as a final step. The schematic for the cleaning setup is shown in Figure 4-12. The discs were first introduced into clean glass tubes and approximately 2 mL of organic solvent was later pipetted into these glass tubes. Cleaning treatment proves critical in getting rid of unwanted surface contaminations and other oily substances that could have incurred during previous handling steps. Also, the entire ultrasonic cleaning treatment took place under a protective hood (Vintex Laboreinrichtungen GmbH & Co. KG, Coswig, Germany) to prevent further contaminations and to provide human protection from the organic fumes. After the cleaning treatment, the initial weights of the discs were recorded. Sterilization was performed by immersing the discs in 70% Ethanol for 5 min under the cell culture clean bench (Herasafe, Heraeus Germany GmbH & Co. KG, Hanau, Germany). The discs were later allowed to dry in a new well plate setup under the clean bench atmosphere. After drying, the well plates were filled with the cell culture medium which marks the beginning of immersion degradation test.

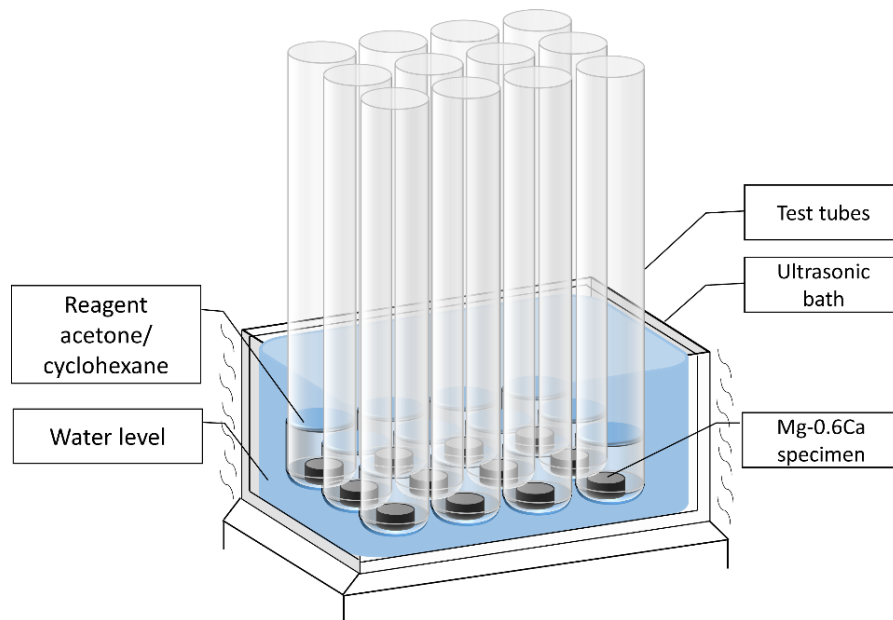


Figure 4-12: Schematic of ultrasonic cleaning procedure for Mg-0.6Ca specimens used in the present work.

4.6.2 Semi static immersion test

The solutions used for immersion degradation test were DMEM + Glutamax cell culture medium (Dulbecco's Modified Eagle's Medium (+ 4.5 g/L D-Glucose, + Pyruvate), 10% Fetal Bovine Serum (FBS), 1% Penicillin Streptomycin (anti-bacterial agent). All the media were taken fresh and mixed under cell culture clean bench atmosphere. About 10 mL of this mix was stored in the incubator (BBD 6220, Thermo Fischer Scientific, Langensfeld, Germany) for 24 h to serve as the control medium.

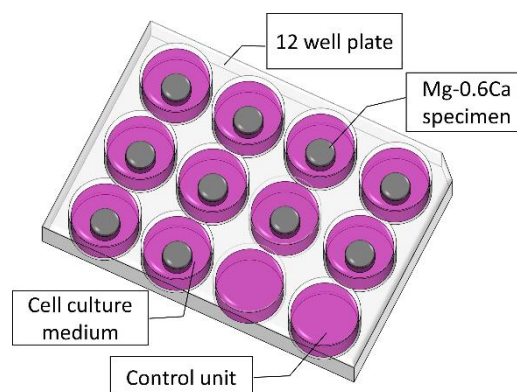


Figure 4-13: Schematic of immersion degradation test setup for Mg-0.6Ca specimens used in the present work.

Medium contaminations were visually inspected with a light microscope after this incubation stage. After the contamination check, the sterilized Mg-0.6Ca discs were introduced with the fresh medium; 2 mL/well. Additionally, a control medium is included for every incubation period as shown in Figure 4-13. Incubation of these well plates took place under physiological cell culture conditions of 37 °C, 20% O₂, 5% CO₂, 95% relative humidity.

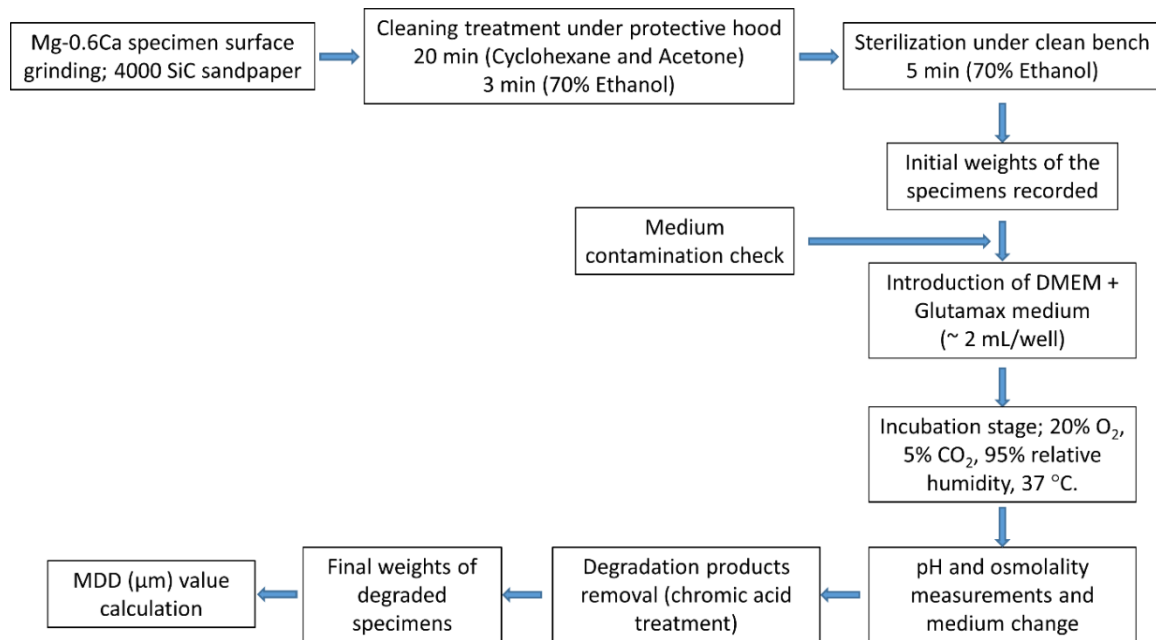


Figure 4-14: Flow sheet of immersion degradation test used for Mg-0.6Ca specimens in the present work.

The test was carried out for nearly 16 days. On every alternate day, 1 mL of medium extract was collected from the well plates containing the Mg-0.6Ca discs and of the control units to evaluate the change in pH and osmolality values during the incubation time. Simultaneously, the remaining wells with alloy specimen discs were supplied with fresh medium to prevent medium saturation and therefore preventing an increase in pH. Two discs were taken out of the test setup every alternate day to evaluate for their mass loss and degradation characteristics. The discs were washed in double distilled water and in absolute ethanol and were promptly dried to prevent layer buildup which may not be a direct result of the exposed cell culture medium under incubation conditions. At this stage, the mass of the discs with degradation layer was recorded.

Chromic acid treatment was performed in two different instances. First, to investigate the direct effect of the acid on the bare Mg-0.6Ca discs and the second, to remove the degradation layer after successive incubation steps. To remove the degradation products after immersion test, samples were treated with chromic acid for 20 min (180 g/L in distilled water, VWR International, Darmstadt, Germany) followed by cleaning with ethanol and distilled water. All surfaces of the discs were equally exposed to the acid by inverting the specimens after 10 min during the chromic acid treatment. Should the discs be stored until further use, they were placed in the cabinet with reduced pressure of 200 mbars at 37 °C. After this treatment, dry chromic acid remained on the certain degraded surfaces, especially in specimens with porosities 18% and 21%, leading to a certain increase in the weights of these specimens. This was corrected by recording the weight increase in specimens belonging to these porosities when they were directly exposed to chromic acid for 20 min, at a different instance. This increase in the mass of the specimens after chromic acid,

however, was not observed in specimens with porosities $\leq 12\%$. In general, no direct chemical interaction between the specimens and the acid is observed as no mass change is observed in specimens with porosities $\leq 12\%$. The mass of the formed degradation layer was measured as the difference in sample mass with the degradation layer and after subsequent chromic acid treatment. The schematic representation of the semi static immersion test procedure is shown in Figure 4-14. Mean degradation depth (MDD) h (in μm) was calculated using the following formula:

$$MDD, h = \frac{\Delta m \cdot 10^4}{A \cdot \rho} \quad (16)$$

Where, Δm is the mass loss difference before and after degradation (g), A is the total surface area of the specimen (cm^2), ρ is the density of the material under investigation (g/cm^3). According to the present approach, the mean degradation rate (MDR) ($\mu\text{m}/\text{d}$) is obtained as the slope value from the linear regression line fitted to the experimental data. For the sake of comparison to the existing literature, the MDR values are presented in mm/year . Linear regression was fitted using Origin 2017 software.

4.6.3 Medium extract analysis

As mentioned in section 4.6.2, 1 mL of the medium extract was taken from the wells with Mg-0.6Ca discs and without the discs (control units) to perform pH (Sentron SI 600 pH meter, Sentron Europe BV, VD Leek, The Netherlands) and osmolality measurements (Osmomat Auto, Genotec mbH, Berlin, Germany). This was performed after every incubation period up to 16 days to assess the progress of degradation. Physiological conditions require pH in the range of 7.8 - 8.1. Hence, to verify the same within the present experimental setup, pH was measured on approximately 950 μl medium extract. Three-point calibration was performed using NIST buffer set calibration solutions of pH value 4, 7 and 10. Osmolality measurements of the medium extract often provide a direct correlation to the degradation progress by calculating the depression in freezing point of the extract medium (with salts) compared to that of double distilled water (without salts). Approximately, 50 μl of the medium extract was input to a cryogenic Osmometer. Calibration was performed using 0.300 Osmol/kg NaCl/ H_2O solution. The measured pH and osmolality values of freshly prepared cell culture media (prior to immersion test start) with added supplements was nearly 7.2 and 0.340 Osmol/kg, respectively. Both measurements were performed ex situ.

4.7 Mechanical property testing

The micro tensile specimens were produced following a similar structure as in section 4.1.4 except that the dimensions of the cut specimens were different. The final specimen geometries were 1 - 1.2 mm (cross sectional thickness) x 2 - 2.3 mm (cross section length at the center of the specimen) and 4.5 - 4.7 mm (cross section length at the head of the specimen). All micro tensile specimens were ground with 1000 SiC sand paper for uniform

surface profiles prior to tensile testing. Tensile tests for Mg-0.6Ca specimens were performed according to DIN EN ISO 6892-1:2009 on 5 samples. The elongation during the test was monitored using a laser extensometer (Fiedler Optoelektronik GmbH, Lützen, Germany) within an initial marked gauge length of approximately 10 mm. Strain rate was set to 0.2 mm/min in a load cell of 5kN (Zwick Roell Z005/ TH2A modell, Zwick Roell GmbH & Co. KG, Ulm, Germany).

5 Results

5.1 Chemical analysis of PM Mg-0.6Ca specimens

The measurement techniques for elemental analysis in porous PM Mg-0.6Ca specimens are described in section 4.3. Table 4 quantifies the elemental concentrations in the investigated PM Mg-0.6Ca specimens prior to immersion degradation test. The measured concentrations for iron, copper and nickel in the sintered specimens are lower than 30 ppm, 25 ppm and 15 ppm respectively, except for Mg-0.6Ca specimens sintered at 567 °C, which showed average copper concentrations nearing 34 ppm. A wide range of silicon concentrations between 130 - 330 ppm are detected in the investigated specimens. It has to be noted that these concentrations are comparable to the starting powders shown in Table 3, indicating clean powder handling and sintering atmospheres. Aluminum concentrations obtained from spark AES technique are not reported here due to the non-reliability in measurements that arise because of the specimen holding plate being made from alumina material.

Table 4: Calcium and impurity element concentrations (n= 3/category) of Mg-0.6Ca (Mg/Mg-10Ca) and Mg-0.6Ca (Mg_{sieved}/Mg-10Ca) specimens in their sintered condition.

Specimen condition	Sintering temperature [°C]	Specimen porosity [%]	Flame AAS [wt.%]		Spark AES [ppm]		
			Ca	Fe	Cu	Ni	Si
Mg-0.6Ca (Mg/Mg-10Ca)	553	21 ± 2	0.64	18 ± 5	18 ± 3	< 2	332 ± 86
	567	18 ± 1	-	9 ± 5	34 ± 7	< 2	160 ± 29
	570	12 ± 2	-	8 ± 1	9 ± 3	4 ± 2	138 ± 27
	574	10 ± 2	0.67	14 ± 4	12 ± 8	9 ± 3	163 ± 9
	582	8 ± 1	-	20 ± 1	11 ± 1	9 ± 1	234 ± 7
	612	6 ± 1	-	22 ± 4	14 ± 3	7 ± 2	191 ± 34
	627	3 ± 1	0.63	20 ± 4	12 ± 1	7 ± 2	157 ± 37
Mg-0.6Ca (Mg _{sieved} /Mg-10Ca)	627	3 ± 1	0.62	20 ± 9	23 ± 13	6 ± 4	220 ± 57

The average calcium contents in PM Mg-0.6Ca powder mix (before sintering), which was compiled according to rule of mixture as in section 4.1.2, is 0.59 wt.% when measured by flame AAS. These measured calcium values in the powder mixes, however, are lower than expected even with an actual calcium content of 10.214 wt.% in the used master alloy as indicated in Table 3. The calculation yields approximately 0.626 wt.% calcium in the resulting PM Mg-0.6Ca powder mix when 10.214 wt.% calcium is used during powder mix

compilation. However, in reality it was measured to be 0.59 wt.% by flame AAS. This deviation in calcium content from the calculated to realistic values in PM Mg-0.6Ca powder mix indicates the possibility of powder losses during handling. With several batches of the produced powder mixes yielding nearly 0.59 wt.% calcium, it can be inferred that powder mixing is, in general, still successful.

After sintering, however, an increase in the overall calcium content is observed as shown in Table 4 for Mg-0.6Ca (Mg/Mg-10Ca) specimens at specific sintering temperatures and in Mg-0.6Ca (Mg_{sieved}/Mg-10Ca) specimens. As indicated in section 4.2, a resublimed magnesium deposit was observed on the specimen surfaces after sintering. The main sources of magnesium available at the specimen vicinity for this deposition to take place are the specimen itself and the loose oxygen getter material surrounding the specimen crucible. However, this layer was removed for all specimens by manual grinding (section 4.2). Therefore, the increase in calcium content in specimens after sintering is due to a possible decrease in the bulk magnesium concentration in the specimens. As a side note, calcium losses that may have incurred during long sintering runs cannot be discerned from the shown chemical analysis measurements.

5.2 Density development with sintering temperature

Sintering setup and furnace operations are detailed in section 4.1.5. The results of relative sinter densities achieved in Mg-0.6Ca (Mg/Mg-10Ca) specimens depending on the choice of sintering temperatures are shown in Figure 5-1 A. It is evident that low sintering temperatures resulted in low relative sinter densities in Mg-0.6Ca (Mg/Mg-10Ca) specimens. Relative sinter densities are also observed to increase with increasing sintering temperatures. It is also apparent that the green compacts soon after initial compaction at 100 MPa, possess nearly 77% relative density values (1.35 - 1.38 g/cm³ actual density values). This high reproducibility in green densities can be attributed to the use of fine powders during PM Mg-0.6Ca powder mixing as in section 4.1.2. The green density values of pure magnesium reference specimens used in the present study are also in the range of 1.37 - 1.38 g/cm³. It should be noted that the relative sinter densities presented in Figure 5-1 are measured geometrically using specimen dimensions and weight. The high scatter in density values after sintering arises due to the error in specimen thickness measurement resulting from the removal of resublimed magnesium layer developed on specimen surfaces after sintering, as mentioned in section 4.2.

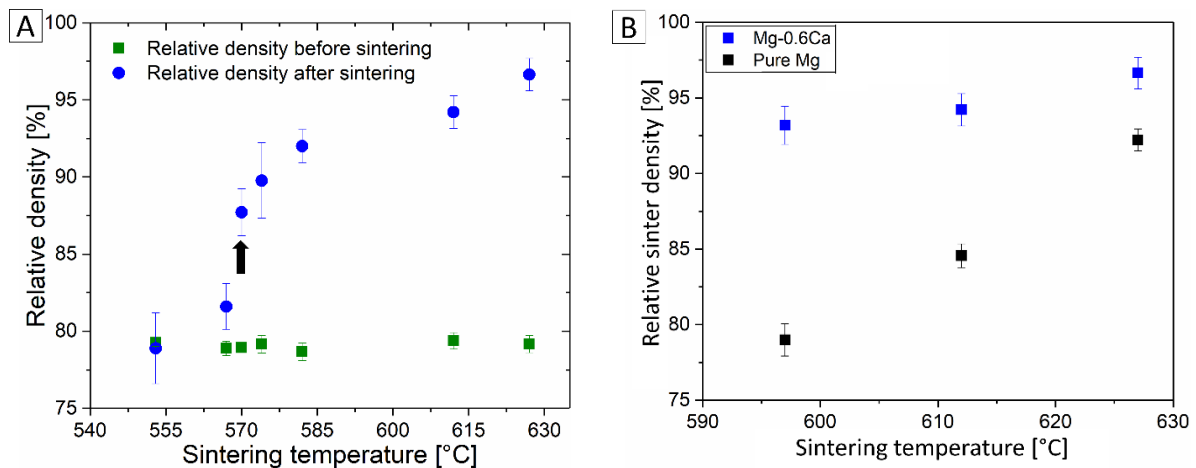


Figure 5-1: (A) Relative density change before and after sintering of porous Mg-0.6Ca (Mg/Mg-10Ca) specimens as a function of sintering temperature. (B) Comparison of relative sinter densities between pure magnesium reference specimens and Mg-0.6Ca (Mg/Mg-10Ca) specimens under same sintering conditions. Arrow in (A) indicates the sharp increase in specimen density after sintering at 570 °C.

A notable feature in Figure 5-1 A is the increase in relative sinter density by nearly 7% with an increase in sintering temperature from 567 °C to 570 °C. The relative density increase in other successive temperature ranges is about 2% - 3%. Though this temperature is not the exact specimen temperature, this is the closest distance the thermocouple in furnace operation can get to the specimens in the employed furnace setup (Figure 4-4). The time of sintering and sintering atmosphere in all the furnace runs concerning Figure 5-1 A remain the same i.e., 63 h and Ar 6.0 atmosphere, respectively. Figure 5-1 B shows the increment in relative sinter densities at different sintering temperatures with and without the presence of calcium in magnesium. Figure 5-1 B indicates that the relative sinter densities of 78% achieved by pure magnesium specimens at sintering temperatures of 595 °C are still comparable to their green density values. At the highest sintering temperature of 626 °C used in the present study, pure magnesium densified to nearly 93% theoretical density compared to Mg-0.6Ca specimens that sinter to nearly 97% relative density under same conditions.

Figure 5-2 shows the changing trend in the measured specimen porosity and the closed pore fraction (assessed from μ CT data) as the function of sintering temperature in Mg-0.6Ca (Mg/Mg-10Ca) specimens. With increasing sintering temperature, the total porosity decreased. The drop in the total porosity between 567 °C and 570 °C corresponds to the increase in relative sinter density shown in Figure 5-1 A (arrow pointer). The closed pore fraction, on the other hand, also starts to develop at sintering temperature of 570 °C and increases thereafter with increasing sintering temperature. A significant closed pore fraction nearing 55% forms at sintering temperature of 570 °C and increases to > 10% at 627 °C sintering temperature.

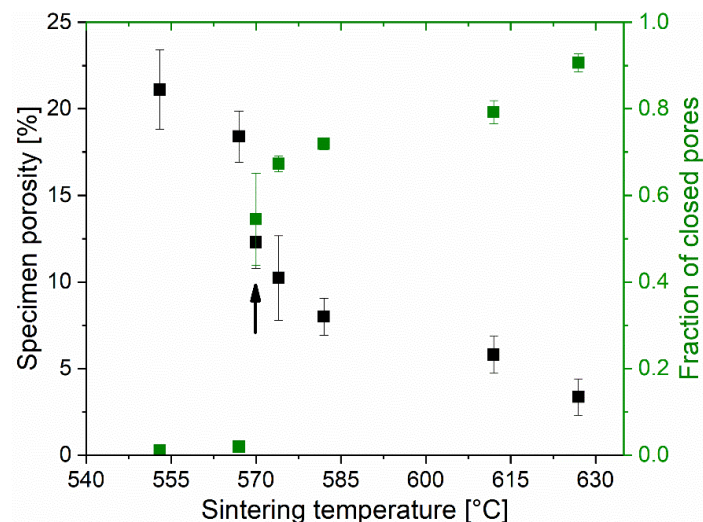


Figure 5-2: Fraction of closed pores formed and specimen porosity change as a function of sintering temperature in porous Mg-0.6Ca (Mg/Mg-10Ca) specimens. Arrow indicates the sharp increase in the closed pore fraction at 570 °C.

5.3 Microstructures of PM Mg-0.6Ca (Mg/Mg-10Ca)

Figure 5-3 shows the overview optical images of sintered Mg-0.6Ca (Mg/Mg-10Ca) specimens. It is evident that the porosity is concentrated mainly at the particle boundaries. 2D pore shape is visually highly convoluted. Pores in the grain interiors are rarely found in the sintered microstructures indicating good quality of the raw powders with low internal defects. Sintering at low temperatures led to an interconnected pore structure as shown in Figure 5-3 A and B. Certain pore closure can be visualized at sintering temperature nearing 570 °C and is more pronounced at sintering temperatures ≥ 574 °C as shown in Figure 5-3 E to G. It can be seen that in Figure 5-3 C and D, more single large pores are visible compared to optical microstructures in Figure 5-3 E to G. No significant change in the nature or the shape of pores can be discerned from the optical microstructure images at sintering temperatures ≥ 582 °C in Figure 5-3 E to G. At the chosen magnification for optical imaging, no clear secondary phases are also distinguishable. All sintered microstructures, however, showed convex shaped grains with distinguishable grain boundaries. In Figure 5-3 E to G, porosity further decreased (Figure 5-2) and only occasionally large pores are found with a considerable decrease in the overall pore sizes. Microstructural features in these specimens appear similar with specimen porosities 8%, 6% and 3%. The average grain size value (~ 30 μm) is only slightly higher than the d_{50} value of the initial pure magnesium powders (Table 3) used in the powder mixing production step in section 4.1.2.

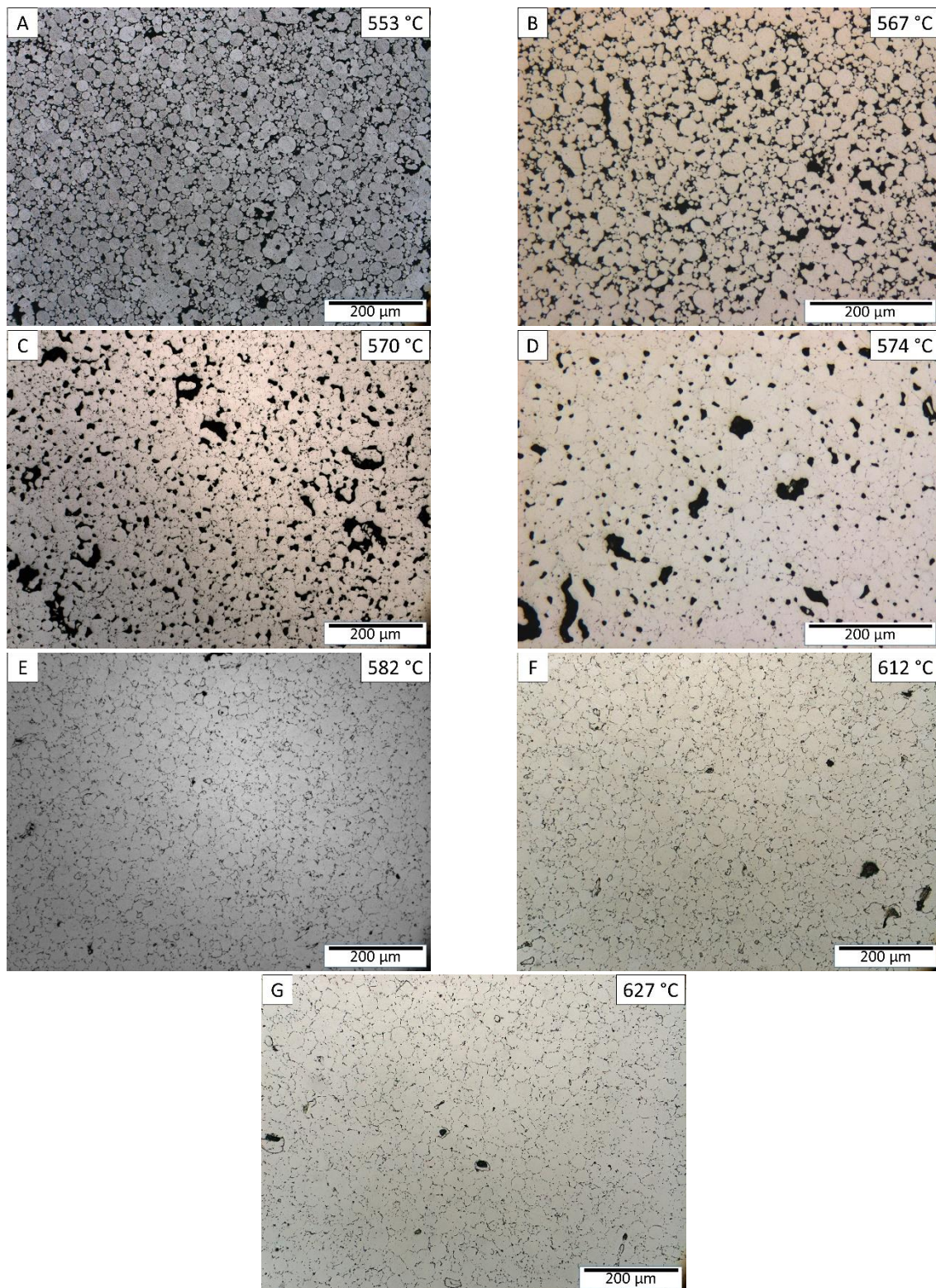


Figure 5-3: Representative optical images of sintered Mg-0.6Ca (Mg/Mg-10Ca) specimens with porosities of (A) 21%, (B) 18%, (C) 12%, (D) 10%, (E) 8%, (F) 6% and (G) 3%. Specimen sintering temperatures are mentioned in respective images.

Electron microscopy images show the confirmation of particle necks in sintered specimens at temperature 553 °C as in Figure 5-4 A and Figure 5-6 A for specimens with 21% porosity. At sintering temperatures > 570 °C, numerous small pores appear between particle

boundaries as shown in Figure 5-4 B to D. The evolved pore morphology appears irregular, however, rounding of small pores is evident at intermediate sintering temperatures of 570 °C and 574 °C as shown in Figure 5-4 B and C, amidst a few large pores. At high sintering temperatures nearing 627 °C, a near spherical pore morphology is visible as in Figure 5-4 D.

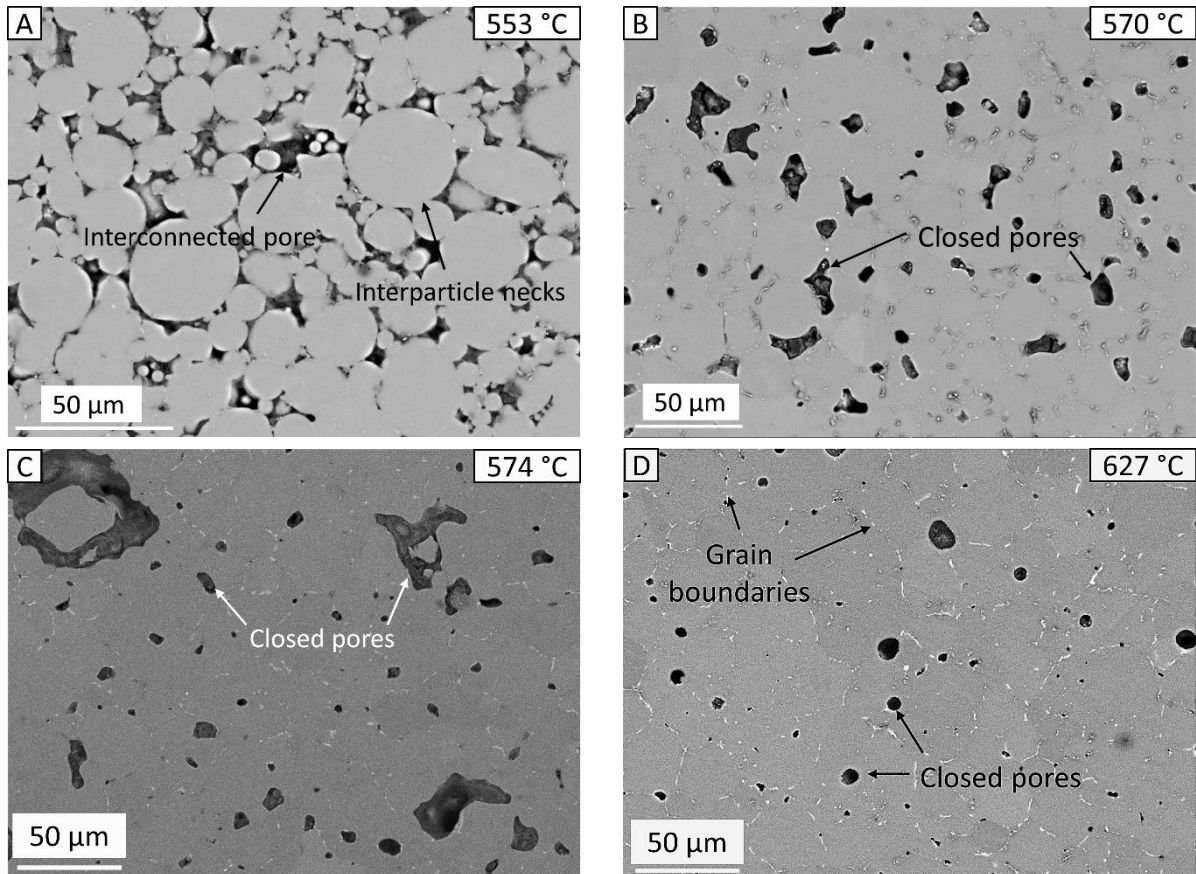


Figure 5-4: BSE images indicating the pore nature and phases formed in Mg-0.6Ca (Mg/Mg-10Ca) specimens with porosities of (A) 21%, (B) 12%, (C) 10% and (D) 3%. Specimen sintering temperatures are mentioned in respective images.

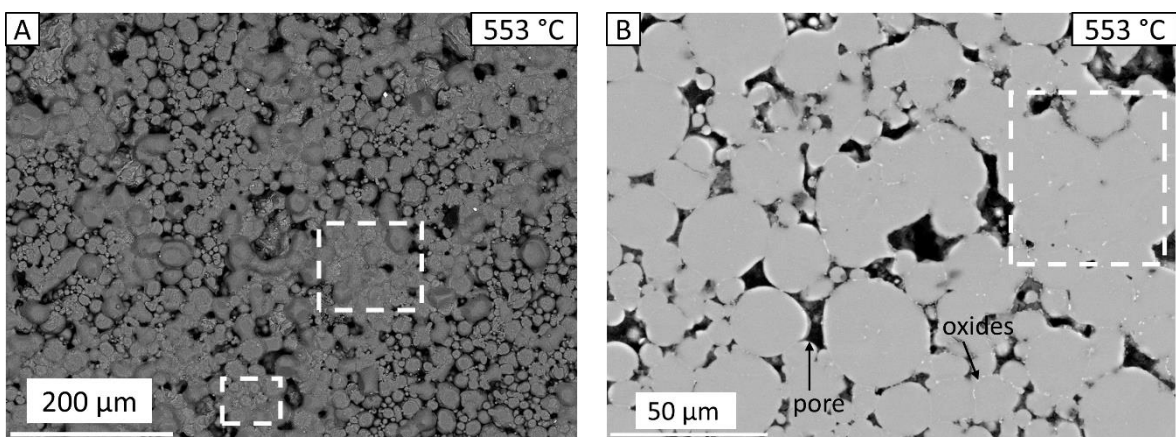


Figure 5-5: BSE images of Mg-0.6Ca (Mg/Mg-10Ca) specimens 21%. White boxes indicate dense regions within the same cross section of the specimen.

In the same cross section of the polished specimen, regions with higher densities are witnessed in specimens with low relative sinter densities. Example of these regions are highlighted in the white boxes in Figure 5-5 A and B, where the specimens are sintered at 553 °C for 63 h duration. This behavior disappears at sintering temperatures ≥ 570 °C and homogeneous microstructures are observed as in Figure 5-4 C and D.

Energy dispersive x-ray analysis on polished specimen surfaces indicates the presence of calcium rich phase and oxide particle arrangement along the grain boundaries as shown in Figure 5-6 A to D. The stoichiometrically favorable Mg/Ca phase at room temperature according to the Mg-Ca phase diagram (Figure 2-4) is Mg_2Ca . The composition of this Mg_2Ca phase in the present work, however, is identified approximately as 17.6 wt.% (oxygen), 18.6 wt.% (silicon), 22 wt.% (calcium) and rest (magnesium) by EDX analysis. Oxygen and silicon are probably detected due to polishing medium containing silica particles that can be embedded around the precipitate phase during polishing. The Mg_2Ca bright phase is not continuous along all grain boundaries but is bigger in size compared to adjacent oxide particles (Figure 5-6 C and D).

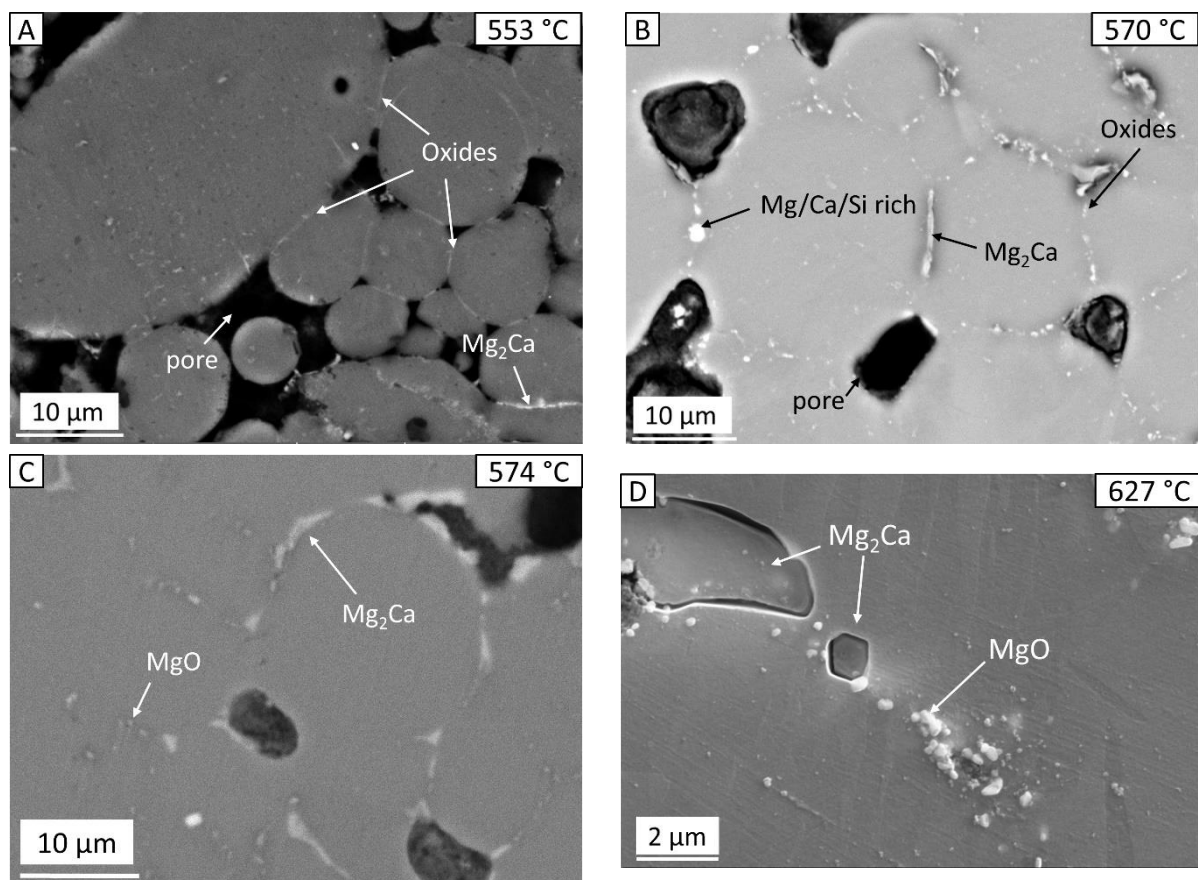


Figure 5-6: Electron microscopy images of Mg-0.6Ca (Mg/Mg-10Ca) specimens with porosities of (A) 21%, (B) 12%, (C) 10% and (D) 3% indicating different phases formed with evolving pore morphology. Images are taken using BSE mode except for image (D), which is in SE mode.

Certain grain boundaries are enriched by the presence of MgO and low Mg_2Ca precipitates as shown in Figure 5-6 A. The composition of MgO phase by EDX analysis

showed < 2 wt.% (oxygen), 0.04 wt.% (silicon), 0.2 wt.% (calcium) and rest (magnesium). The disparity in composition away from the stoichiometric composition is likely due to small MgO particle sizes and huge interaction volume of the electron beam with magnesium matrix. The microstructures of sintered Mg-0.6Ca (Mg/Mg-10Ca) specimens also reveal the presence of Mg/Ca/Si rich phases in grain boundaries and in grain interiors. This phase occurs at random sites with varying sizes and mostly convoluted morphology. The composition of Mg/Ca/Si phase is approximately 4.1 wt.% (oxygen), 28.5 wt.% (silicon), 38.4 wt.% (calcium) and rest (magnesium) as determined by EDX analysis.

5.4 Tomography evaluation of PM Mg-0.6Ca (Mg/Mg-10Ca)

Number of pores formed

Pore characterization on similar sample volumes (700 μm x 700 μm x 500 μm) in all Mg-0.6Ca porosity levels revealed that both high and low porous specimens possess a smaller number of pores. This means that specimens with high porosities of 18% and 21% possibly possess larger connected pores due to the visible inter particle necks after sintering as shown in Figure 5-4 A. Hence, a lower pore count is detected in these specimens. In specimens with 3% porosity, the number of pores detected is inherently low owing to the thermal activity during sintering. However, this low pore count can be also due to small pores that shrank further during high temperature sintering but are not detected due to the limiting voxel size of 27 μm^3 during tomographic characterization. Maximum pore counts are measured for samples sintered at 582 °C in specimens with 8% porosity.

Table 5: Quantitative pore parameters obtained from three different μCT volumes (each of 700 μm x 700 μm x 500 μm) of porous Mg-0.6Ca (Mg/Mg-10Ca) specimens sintered at different temperatures.

Sintering temperature [°C]	Specimen porosity [%]	Quantitative pore parameters		
		Average pore interconnectivity [%]	Average pore number	Average pixel value measured across 1900 μCT slices [pixel]
553	21 \pm 2	98.4 \pm 0.2	3718 \pm 300	52.2 \pm 2.0
567	18 \pm 1	97.0 \pm 0.4	3953 \pm 417	48.4 \pm 1.3
570	12 \pm 2	7.4 \pm 3.1	11046 \pm 406	27.1 \pm 2.0
574	10 \pm 2	4.8 \pm 1.6	14472 \pm 1156	20.8 \pm 2.2
582	8 \pm 1	3.1 \pm 1.3	16929 \pm 779	16.7 \pm 2.2
612	6 \pm 1	2.2 \pm 0.5	15368 \pm 334	10.0 \pm 1.8
627	3 \pm 1	3.8 \pm 1.3	1290 \pm 459	1.5 \pm 0.6

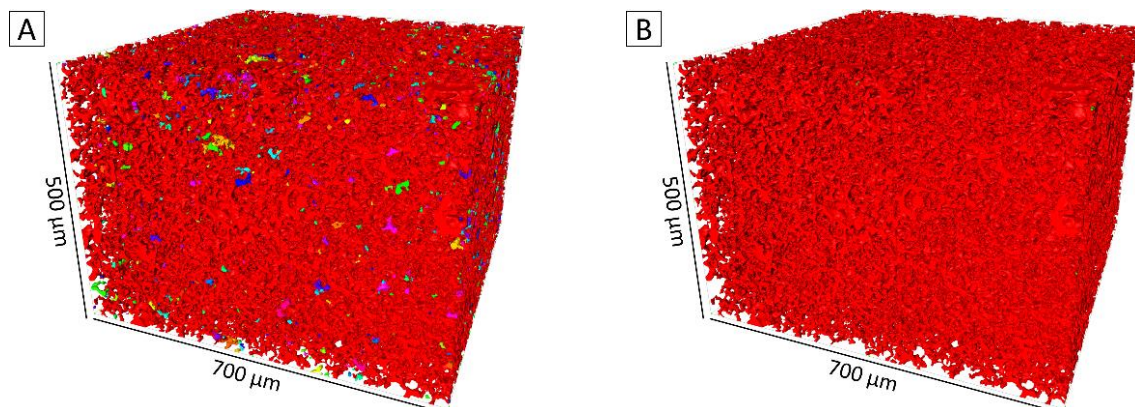
Mostly, an increasing tendency in the pore count can be observed with decreasing specimen porosity with increasing sintering temperature. Visually this can also be observed in the optical images as in Figure 5-3. It should be noted that in Table 5 the average number

of pores formed may be slightly exaggerated due to similar tomographic volumes chosen for pore characterization in porous Mg-0.6Ca (Mg/Mg-10Ca) specimens despite their differences in the actual dimensional shrinkages due to the choice of different sintering temperatures.

Pore interconnectivity and pore homogeneity

In most cases, the measured pore interconnectivity is lower than 10% in Mg-0.6Ca specimens with porosities $\leq 12\%$ (i.e., specimens sintered at temperatures ≥ 570 °C, Table 5). Specimens with porosities 18% and 21% showed a dramatic increase in their pore interconnectivity with values $> 95\%$. This provides evidence that the small pores visualized in Figure 5-4 A between sintered particles are actually contributing to 3D pore networks. The pore isolation observed in specimens with $\leq 12\%$ as in Figure 5-4 B to D correlates to the observed decrease in pore interconnectivity in Table 5. In specimens with 12% porosity, a high error value for pore interconnectivity is observed compared to the specimens with porosities $\leq 10\%$. Since similar tomographic volumes are chosen for μ CT evaluation, this high error in 12% porous specimens indicates the inherent error brought out by the pore closure leading to variation in formed pore volumes.

A low pore interconnectivity does not necessarily indicate pore homogeneity in the investigated Mg-0.6Ca specimens. The pore homogeneity is revealed by the deviations in the average pixel value of the segmented images (see section 4.5) across the entire length of the investigated specimens. These values in Table 5 (last column) show that the measured pixel values across 1900 μ CT slices deviate not more than 3 pixels at all Mg-0.6Ca specimen porosity categories. This means a homogeneous pore distribution existing in the produced porous Mg-0.6Ca specimens. The decrease in average pixel values from nearly 52 to 2 in Table 5 is due to the high and low porosities relating to the specimens with 21% and 3% porosities, respectively. Certain dense regions shown in 2D SEM images (Figure 5-5; white boxes) for specimens with 21% porosity seem not to affect the pore homogeneity of the overall specimen (low deviation in the average pixel value in Table 5).



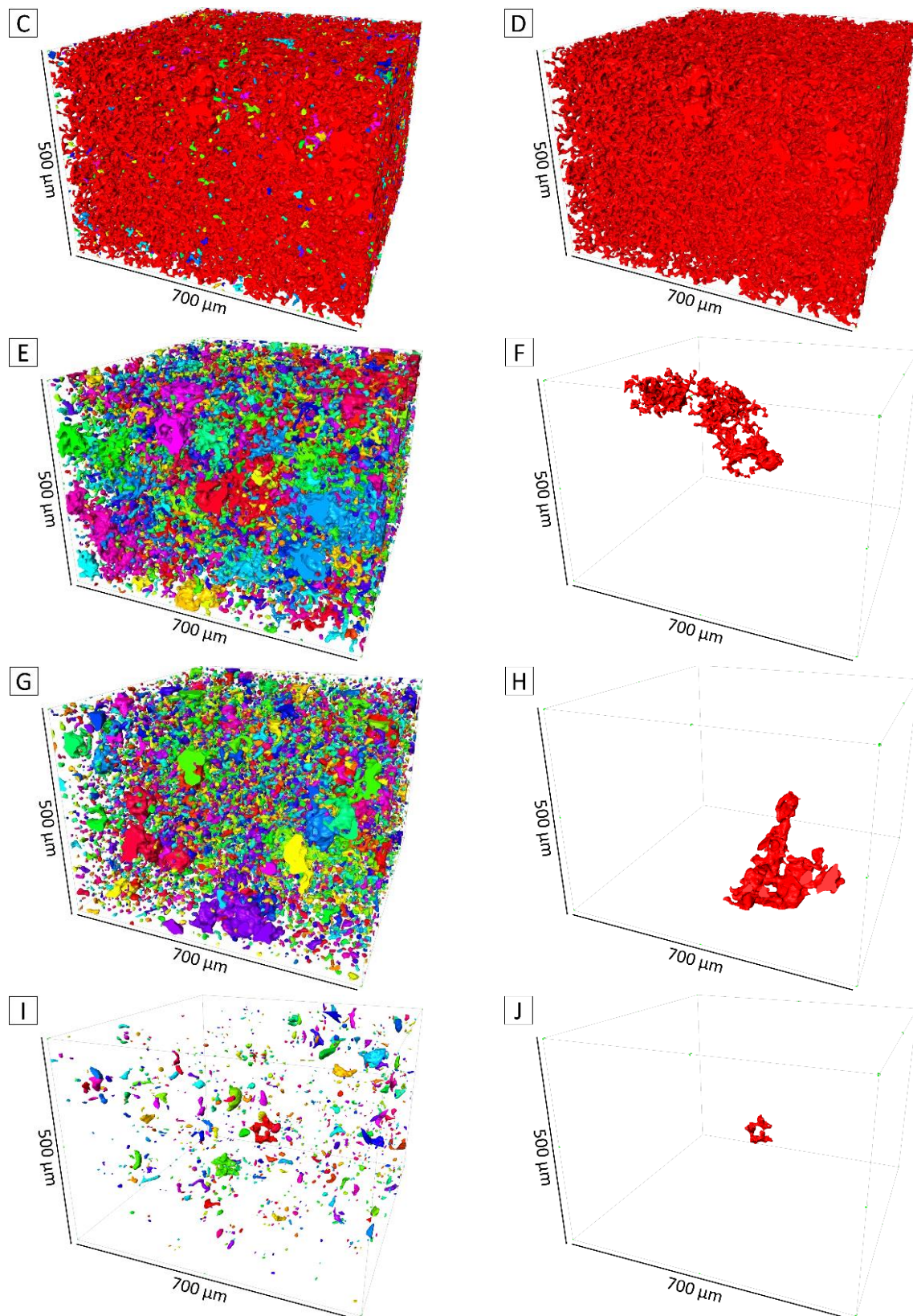
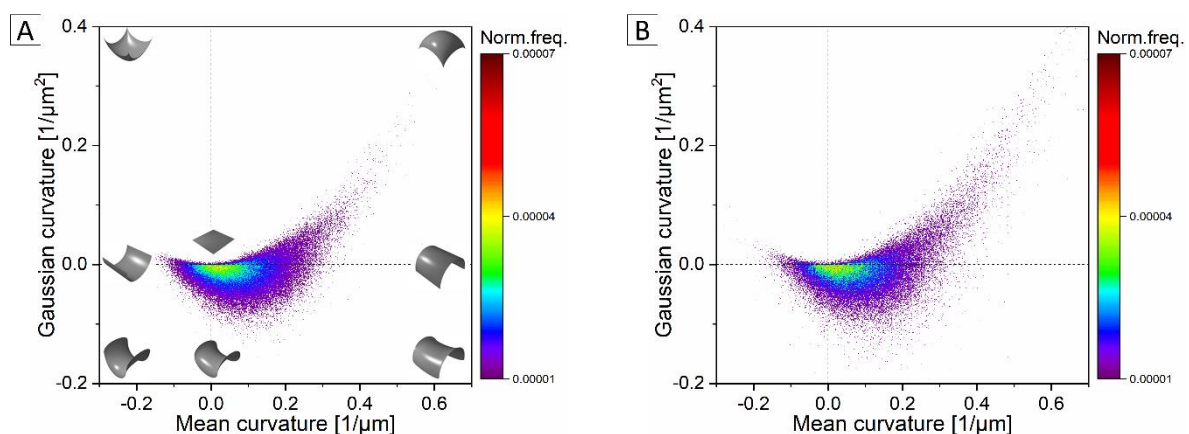


Figure 5-7: Rendered 3D images of pores after image segmentation from similar μ CT volumes in Mg-0.6Ca (Mg/Mg-10Ca) specimens with (A) 21%, (C) 18%, (E) 12%, (G) 8% and (I) 3% porosity values. (B), (D), (F), (H) and (J) represent the 3D images of the largest pore detected in these specimens corresponding to the aforementioned porosity levels.

Visual representation of the formed pores is shown in Figure 5-7; left column. The largest pore volumes corresponding to these specimens are isolated and shown in Figure 5-7; right column. It should be noted that the different coloration for the pores shown in Figure 5-7 left column indicates different volumes they possess and in Figure 5-7 right column the red color is arbitrarily chosen for the representation of the large pore. Evidently, the high pore interconnectivity in specimens with 21% and 18% can be now visualized in Figure 5-7 A to B and C to D, respectively. In Figure 5-7 A and C, pores possessing small volumes, though insignificant in number, can also be seen. In Figure 5-7 B and D, the interconnected pore extends across the specimen to all surfaces which is not the case in specimens with porosities $\leq 12\%$, as visible in Figure 5-7 F, H and J. The convoluted and irregular shapes of the pore volumes is also now apparent from these 3D images in Figure 5-7 E, G and I, which otherwise would have only been a speculation from 2D cross sectional images.

Pore surface curvatures and pore size distribution

The contour plots of the combined mean and Gaussian curvatures of all segmented pore volumes (shown in Figure 5-8; left column) and of the respective largest pore volume (shown in Figure 5-8; right column) correspond to Mg-0.6Ca specimens with porosities 21%, 18%, 12%, 8% and 3%. In general, it is observed that the formed pores after sintering tend to obtain a spherical morphology, irrespective of the sintering temperature. This is evident by the distribution slanting towards the positive-positive (mean-Gaussian curvature) in Figure 5-8; left column, where the curvature distribution for all segmented pores is shown. High pore frequencies in positive-negative (mean-Gaussian curvature) are also found indicating convex cylindrical type pore surfaces. Furthermore, with decreasing specimen porosity less pore shape frequency in the positive-negative and negative-negative (mean-Gaussian curvature) is witnessed indicating less pore surfaces with saddle type and pit type morphologies. Simultaneously, an increased tendency to form spherical pores is witnessed with decreasing specimen porosity (Figure 5-8; left column, A through I).



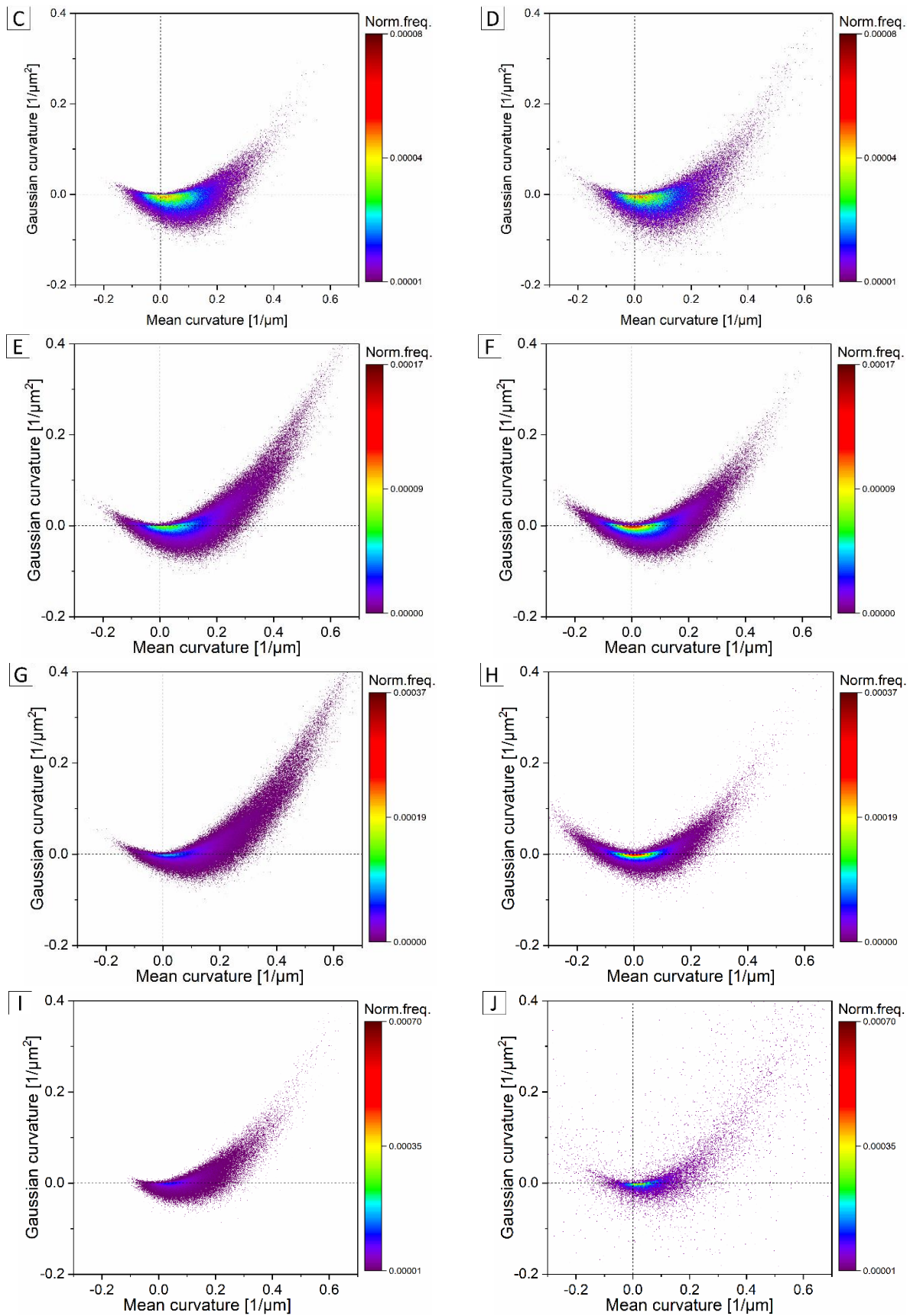


Figure 5-8: Combined mean and Gaussian curvatures of pores after segmentation of similar μ CT volumes in Mg-0.6Ca (Mg/Mg-10Ca) specimens with (A) 21%, (C) 18%, (E) 12%, (G) 8% and (I) 3% porosity values. (B), (D), (F), (H) and (J) represent curvature distributions of the largest pore

detected in these specimens corresponding to the aforementioned porosity levels. The shape descriptors corresponding to the signs of mean and Gaussian curvatures are shown in (A).

From Figure 5-8 F, in specimens with 12% porosity, the curvature distribution of the largest pore volume shows a slight shift from positive-positive (mean-Gaussian curvature) to the negative-positive (mean-Gaussian curvature) compared to the curvature distribution of all pores as in Figure 5-8 E. This shift implies that the largest pore surface may possess a pronounced pit type and concave saddle type morphologies unlike the spheroidal and concave cylindrical morphologies observed for all segmented pores shown in Figure 5-8 E. The same observation holds in the curvature distributions of the largest segmented pore compared to all segmented pores in specimens belonging to porosities $\leq 10\%$. Examples are shown for 8% and 3% specimen porosities in Figure 5-8 G to H and Figure 5-8 I to J, respectively, where the dominant spherical shape effect of all pores surfaces is visible whilst the largest pore surface deviates into a convoluted shape. This behavior, however, is not seen in specimens with 21% and 18% porosities. In these specimens, the largest pore volume alone dominates the total investigated pore volume as indicated in Figure 5-7 B and D. Hence, the curvature distribution of all segmented pore volumes and of the respective largest pore volume remains fairly the same in these specimens.

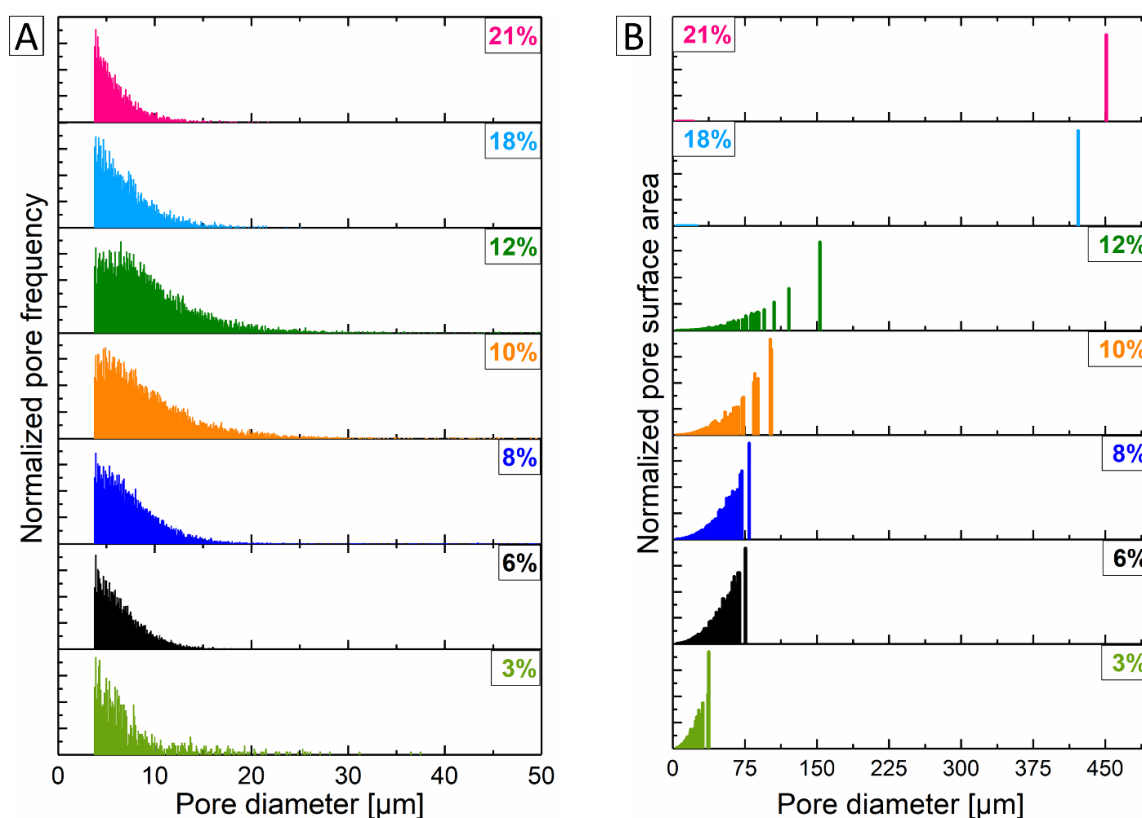


Figure 5-9: (A) Normalized pore frequency as a function of pore diameter for porous Mg-0.6Ca (Mg/Mg-10Ca) specimens with cut off in pore diameter at 50 μm . (B) Normalized pore surface area of all segmented pores in porous Mg-0.6Ca (Mg/Mg-10Ca) specimens vs the actual pore diameters formed in these specimens.

The pore size distribution shown in Figure 5-9 A reveals that in all porous Mg-0.6Ca specimens, except for specimens with 10% and 12% porosities, the distribution tails off at pore diameters nearing 15 μm . This indicates that majority of the formed pores possess smaller diameters in these porosity levels. For the specimens in the pore transition region of open to closed nature i.e., in specimens with 10% and 12% porosities, the distribution tails off at pore diameters nearing 25 μm . Larger pore diameters do exist but due to the choice of showing absolute pore diameter values in Figure 5-9 A, the graph obtained a left skewed nature and therefore the diameter was cut off at 50 μm for better readability. The diameters less than 3.7 μm are omitted due to the threshold pore volume chosen for μCT pore characterization as mentioned in section 4.5.

In Figure 5-9 B, however, the normalized pore surface area of pore diameters pertaining to all segmented pores are shown. Here it can be seen that the equivalent pore diameter relating to the largest pore (Figure 5-7 B and D for specimens with porosities 21% and 18%, respectively) is as high as 400 - 450 μm . For these porosity levels, the smaller diameter pores are virtually not visible in the graph owing to their very small surface area. It is also evident that the equivalent largest pore diameter decreases with decreasing overall Mg-0.6Ca specimen porosity and reaches to the value less than 50 μm in specimens with 3% porosity. Figure 5-9 B also shows that specimens with 10% and 12% porosities do exhibit pores with diameters greater than 100 μm though less significant in number.

5.5 Heterogeneous grain structures in Mg-0.6Ca (Mg_{sieved}/Mg-10Ca)

The sintered microstructures of Mg-0.6Ca (Mg/Mg-10Ca) and Mg-0.6Ca (Mg_{sieved}/Mg-10Ca) specimens (see section 4.1.2 for specimen descriptions) are shown as EBSD maps in Figure 5-10 A and C, respectively. The images clearly indicate a significant difference in grain structures between the two varied process routes. Note that the scale bars of these images are different. In Figure 5-10, different colored regions represent a grain with certain orientation characteristics that are different from the neighboring grains and the pores exhibit a mixed coloration. In Figure 5-10 A, for Mg-0.6Ca (Mg/Mg-10Ca) specimens, a homogeneous grain structure is observed with occasional large grains in the matrix that are insignificant in number. For recap, these Mg-0.6Ca specimens are produced using the as received pure magnesium powder mixed with Mg-10Ca master alloy powder (see section 4.1.2). However, in Figure 5-10 C, heterogeneously coarsened grains are visible in the matrix of Mg-0.6Ca (Mg_{sieved}/Mg-10Ca) specimens despite subjecting both specimen types to the same sintering path as shown in Figure 4-5 (sintering at 627 °C for 63 h duration; light green line). These Mg-0.6Ca specimens are produced using the sieved pure magnesium powder mixed with Mg-10Ca master alloy powder (see section 4.1.2). In general, the grain morphology is irregular with no distinctly faceted or angular grain boundaries. As a side note, the Mg-0.6Ca (Mg/Mg-10Ca) specimens used for EBSD mapping in Figure 5-10 A are essentially similar to those specimens shown in optical image Figure 5-3 G and electron microscopy images Figure 5-4 D and Figure 5-6 D because of the exact same process conditions. It should also be noted that specimens in Figure 5-10 A and C had average

density values of 1.72 g/cm^3 and 1.69 g/cm^3 , respectively, with heterogeneous grain microstructure specimens showing slightly lower density compared to homogeneous grain microstructure specimens when measured using Archimedes technique (see section 4.2).

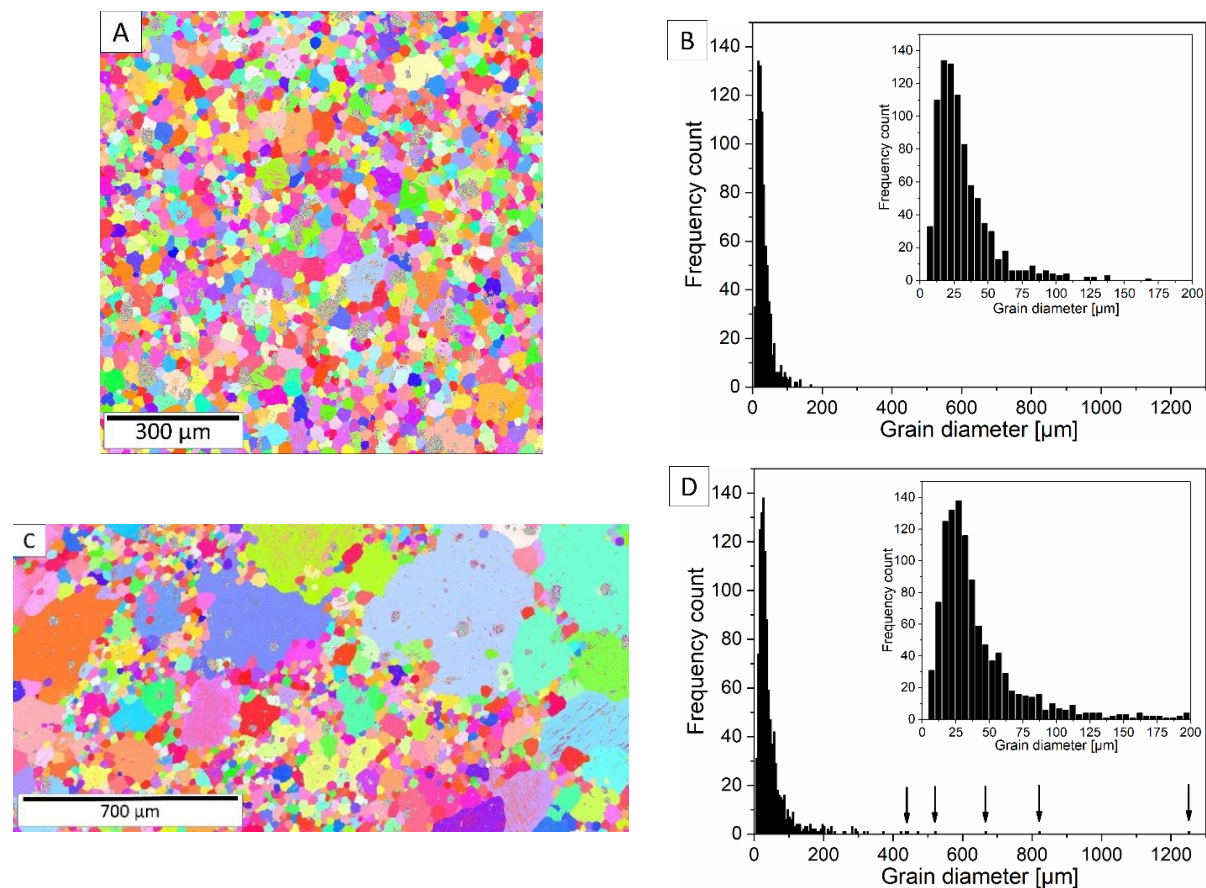


Figure 5-10: EBSD maps and grain size distribution of Mg-0.6Ca specimens produced using (A, B) (Mg/Mg-10Ca) powder mix and (C, D) ($\text{Mg}_{\text{sieved}}$ /Mg-10Ca) powder mix. Arrows in (D) indicate the grain sizes of the heterogeneously coarsened grains in (C).

Figure 5-10 B and D shows the differences in grain size distributions of Mg-0.6Ca (Mg/Mg-10Ca) and Mg-0.6Ca ($\text{Mg}_{\text{sieved}}$ /Mg-10Ca) specimens. As indicated by the arrows in Figure 5-10 D, the heterogeneous grain growth resulted in grain sizes exceeding grain diameters of 1.2 mm, whereas in Mg-0.6Ca (Mg/Mg-10Ca) specimens the maximum grain diameters are found to be around $175 \mu\text{m}$ as shown in the inset of Figure 5-10 B. In addition, the number of grains possessing diameters greater than $100 \mu\text{m}$ have also increased with heterogeneous grain growth comparing the insets of Figure 5-10 B to D. The overview electron microscopy images of Mg-0.6Ca ($\text{Mg}_{\text{sieved}}$ /Mg-10Ca) specimens prior to etching are shown in Figure 5-11 A to D. The grain contrast difference in the BSE mode shows both coarse and fine grain structures in the polished specimen surfaces as in Figure 5-11 A and B. The microstructure shown in Figure 5-11 C corresponds to the fine grain region in Figure 5-11 B, where smaller grain diameters are evident. In the same sample, a distant region in Figure 5-11 D shows the grain boundary juncture of the coarse grain and

fine grain structure indicating varying microstructure on either side of the boundary. The presence of MgO and Mg₂Ca phases is also shown in the Figure 5-11 D. The location of pores is either within the grains or at the grain boundaries with rather spherical morphology. Some pores have sizes corresponding to the initial Mg-10Ca master alloy powder particles whilst most of the pores formed are small and closed/isolated in nature.

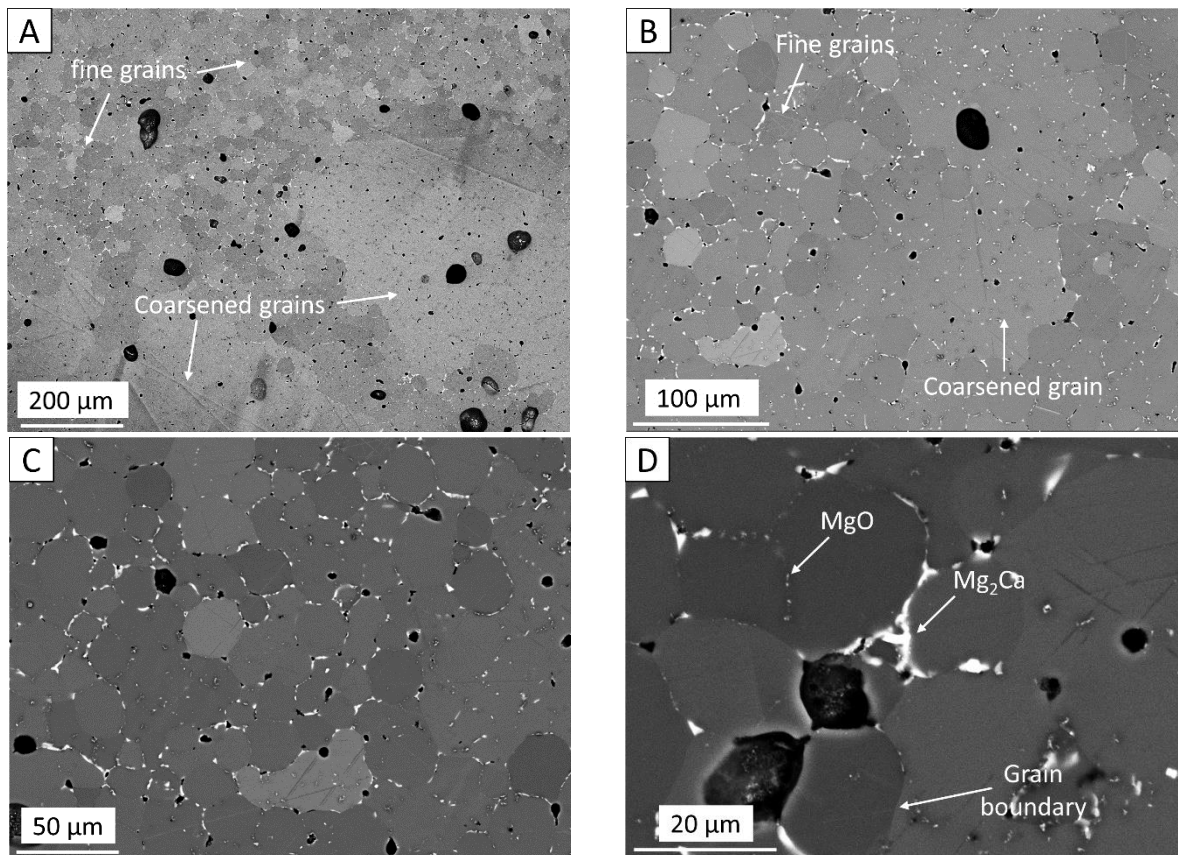


Figure 5-11: (A, B) BSE overview images and (C, D) Close up images of Mg-0.6Ca (Mg_{sieved}/Mg-10Ca) specimens indicating different grain size regions and phases within the same specimen cross section after polishing.

Specific features of the heterogeneous microstructures in Mg-0.6Ca (Mg_{sieved}/Mg-10Ca) specimens are shown in Figure 5-12 A to C. Frequently visible are the oxide particles arranged either randomly or at the locations of former magnesium particle boundaries as shown in Figure 5-12 B. In the sites where a grain is trapped within an enlarged grain, there the existence of Mg₂Ca phase is found along that grain boundary. As shown in Figure 5-4 and Figure 5-6, the grain boundaries of Mg-0.6Ca (Mg/Mg-10Ca) specimens consist mainly of MgO, Mg₂Ca and Mg/Ca/Si rich phases. However, in Mg-0.6Ca (Mg_{sieved}/Mg-10Ca) specimens, eutectic lamellar structures containing α-Mg + Mg₂Ca are evident in addition to the regular Mg₂Ca phase. Primarily, the grain boundaries of the fine grain structure (Figure 5-11 C) tend to possess the regular Mg₂Ca and MgO phases while certain grain boundaries of heterogeneously coarsened grains additionally reveal the eutectic lamellar structures as shown in Figure 5-12 B and C. The presence of MgO phase along the grain boundaries of

coarsened grains is meager. Nevertheless, oxides are evident inside the enlarged grains as in Figure 5-12 B and C. Bright Mg/Ca/Si rich intermetallic phases, sometimes adjoining the eutectic phase and sometimes randomly in the matrix are also visible. The size of the Mg/Ca/Si phase is random but qualitatively larger than those seen in microstructures of Mg-0.6Ca (Mg/Mg-10Ca) specimens. The Mg/Ca/Si rich phases possess a near atomic ratio of 1:1:1 as determined by EDX analysis.

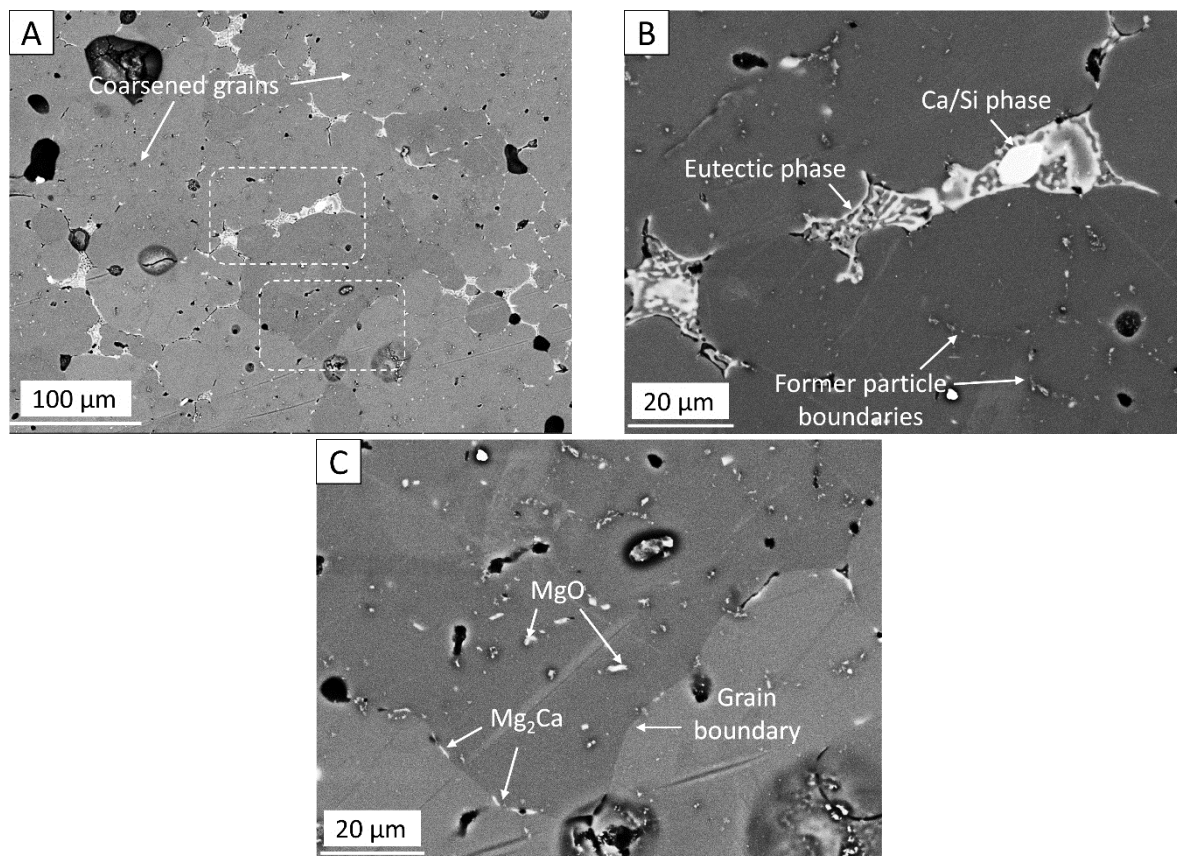


Figure 5-12: Microstructural features of Mg-0.6Ca (Mg_{sieved}/Mg-10Ca) specimens. (A) Overview image. (B, C) are inset pictures of (A) showing eutectic lamellar structures at certain boundaries of heterogeneously coarsened grains and the presence of Mg/Ca/Si and MgO phases, respectively.

EDX analysis at juncture of two heterogeneously coarsened grains in Mg-0.6Ca (Mg_{sieved}/Mg-10Ca) specimens is shown in Figure 5-13. Presence of eutectic lamellar structure α -Mg + Mg₂Ca in combination with Mg/Ca/Si rich phase is witnessed. At the Mg/Ca/Si phase, in Figure 5-13 B, exclusively no magnesium or oxygen was detected. This can be because of the Mg content in this Mg/Ca/Si phase being significantly lower than in the adjacent magnesium rich matrix and therefore it can be undermined in the elemental maps of Figure 5-13. The same observation holds in Figure 5-14 A and B, where a Mg/Ca/Si phase location is chosen for the analysis. The combined presence of oxygen and silicon in the pores and at some precipitate areas can be attributed to the artefact from the specimen exposure to polishing medium consisting SiO₂ particle suspension. At the chosen EDX map parameters in Figure 5-13 B, detection of MgO particles was not feasible due to the small

size of these oxides. However, in Figure 5-14 B oxide particle arrangement along the former magnesium particle boundary can be seen (shown also in Figure 5-12 B).

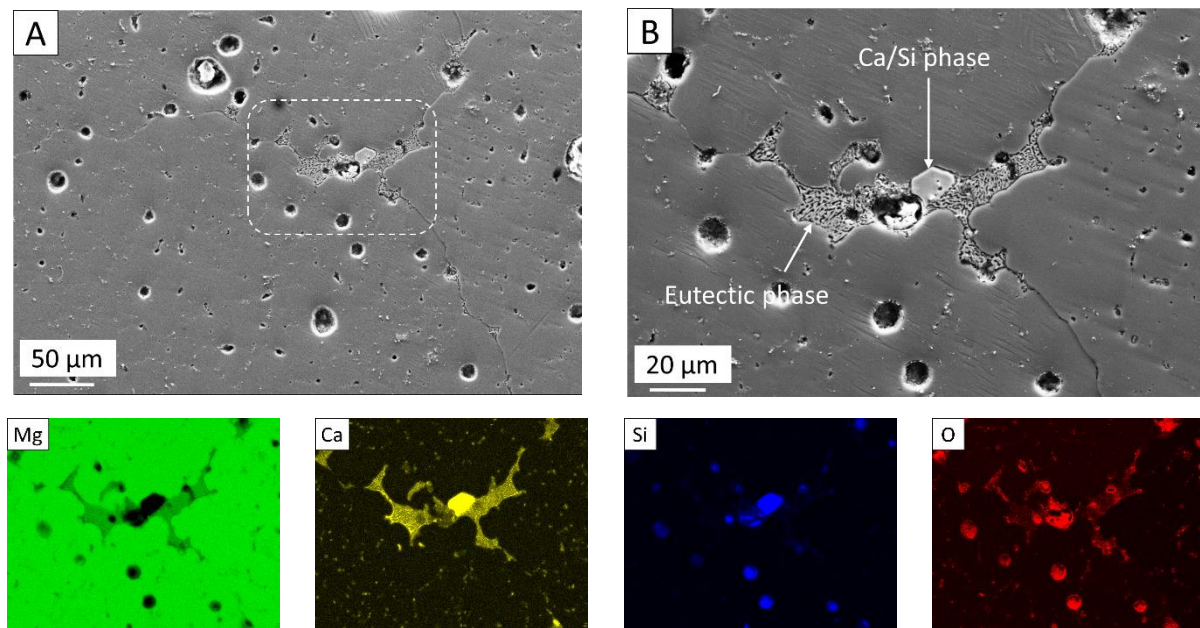


Figure 5-13: EDX map of eutectic lamellar structure in Mg-0.6Ca ($Mg_{sieved}/Mg-10Ca$) specimens. (A) Overview image. (B) Inset of figure (A) showing the eutectic lamellar α -Mg + Mg_2Ca along with Mg/Ca/Si phase. EDX maps of (B) are shown in the second row.

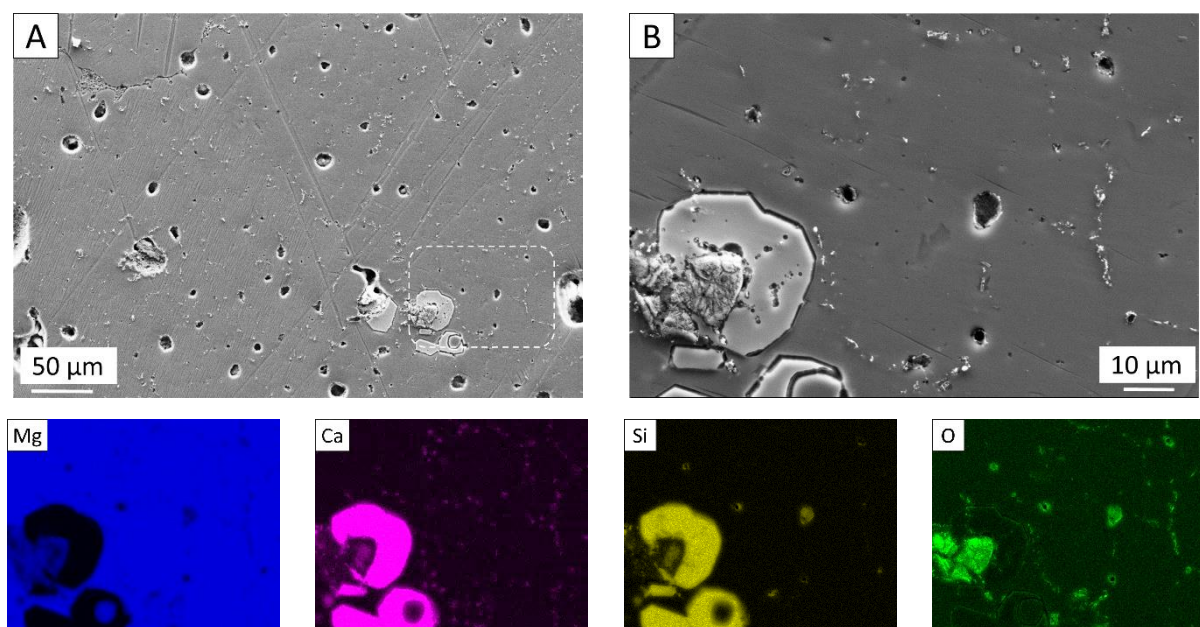


Figure 5-14: EDX map at the site of Mg/Ca/Si phase along with a former particle boundary in heterogeneous grain structure of Mg-0.6Ca ($Mg_{sieved}/Mg-10Ca$) specimens. (A) Overview image and (B) is the inset of figure (A). EDX maps are shown in the second row.

It is to be noted that the heterogeneous grain growth was also observed in Mg-0.6Ca (Mg_{sieved}/Mg-10Ca) specimens, irrespective to the atmosphere (either argon or air) during the initial powder handling and green specimen compaction. In a separate experiment, Mg-0.6Ca (Mg_{sieved}/Mg-10Ca) powder mix was exposed to ambient air for 24 h and specimens were compacted from this powder mix under normal atmospheric conditions. These specimens still exhibited a heterogeneous grain growth after sintering with microstructural features similar to Figure 5-11 through Figure 5-14. This indicates an irreversible change in the surface characteristics of pure magnesium powders after mechanical sieving treatment (section 4.1.3).

5.6 Factors potentially affecting heterogeneous grain growth

5.6.1 Pure Mg powder surface morphology

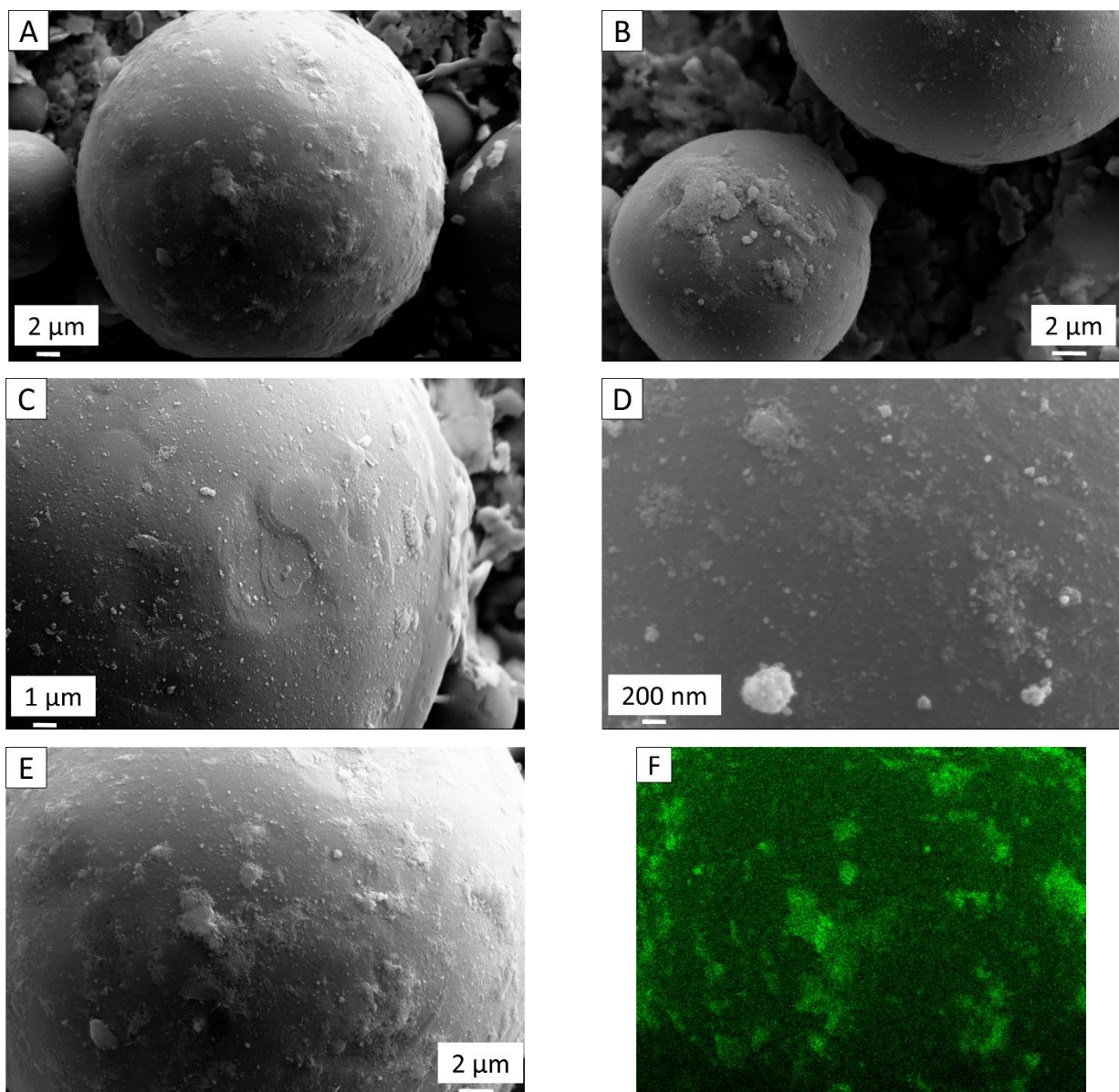
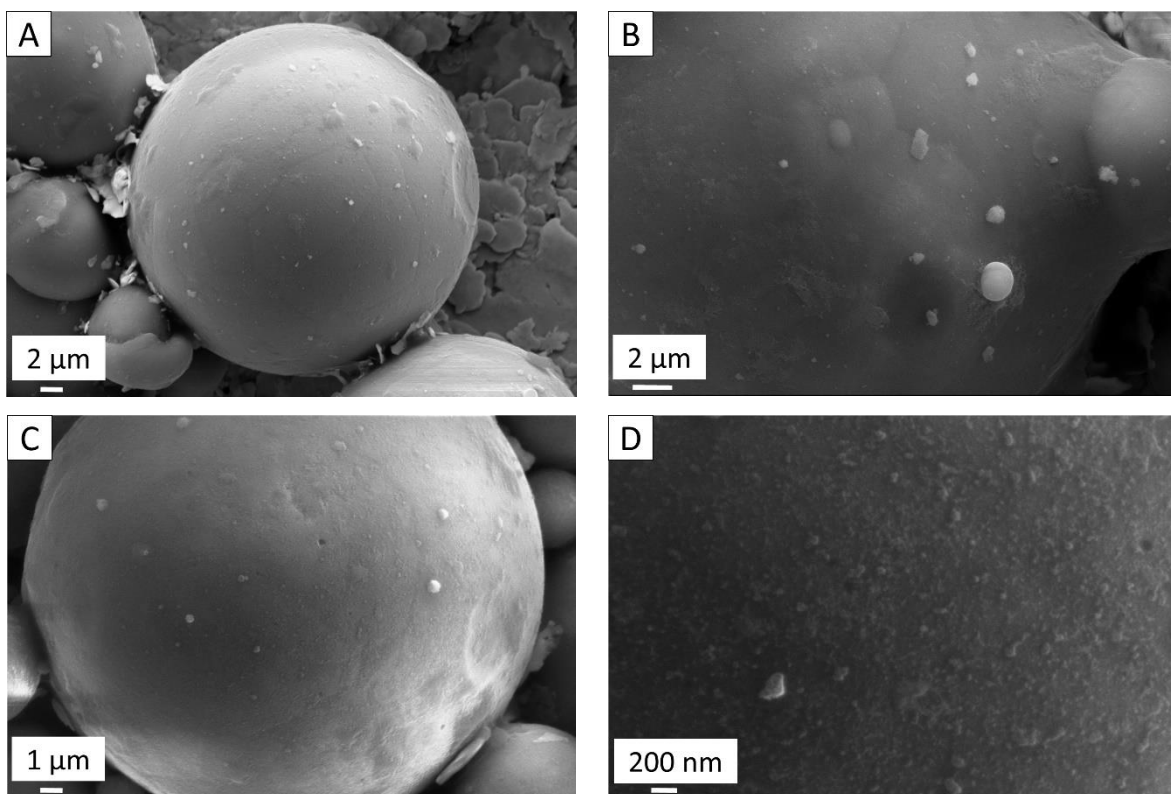


Figure 5-15: Surface morphologies of gas atomized pure magnesium powders used in the study. (A-E) Secondary electron images indicating particulate and patch form of oxide surface. (F) Corresponding oxygen map for image (E) by EDX analysis.

Pure magnesium particles in their as received condition exhibit spherical morphology with occasional fine aggregates as shown in Figure 4-1. However, a close inspection onto certain powder surfaces reveals irregularities which include oxides and surface roughness. Oxides are found to prevail either in a patch form or in particulate form. This can be seen in Figure 5-15 A and B, where irregular patches of oxidized areas are visible and in Figure 5-15 C and D, where particulate type oxides or dispersoids are visible. The corresponding secondary electron image and EDX maps proving oxide presence at these features are shown in Figure 5-15 E and F, respectively. Figure 5-15 D shows that these particles or inclusions can be smaller than 200 nm. These features are abundant on all investigated surfaces of pure magnesium powders. Due to limitation in the detection technique by EDX, where the dominant magnesium and/or oxide peaks supersede the other less apparent elements on the surface, no carbon, silicon or other impurity elements could be detected, irrespective to feature size. An attempt was also made to investigate the oxide type and thickness by preparing the cross section of the powders through conventional polishing technique at very slow speeds. However, the carbon black resin used for embedding powder samples resulted in shrinkage artefacts after solidification of the polymeric resin by creating a gap between polished magnesium powder and the resin. This caused the oxide layer to hugely disrupt and the analysis outcome was not profound.



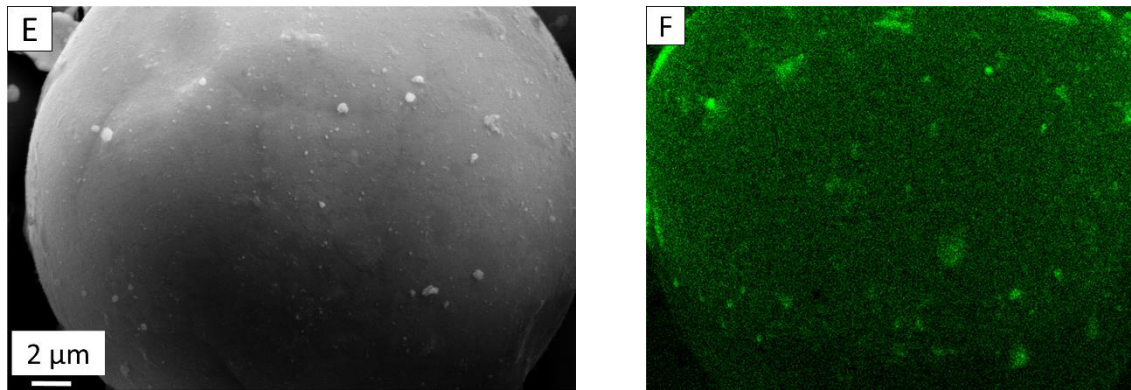


Figure 5-16: Secondary electron images of pure magnesium powders after mechanical sieving treatment used in the study. (A-E) Powder surface view indicating particulate oxide form. (F) Corresponding oxygen map of image (E) by EDX analysis.

The sieving treatment for pure magnesium powders was carried out for 20 min, as mentioned in section 4.1.3. However, no significant differences could be discernible on powder surfaces after 20 min treatment. Therefore, in order to visually observe the changes in the surface after sieving, the sieving time was prolonged for an hour and the powder surfaces thereafter are observed under an electron microscopy. These images are shown in Figure 5-16. In general, pure magnesium powder surfaces after sieving treatment visually appear cleaner of oxides. For the sake of easy comparison, images in Figure 5-16 are chosen with similar magnification respective of the images in Figure 5-15. The powder surfaces of sieved pure magnesium possess particle type oxides with a reduction in the patch type oxide surfaces. The presence of oxides, nevertheless, is still evident as shown in the secondary electron image and EDX mapping of oxide in Figure 5-16 E and F, respectively. Surface deformations exist both before and after sieving treatments and hence difficult to discern if powder roughness has changed due to sieving treatment. It should also be noted that not all particles are free of the patch type oxide features after the sieving treatment. Some pure magnesium powder particles still retain these features after sieving treatment indicating a mix of powder fractions which are in part surface modified by sieving and those which remain unaltered during sieving treatment. The chemical analysis of pure magnesium powder surfaces in the as received and sieved conditions is shown in Table 3.

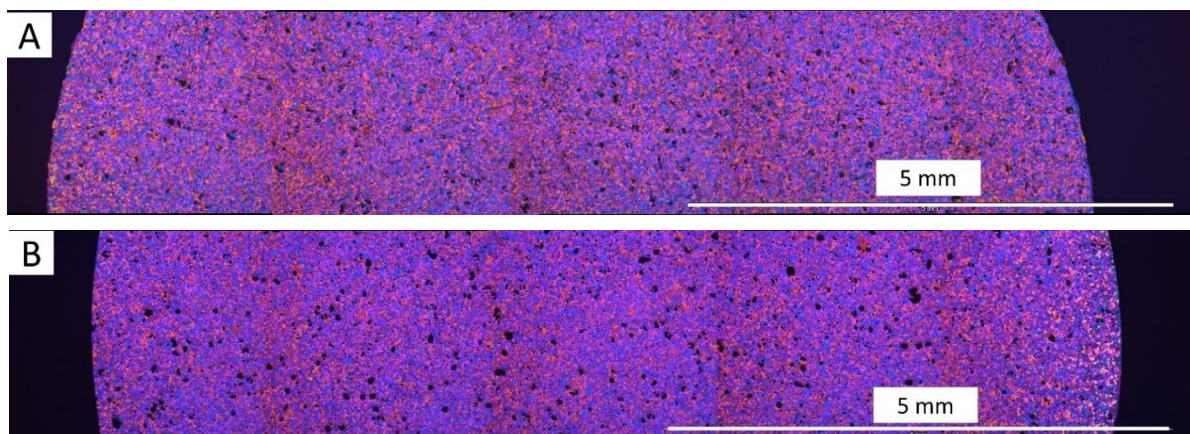
5.6.2 Sintering time

The sintering time for the onset of heterogeneous grain growth and thereby the attained sinter density values of Mg-0.6Ca ($Mg_{\text{sieved}}/Mg-10Ca$) specimens are shown in Table 6. It is evident that the sinter density values measured using Archimedes technique remain nearly constant irrespective of the specimen grain structure. Additionally, all these values are slightly lower than Mg-0.6Ca (Mg/Mg-10Ca) specimens with 1.72 g/cm^3 (after 63 h sintering) processed with same sintering parameters as mentioned in Figure 4-5 (sintering at $627 \text{ }^\circ\text{C}$, light green line).

Table 6: Sintering time for onset of heterogenous grain growth in porous Mg-0.6Ca (Mg_{sieved}/Mg-10Ca) specimens when sintered at 627 °C under argon atmosphere.

Time of sintering, h	(Mg _{sieved} /Mg-10Ca) mix	Density, g/cm ³	
		Before sintering, Geometrical density	After sintering, Archimedes density
3	No grain coarsening	1.33	1.69
6	No grain coarsening	1.35	1.68
12	No grain coarsening	1.35	1.68
18	coarsening observed	1.35	1.70
24	coarsening observed	1.34	1.70
63	coarsening observed	1.35	1.69

Figure 5-10 C indicates the occurrence of heterogeneous grain growth behavior in Mg-0.6Ca (Mg_{sieved}/Mg-10Ca) specimens after sintering for 63 h. Table 6 additionally shows that this heterogeneous grain growth behavior is not continuous over 63 h sintering duration but initiates nearly after 18 h sintering. This can be visually seen in the optical images in Figure 5-17 A to C, where Mg-0.6Ca (Mg_{sieved}/Mg-10Ca) specimens sintered for 3 h, 12 h and 18 h are shown. Longer sintering durations of approximately 18 h caused the heterogeneous grain growth initiation in these specimens as Figure 5-17 C. Though the actual grain diameters may vary, visual observations indicate that the heterogeneous grain structure in Figure 5-17 C after 18 h sintering looks similar to Figure 5-10 C, where the samples are sintered for 63 h. The similarities in these microstructures include the mix of both fine grain and coarse grain regions in the polished specimen surfaces as in Figure 5-17 C, D after 18 h sintering and Figure 5-11 A and B after 63 h sintering. Additionally, the eutectic lamellar structures of α -Mg + Mg₂Ca are also found in these specimens sintered for 18 h. These are shown in Figure 5-17 E and F.



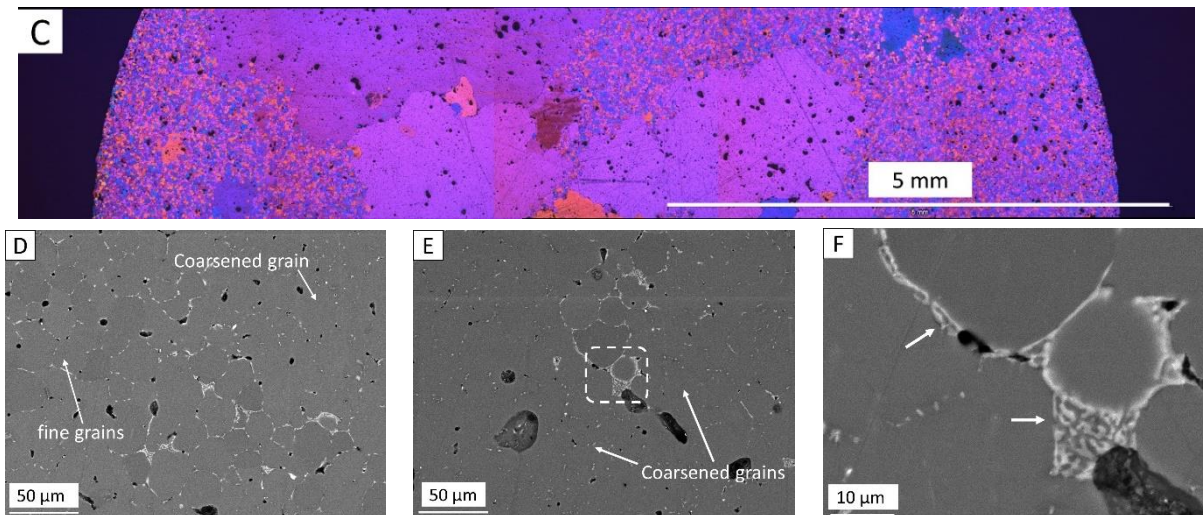


Figure 5-17: Optical microstructures of porous Mg-0.6Ca ($Mg_{\text{sieved}}/Mg-10Ca$) specimens after sintering at 627 °C for different durations of (A) 3 h (B) 12 h and (C) 18 h under argon atmosphere. (D, E, F) BSE images of the specimen shown in image (C). Arrows in (F) show the eutectic lamellar structure of the inset in image (E).

From Figure 5-10 C and the montage of optical images in Figure 5-17 C, a self-similar heterogeneous grain structure is seen to persist from the onset of grain growth at 18 h till 63 h sintering. The vertical stripe appearance in Figure 5-17 A to C is the image artefact arising due to the stitching of five individual images captured side by side.

5.6.3 Master alloy powder particle size

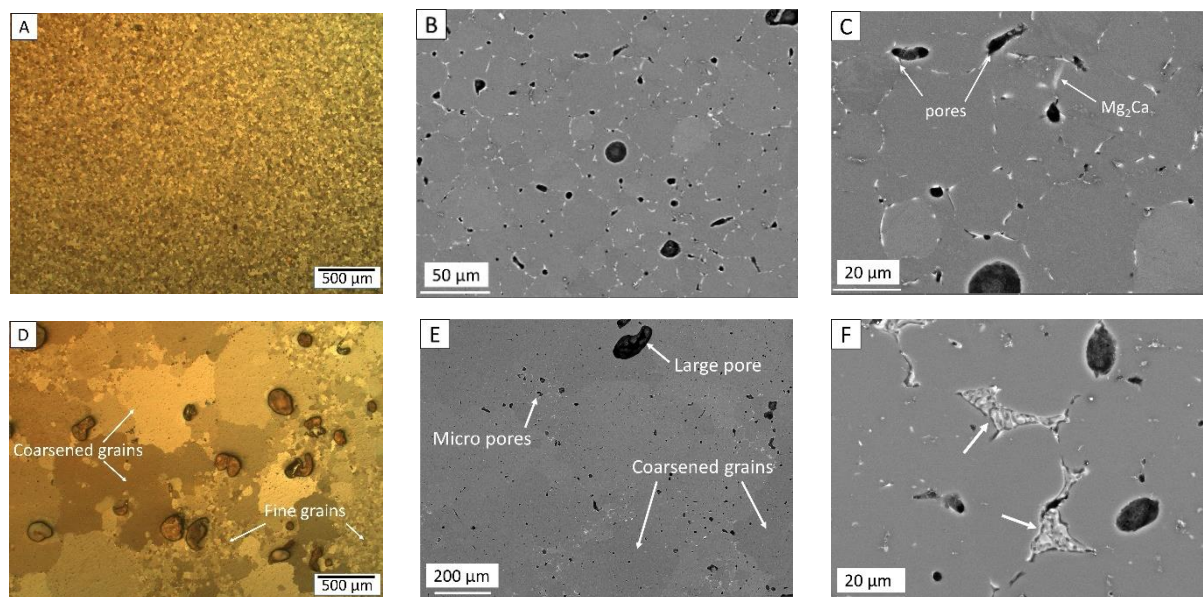


Figure 5-18: Microstructures of Mg-0.6Ca ($Mg_{\text{sieved}}/Mg-10Ca$) specimens with pure magnesium (< 45 μm) blend with Mg-10Ca master alloy powder with varying sizes of (A, B, C) < 32 μm and (D, E, F) 180 – 250 μm. (A, D) Optical microscope images after etching treatment. (B, C, E, F) BSE images prior to etching. Arrows in (F) indicate a eutectic lamellar structure.

Figure 5-18 compares the grain structures of Mg-0.6Ca ($Mg_{sieved}/Mg-10Ca$) specimens fabricated with varying sizes of Mg-10Ca master alloy powder during Mg-0.6Ca powder mixing step. Sintering of the specimens produced from these powder mixes was performed at 627 °C for 24 h, following the grain growth occurrence indication as in Figure 5-17 C. Pure magnesium powder used for powder mixing was in its sieved condition with sizes < 45 μm as in Table 3. Evidently, similar powder size fractions of sieved pure magnesium (< 45 μm) and Mg-10Ca (< 32 μm), as in Figure 5-18 A to C, resulted in no apparent heterogeneous grain growth after 24 h sintering duration. However, when huge size disparity existed in powder fractions of sieved pure magnesium (< 45 μm) and Mg-10Ca (180 - 250 μm) within the same green compact, as in Figure 5-18 D to F, heterogeneous grain growth occurred for the same sintering conditions. In Figure 5-18, the large pores formed are found to be in similar sizes to that of initial master alloy powder particles chosen (i.e., < 32 μm and 180 - 250 μm). It can therefore be expected that the relative sinter densities may vary in these specimens due to the combination of these large sized pores and micron sized pores inherent during sintering. Apart from the formed pore sizes and the sinter densities, the heterogeneous grain growth microstructures visually appear similar between Mg-0.6Ca ($Mg_{sieved}/Mg-10Ca$) specimens in Figure 5-18 D to F and Figure 5-11 A to D, where both fine- and coarse-grained regions in the polished specimens are evident. The eutectic lamellar structure α -Mg + Mg_2Ca is also evident in Figure 5-18 F (pointing white arrows) similar to Figure 5-12 A to C, irrespective to their differences in the chosen master alloy particle sizes and sintering times.

5.7 Semi static immersion test

5.7.1 Effect of porosity on PM Mg-0.6Ca specimen degradation

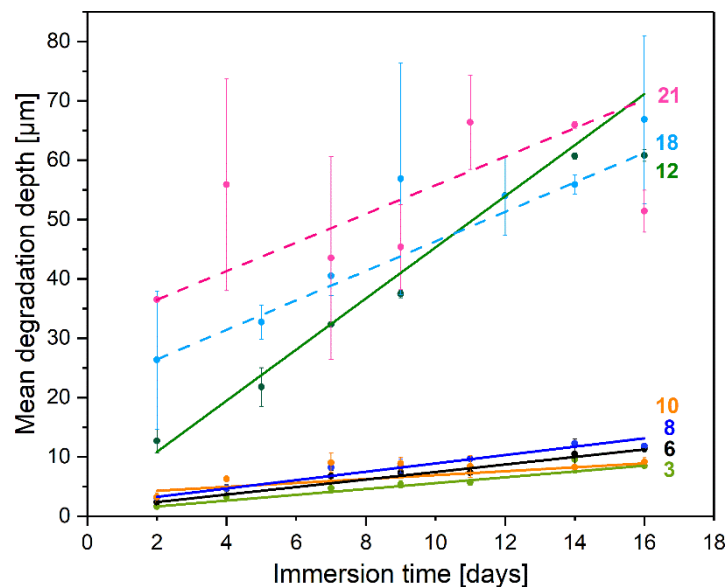


Figure 5-19: Degradation profiles of porous Mg-0.6Ca (Mg/Mg-10Ca) specimens obtained via semi static immersion test. Straight lines indicate linear regression fit for the experimental data. The specimen porosities are correspondingly shown to the right of the graph.

Table 7: Linear regression fit parameters obtained from the degradation profiles of porous Mg-0.6Ca specimens (Mg/Mg-10Ca) specimens.

Sintering temperature [°C]	Total porosity [%]	Parameters of fit			
		Slope [$\mu\text{m}/\text{day}$]	Slope [mm/year]	Intercept [μm]	Fitting coefficient
553	21.1 \pm 2.3	2.41 \pm 0.1	0.88	31.7 \pm 0.4	0.99
567	18.4 \pm 1.5	2.48 \pm 0.2	0.91	21.5 \pm 1.8	0.98
570	12.3 \pm 1.5	4.31 \pm 0.1	1.57	2.2 \pm 1.4	0.99
574	10.2 \pm 2.4	0.33 \pm 0.1	0.12	3.6 \pm 1.2	0.76
582	8.0 \pm 1.1	0.70 \pm 0.1	0.26	1.9 \pm 0.3	0.99
612	5.8 \pm 1.1	0.63 \pm 0.1	0.23	1.1 \pm 0.2	0.99
627	3.4 \pm 1.0	0.49 \pm 0.1	0.18	0.7 \pm 0.1	0.99

From Figure 5-19, it is evident that Mg-0.6Ca (Mg/Mg-10Ca) specimens with porosities $\leq 10\%$ showed low MDD values when compared to specimens with porosities $> 10\%$ during semi static immersion testing for 16 days. This eventually led to the MDR values < 0.3 mm/year in the specimens with $\leq 10\%$ porosities as shown quantitatively in Table 7. Specimens possessing porosities 18% and 21% showed MDR values near to 1 mm/year and the highest values are recorded in specimens with 12% porosity at about 1.6 mm/year. In the present study, high fitting coefficients are indeed observed in the degradation profiles for specimens of all porosity levels except in specimen category with 10% porosity. In these specimens the fitting coefficient drops to 0.76 indicating a slight deviance from linear behavior between degrading specimens. Nevertheless, the initial degradation (y-intercept value) and the overall MDD values remain below 10 μm during the 16 days immersion test with low degradation rate in specimens with 10% porosity (0.12 mm/year). The change in slope of the linear fit, and therefore, the change in MDR value is witnessed between Mg-0.6Ca (Mg/Mg-10Ca) specimens with 10% and 12% porosities. The deviation in mass loss values of the investigated specimens ($n= 2/\text{time point}$) is also found to be varying. This can be seen as small error bars in MDD data points corresponding to specimen porosities $\leq 12\%$ in Figure 5-19. In higher specimen porosities of 18% and 21%, however, the degradation is witnessed by huge scatter in their mass loss error bars (light blue and magenta data points in Figure 5-19) just after 2 days of immersion duration. A great disparity in the initial degradation is shown in Table 7, where the y-intercept value is < 5 μm for specimen porosities $\leq 12\%$ and > 20 μm for higher specimen porosities of 21% and 18%.

Osmolality measurements and mass of the degradation layer

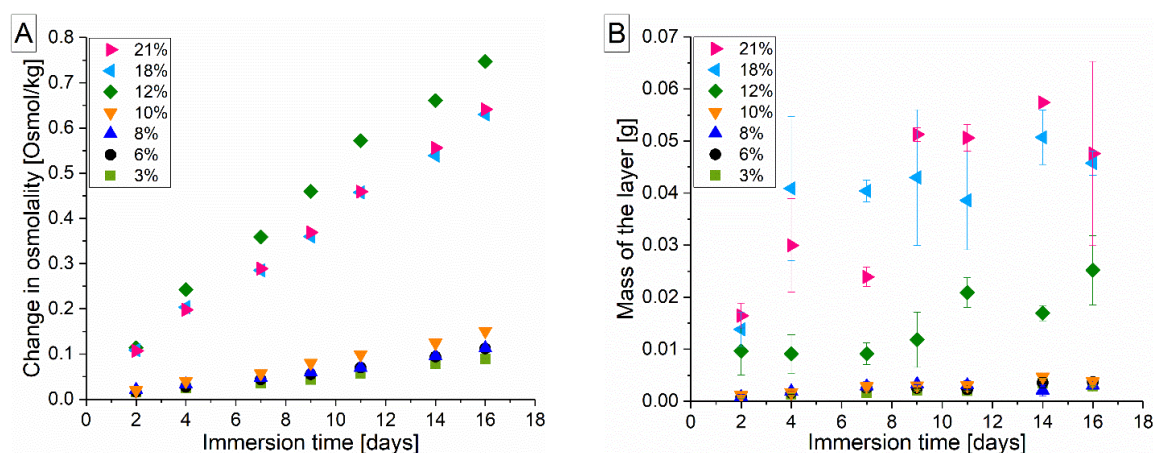


Figure 5-20: (A) Incremental change in the extract osmolality of degrading Mg-0.6Ca (Mg/Mg-10Ca) specimens with varying porosities during semi-static immersion test. (B) Variation in the mass of the formed degradation layer with immersion time.

As mentioned in section 4.6.3, the measurement of pH and osmolality was performed *ex situ*. Measured pH ranged 7.8 - 8.1 for all immersed Mg-0.6Ca (Mg/Mg-10Ca) specimens and 7.5 - 7.9 for the cell culture control units during 16 days immersion testing. In Figure 5-20 A, the cumulative increment in osmolality indicates the progressive degradation that is occurring with immersion time. Evidently, the gradient increase in osmolality values is minor in the degrading specimens with porosities $\leq 10\%$. These results are in agreement with the degradation profiles for these specimens shown in Figure 5-19. Also, the mass of the formed degradation layer, shown in Figure 5-20 B, shows a slight increase but remains fairly low in these specimens with $\leq 10\%$ porosities. However, in Mg-0.6Ca (Mg/Mg-10Ca) specimens with huge interconnected pores, like 18% and 21% porosity categories, the change in osmolality is higher as reflected also by their degradation profiles in Figure 5-19. The mass of the degradation layer formed in these specimens is also the highest among the investigated porous specimens. In addition, highest variation in the scatter of their error bars is witnessed for these specimens (Figure 5-20 B; light blue and pink data points). In Figure 5-21 G to L, the degraded surfaces of specimens with $\leq 10\%$ porosity showed homogeneous dimple-like features with occasional presence of original pores. The sizes of these dimple-like features increased with immersion duration from 2 to 16 days. The dimples turned to deep grooves as the specimen porosity increased to 12% as in Figure 5-21 D to F. These grooves appear still homogeneous upon initial immersion and occasional pits are observed after 16 days immersion in these specimens. At higher porosities of 18% and 21%, the degraded surface is non-homogeneous with cracks and deep grooves penetrating through the material just after 2 days of immersion time, as shown in Figure 5-21 A to C for specimen porosity of 21%. Occasional cracks appeared throughout the specimen surfaces with material wearing away as deep as half the sample thickness at higher immersion times. All the images in Figure 5-21 represent the degraded specimen top surfaces. The degraded

bottom surfaces showed pitting effect even in low porosity specimens. These pits are observed to form adjacent to non-corroded metallic surfaces indicating the possibility of localized attack in these regions. Though the degradation profiles shown for porous Mg-0.6Ca (Mg/Mg-10Ca) specimens in Figure 5-19 and Table 7 include this additional mass loss due to pitting at bottom surfaces, it is generally considered to be an artefact arising from the nature of immersion test procedure rather than the actual material degrading property.

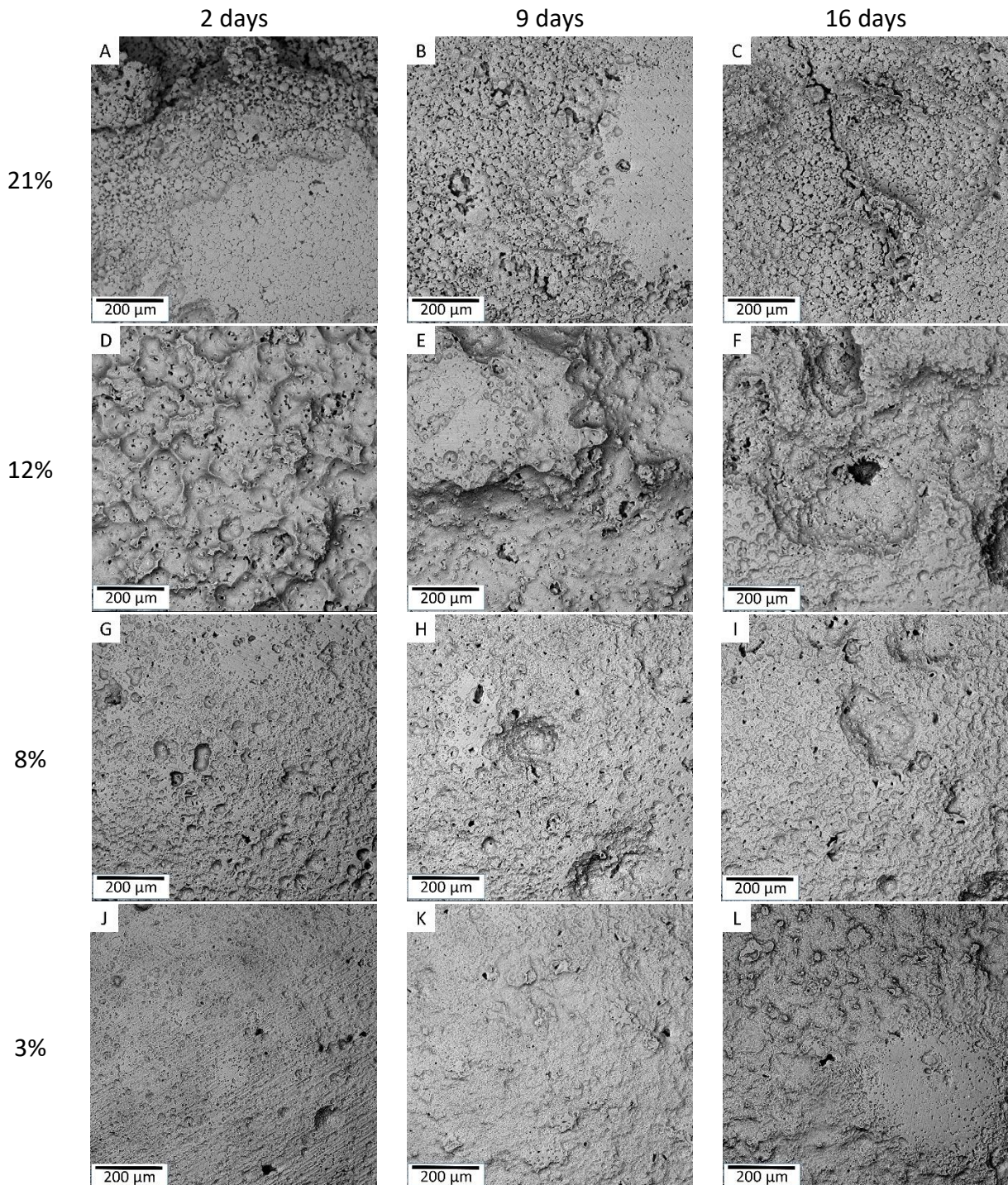


Figure 5-21: Degraded surface morphologies of Mg-0.6Ca (Mg/Mg-10Ca) specimens with varying porosities after chromic acid treatment at different immersion durations.

5.7.2 Effect of heterogeneous grain structure on Mg-0.6Ca specimen degradation

Immersion test results for porous Mg-0.6Ca ($Mg_{\text{sieved}}/Mg-10Ca$) specimens possessing heterogeneous grain structures are shown in Figure 5-22; violet line. These specimens belong to the sintering path shown in Figure 4-5 (sintering at 627 °C for 63 h duration; light green line) and possess the microstructure shown in Figure 5-10 C and grain size distribution in Figure 5-10 D. For comparison, the degradation profiles of Mg-0.6Ca ($Mg/Mg-10Ca$) specimens possessing homogeneous grain structure ($\sim 30 \mu\text{m}$ grain sizes) are also shown in Figure 5-22. These specimens are chosen for comparison because of the same sintering conditions shown in Figure 4-5 (sintering at 627 °C for 63 h duration; light green line). They possess the microstructure shown in Figure 5-10 A.

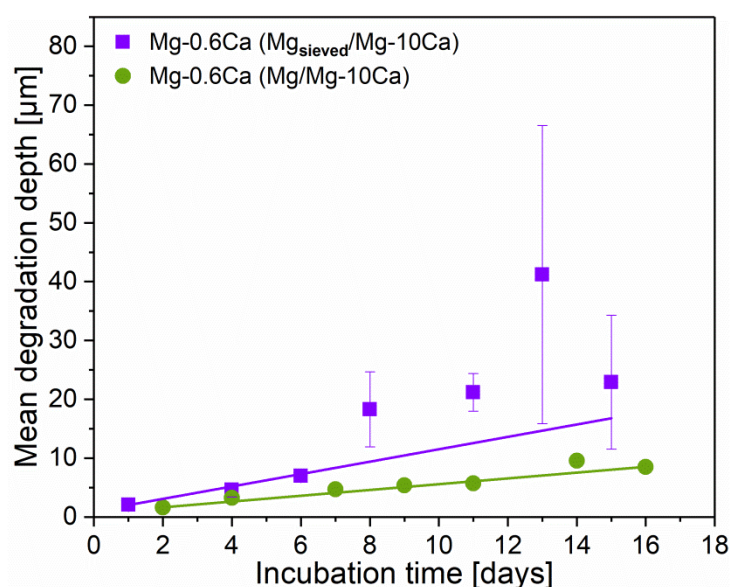


Figure 5-22: Degradation profiles of Mg-0.6Ca ($Mg_{\text{sieved}}/Mg-10Ca$) specimens shown in violet obtained after 16-days immersion degradation test. Green line represents Mg-0.6Ca ($Mg/Mg-10Ca$) specimens with 3% porosity shown for comparison.

Table 8: Linear regression fit parameters obtained from the degradation profiles of Mg-0.6Ca ($Mg_{\text{sieved}}/Mg-10Ca$) specimens compared to Mg-0.6Ca ($Mg/Mg-10Ca$) specimens.

Specimen processing	Parameters of fit			
	Slope [$\mu\text{m}/\text{day}$]	Slope [mm/year]	Intercept [μm]	Fitting coefficient
Mg-0.6Ca ($Mg_{\text{sieved}}/Mg-10Ca$)	1.05 ± 0.1	0.38	0.97 ± 0.3	0.93
Mg-0.6Ca ($Mg/Mg-10Ca$)	0.49 ± 0.1	0.18	0.7 ± 0.1	0.99

In general, slightly higher MDD values are recorded in specimens of Mg-0.6Ca ($Mg_{\text{sieved}}/Mg-10Ca$) compared to Mg-0.6Ca ($Mg/Mg-10Ca$) with progressive immersion time. A substantial increase in the scatter of error bars in MDD values is seen between 8 to 15 days of immersion in Mg-0.6Ca ($Mg_{\text{sieved}}/Mg-10Ca$) specimens. This behavior does not exist

in Mg-0.6Ca (Mg/Mg-10Ca) specimens as shown in Figure 5-22 (green line). Table 8 indicates also a slightly higher degradation rate and weaker linear fit coefficients for the experimental data in the specimens with heterogeneous grain structures compared to their counterparts.

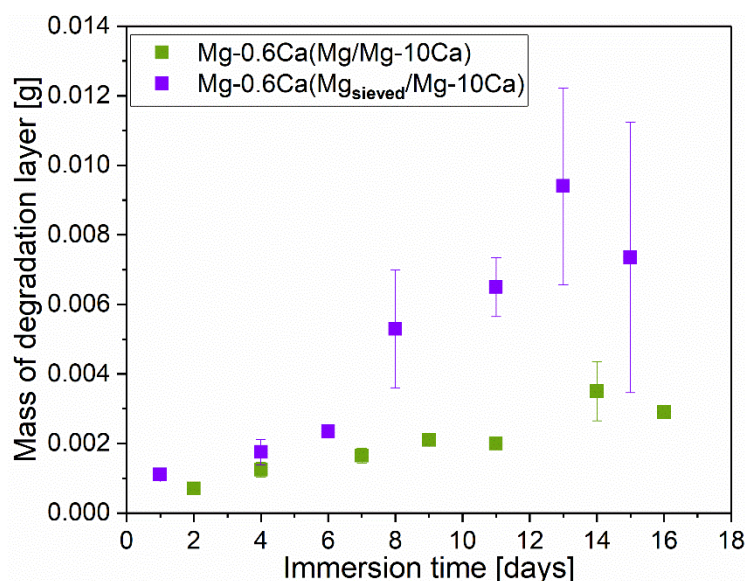


Figure 5-23: Variation in the mass of the formed degradation layer with immersion time of Mg-0.6Ca (Mg_{sieved}/Mg-10Ca) Mg-0.6Ca (Mg/Mg-10Ca) specimens with heterogeneous and homogeneous grain structures, respectively.

A higher mass of the degradation layer formed is observed in Mg-0.6Ca (Mg_{sieved}/Mg-10Ca) specimens with heterogeneous grain structure compared to their homogeneous grain structure counterparts as shown in Figure 5-23. Here again, the variation in the scatter of error bars is noticeably high in specimens of Mg-0.6Ca (Mg_{sieved}/Mg-10Ca) compared to Mg-0.6Ca (Mg/Mg-10Ca) specimens (shown in green in Figure 5-23). The scale of y-axis in Figure 5-23 is at a lower limit compared to that in Figure 5-20 B, indicating that the amount of formed layer in specimens with heterogeneous grain structures is in fact low compared to other non-homogeneously degrading specimens, like the specimens possessing higher porosities of 18% and 21% as in Figure 5-20 B.

5.8 Mechanical properties of PM Mg-0.6Ca

5.8.1 Dependence on Mg-0.6Ca specimen porosity

Table 9 shows an increase in the tensile strength (UTS), elongation to fracture and yield strength with decreasing porosity in Mg-0.6Ca (Mg/Mg-10Ca) specimens. For specimens with porosities 3% and 6%, similar mechanical properties are recorded. On the other hand, no discernible yield strength values could be obtained using similar tensile test parameters for specimens with 21% porosity. The representative tensile curves for porous Mg-0.6Ca (Mg/Mg-10Ca) specimens are shown in Figure 5-24 A. Some specimens possessing 18% and 21% porosity levels prematurely fractured. Certain specimens also exhibited

negative strains at initial loading indicating the possibility of specimen slipping during initial stages of tensile testing.

Table 9: Tensile strength and elongation to fracture values (n= 5) recorded for Mg-0.6Ca (Mg/Mg-10Ca) specimens with varying porosities in their sintered condition prior to immersion degradation test.

Sintering temperature [°C]	Specimen porosity [%]	Tensile properties		
		UTS [MPa]	Elongation [%]	Yield strength [MPa]
553	21.1 ± 2.3	21 ± 4	< 0.2	-
567	18.4 ± 1.5	35 ± 3	0.6 ± 0.2	29 ± 2
570	12.3 ± 1.5	62 ± 7	2.1 ± 0.4	41 ± 3
574	10.2 ± 2.4	70 ± 9	2.0 ± 0.6	53 ± 4
582	8.0 ± 1.1	102 ± 11	3.6 ± 1.2	65 ± 4
612	5.8 ± 1.1	145 ± 3	8.3 ± 1.3	74 ± 3
627	3.4 ± 1.0	145 ± 4	7.2 ± 1.1	71 ± 3

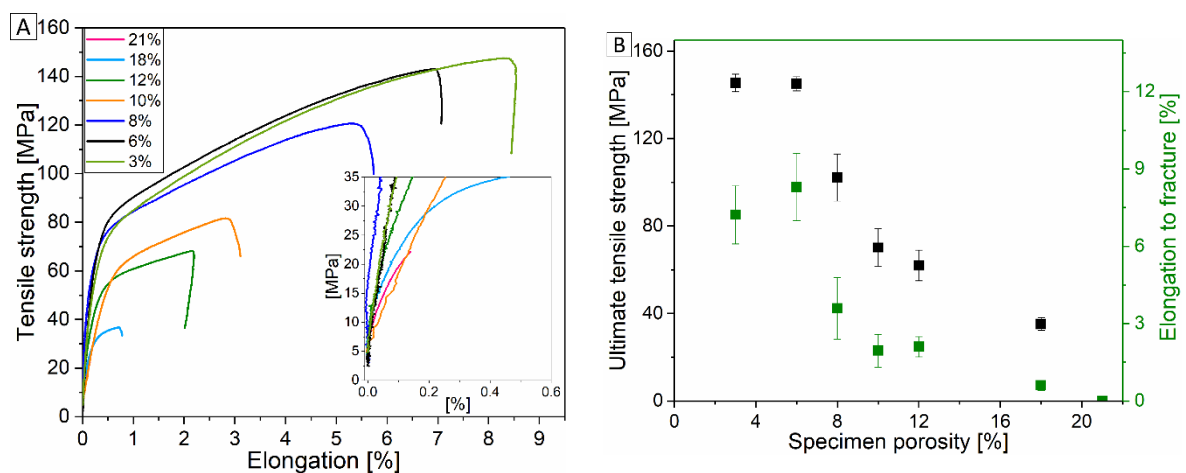


Figure 5-24: (A) Representative tensile curves for Mg-0.6Ca (Mg/Mg-10Ca) with varying porosities. (B) UTS and elongation to fracture values in Mg-0.6Ca (Mg/Mg-10Ca) specimens as a function of porosity.

5.8.2 Dependence on Mg-0.6Ca specimen grain structure

No significant differences are observed in the recorded UTS and elongation to failure values in Mg-0.6Ca (Mg_{sieved} /Mg-10Ca) specimens compared to Mg-0.6Ca (Mg/Mg-10Ca) specimens as shown in Figure 5-25. The only discernible difference is the increased standard deviation in the measured UTS and elongation values for specimens with heterogeneous grain structures compared with homogeneously grain sized specimens.

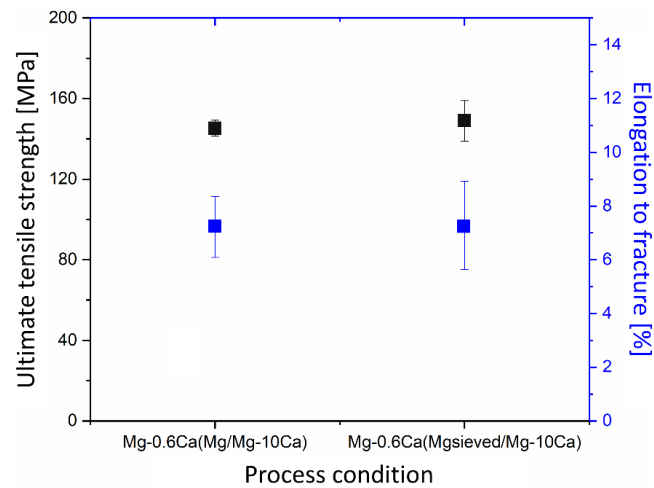


Figure 5-25: Mechanical properties of porous Mg-0.6Ca (Mg_{sieved} /Mg-10Ca) specimens with heterogeneous grain structure compared with Mg-0.6Ca (Mg/Mg-10Ca) specimens with homogeneous grain structure.

6 Discussion

6.1 Effective liquid phase mass fraction for pore closure

In each Mg-0.6Ca specimen, both pure magnesium and master alloy powder particles exist with random distribution in their initial pressed condition, provided the mixing step was successful. According to the Mg-Ca equilibrium phase diagram, as in Figure 2-4, the master alloy powder Mg-10Ca enters complete liquid region after 579 °C [13]. From 516 °C, where master alloy powder enters the two phase α -Mg + liquid region until 579 °C, only a fraction of it melts and contributes to sintering densification. Comparing Figure 5-1 and Figure 2-5, it can be observed that the densification in Mg-0.6Ca (Mg/Mg-10Ca) specimens relates to the mass fraction of liquid formed by melting of Mg-10Ca master alloy powder due to the increased sintering temperature. It was ascertained via a differential thermal analysis that calcium diffuses rapidly from the formed liquid to the surrounding magnesium base material when the liquid forming master alloy is held above eutectic temperatures even for a few minutes [6]. This diffusion leads to a decrease in the calcium content of the liquid phase from 10 wt.% calcium towards the equilibrium 0.6 wt.% calcium in magnesium following the compositional changes along the liquidus and solidus lines of the Mg-Ca equilibrium phase diagram as in Figure 2-5. As persistent liquid phase sintering conditions prevail at all the sintering temperatures chosen in the present work, the remaining melt solidifies leading to the formation of intermetallic phase like Mg_2Ca . The oxidation resistance of magnesium is reported to be improved by the presence of calcium up to 645 °C [169]. Calcium is also reported to reduce the surface oxide of magnesium along with other surface constituents [8, 9]. These two effects combined indicate the availability of metallic powder magnesium surfaces for enhanced sinter densification with simultaneous protection from further oxygen attack due to calcium presence. Since, sintering progresses through diffusion which in turn strongly depends on temperature, it can be expected that the nature of porosity changes from open to closed with increasing sintering temperature [170]. It is reported for supersolidus liquid phase sintering systems, like nickel base superalloys, that closed porosity forms between 85% and 95% of theoretical density [39, 171]. This, however, may vary in regular liquid phase sintering systems due to the amount of liquid phase and its distribution. In the present work, it is indeed observed that the closed porosity in the Mg-0.6Ca (Mg/Mg-10Ca) specimens starts at the specimen porosity of nearly 12% (Figure 5-2). This occurred at sintering temperature of 570 °C, where approximately 90% mass fraction of the liquid phase contribution occurred via the master alloy melting (Figure 2-5; isothermal line at 570 °C).

The fading protective nature of MgO surface at temperatures greater than 500 °C due to its porous nature at these temperatures is reported leading to both inward and outward diffusion of surrounding gases [172, 173]. Non-protective nature of oxide on molten

magnesium was also reported by Jalilvand et al. during casting conditions [174]. This indicates the possibility of an enhanced solid-state sintering between pure magnesium powder particles, provided oxygen free sintering atmospheres exist. In addition, the compaction pressures during green specimen preparation are known to disrupt the oxide surface in the form of cracks [175]. These combined effects can be seen as the relative density increase in PM pure magnesium reference specimens with increasing sintering temperature (Figure 5-1 B). It is shown microscopically by Burke et.al that the diffusion distance of calcium rich liquid by melting of a large size eutectic Mg-Ca rich particle affected the densification differently at different distances from its melting location [8]. The same is observed in the present study where dense areas are seen at random at lower sintering temperatures of 553 °C and 567 °C due to localized partial master alloy powder melting (ex. white boxes in Figure 5-5 A and B). The smaller diffusion distances can be attributed to the low fraction of localized liquid formed pertaining to that sintering temperature. As more master alloy transforms to liquid, the diffusion distances are expected to increase. With this effect arising at the same time from all master alloy particles at different locations within the compact, it can be expected that the formed liquid has effectively spread within the compact leading to closure of certain pore channels. This can be seen in Figure 5-9 B, where pore channel closure due to an increased overall liquid fraction in the compact has resulted in the transformation of the previously large interconnected pore (at 567 °C sintering temperature) to numerous intermediate pore sizes of 75 - 150 μm diameter (at 570 °C sintering temperature). This can be seen visually also in Figure 5-7 C to E and in Figure 5-9 B. Though the dominant factors for densification may vary with sintering temperature and amount of persistent liquid, it is proposed that the pore closure due to the enhanced diffusion distances of calcium rich liquid and reduction of surface oxide by calcium played an important role for Mg-0.6Ca sinter densification. In order to determine the dominant densification mechanism at respective sintering temperatures, further experiments will be necessary.

Delayed pore filling by the capillary liquid and therefore a delayed pore spheroidization are reported to occur in liquid phase sintering systems due to the presence of insoluble gases trapped inside the pores. These gases may form either due to sintering atmosphere [176, 177] or reaction products at high sintering temperatures [177]. In the present study, pore isolation followed by closed pore formation and spheroidization of the formed small pores (Figure 5-8 E, G, I) is observed in specimens of Mg-0.6Ca (Mg/Mg-10Ca) with porosities 12%. Due to the capillary force that causes pore filling often being relatively weaker than the gas pressure trapped inside the pores, a delayed pore generation and sometimes specimen bloating are peculiar with prolonged sintering times [177]. However, this adverse effect was not observed in the present study (Figure 4-3 B) indicating less hindrance to the sintering activity from the used high purity argon gas during sintering. It can be partly attributed to the fact that heating stage is also performed under vacuum (Figure 4-5; stage II). Another characteristic of liquid phase sintering is the sudden increase in sinter density within a small temperature gradient [178, 179]. The same is the case in PM

Mg-0.6Ca specimens, where the porosity transition from highly open pore nature to 55% closed porosity occurred within a temperature gradient of 4 °C (Figure 5-1).

It should be noted that the liquid phase mass fraction calculations are performed based on a Mg-Ca equilibrium phase diagram. However, in most cases non-equilibrium conditions prevail resulting in different microstructures compared to the ones predicted by the equilibrium phase diagrams. It is also reported that the formation of liquids from gas atomized alloy powders during heating can occur at temperatures lower than the liquidus line prescribed by the equilibrium phase diagrams [180]. This is due to the microstructural changes that occur within alloy powders, like Mg-10Ca in the present study, due to high degree of undercooling during solidification stage of powder production. This microstructural change is reported to be, in turn, powder particle size dependent [181-183]. In addition, the powder surface morphologies change in relation to the presence of impurities that may respond differently to the undercooling of atomized powders [184]. Due to these reasons, the reported 90% liquid phase mass fraction formed due to master alloy melting at 570 °C (Figure 2-5) should only be considered as an approximate quantity. Nevertheless, the present study establishes that in PM Mg-0.6Ca specimens produced by master alloy blending route, for effectively getting rid of the interconnected pores and to initiate the formation of closed pores, the sintering temperatures are to be chosen such that nearly 90% of master alloy liquifies.

6.2 Influence of pore features on PM Mg-0.6Ca degradation

6.2.1 Surface open pore fraction and pore interconnectivity

The degradation results for porous Mg-0.6Ca (Mg/Mg-10Ca) specimens indicate that the degradation rates do not linearly correlate to the specimen porosity. Combined analysis from Figure 5-19 and Table 5 indicates that with decreasing Mg-0.6Ca specimen porosity, the pore interconnectivity decreased leading to a decrease in specimen degradation rates. Additionally, homogeneously degrading surfaces are found in specimens with porosities $\leq 10\%$ in Figure 5-21 G to L. Direct conclusion can be drawn that the pore interconnectivity is the important factor promoting degradation homogeneity and low degradation rates in Mg-0.6Ca (Mg/Mg-10Ca) specimens. The pore interconnectivity of $< 10\%$ is shown to facilitate this behavior until 10% porosity. However, in specimens with high pore connectivity, i.e., specimen porosities of 18% and 21%, the degradation is non-uniform as seen by huge scatter in their mass loss error bars values. Specimens in pore transition region, i.e., 12% porosity exhibited low initial degradation 12 μm and also a later steady state degradation as evident by the 0.99 coefficient of fitting (Table 7).

A noticeable change in the linear degradation behavior can be observed between specimens with 10% and 12% porosities (Figure 5-19). These Mg-0.6Ca specimens in the pore transition regions also showed a similar pore size distribution (Figure 5-9 A and B). In addition, their impurity concentrations (Table 4) and pore shape analysis (Figure 5-8 E and F) showed similar distributions. However, their degradation profiles reveal a significant difference in their mean degradation rates by 1.6 mm/year and 0.2 mm/year for 12% and

10% porosities, respectively. The only influential parameter that can lead to a variation in their degradation rates is their surface open pore fraction as assessed from their μ CT data (Figure 5-2). The closed pore fraction increased as the specimen porosity decreased from 12% to 10%. This means a higher fraction of surface open pores exists, nearly 45% in specimens with 12% porosity, compared to 33% in specimens with 10% porosity. This signifies that the surface open pore fraction should be $< 45\%$ for low degradation rates to persist in porous PM Mg-0.6Ca system, provided the pore interconnectivity is $< 10\%$. Reproducibility of degradation results in the present work is deduced from the extent of deviations in the measured mass loss values and thereby MDD values at different immersion times. The evidence of huge scatter in MDD error bar values indicates a non-reproducible nature of degradation in the specimens with high pore interconnectivities (18% and 21% porosities). This wide deviation in the MDD error bar values disappears in the degrading specimens with porosities $\leq 12\%$ indicating a high degradation reproducibility.

The pore interconnectivity value of 10% in the present work means that the largest pore occupies 10% of the total pore volume and that it can be at random locations within the specimen including the surface contributing to the surface open porosity. In general, a large pore interconnectivity value with very low surface open pore fraction indicates an inherently non-uniform porosity distribution existing in the specimen. This is not desirable for degradation studies as the degradation may become uncontrolled when this large pore becomes available for the external medium due to progressive degradation. A large pore interconnectivity with high surface open pore fraction (specimen porosities of 18% and 21% in the present work), indicates a high chance for non-homogeneity with respect to specimen degradation. The case of low pore interconnectivity with low surface pore fraction implies a material towards bulk properties (specimen porosities of $\leq 10\%$ in the present work) which are highly favorable for homogeneous and reproducible degradation. The case of higher surface open pore fraction with low interconnectivities may indicate a better chance for reproducible and homogeneous degradation (specimen porosities of 12% in the present work) as the capillary forces that purge cell culture medium from the surface to the specimen internal pores are limited just to the surface open pores. In addition, the degradation layer that forms due to the influence of protein complex in the cell culture medium is known to alter the degradation kinetics [95, 185, 186]. The prerequisite for a persistent reproducible degradation in the last case scenario may arise from the actual values of the combined pore interconnectivity and surface open pore fraction for the material under investigation. In the present work, these values are observed to be $< 10\%$ and $< 45\%$, respectively, resulting in the degradation rate of 1.57 mm/year in Mg-0.6Ca (Mg/Mg-10Ca) specimens with 12% porosity. These values also act towards exhibiting a reproducible and homogeneous degradation in these specimens.

This behavior of varied degradation due to porosity is indeed documented in the literature [15, 49, 97, 187]. The interconnected pore channels in high porosity specimens are reported to increase the capillary action of the water based DMEM cell culture medium leading to high degradation. Although degradation can occur from within the pore once the

medium reaches the pore walls, the kinetics of degradation may differ to that of the surface [188]. Jia et al. have reported for open porous magnesium scaffolds that the formed degradation layer thickness in the internal pore walls remained constant even after 56 days immersion unlike the layer formed on the surface which increased in thickness with immersion time [97]. They reported the formation of degradation layer on the surface reduced the further input of medium inside the pore. Though their immersion test conditions are similar to the present work with interconnected pore structures, as in specimens with 18% and 21% porosity categories, the porosity and pore sizes they studied were many orders of magnitude higher than shown in the present work. In case of micro pores, as in the present study Figure 5-9 A, variation in the local environment of the formed pit or pore i.e. depletion of cathodic reactants inside the pit favors an auto-catalytic cell as long as aggressive anions, like chlorides, are able to penetrate the degradation layer [189]. This type of cell causes local acidic environment inside pit and may further self-propagate pitting by reacting with metal cations inside the pit. In addition, presence of secondary phases or impurities adjacent to pore walls can generate lateral pitting. In the present study, degradation is observed only macroscopically and therefore multiple degradation mechanisms are expected to act at the pore sites. Degradation results of Mg-0.1Si alloy with porous defects during casting were investigated by Cao et al. [187]. They reported degradation rate via mass loss measurements as 0.7 mm/year and 3.7 mm/year for specimens with no defects at the surface and in specimens containing small pores after solution heat treatment, respectively. They attributed the increase in degradation rate to the increased surface area and the presence of impurity at the pores which are the lastly solidified areas in cast materials. Eventually, an increased galvanic corrosion is postulated as the reason for an increased degradation in these specimens [187]. In the present work, though impurities did exist, they are measured to be in similar quantities in all porous Mg-0.6Ca (Mg/Mg-10Ca) specimens investigated prior to immersion testing (Table 4). Phases like Mg_2Ca are reported to be anodic and preferentially dissolve prior to the magnesium matrix. However, Mg_2Ca is found not continuous but only at discrete areas of grain boundaries (Figure 5-6 A to D). This probably had less influence on degradation. The presence of Mg/Ca/Si rich phases (Figure 5-6 A to D) indicate possible elimination of detrimental effects arising from silicon and iron combinations on magnesium degradation [84]. In addition, no cracks or defects apart from inherent material porosity are observed in the microstructures (section 5.3 and Figure 4-3 B). These observations confirm that the observed specimen degradation is indeed due to the pore interconnectivity and surface open pore fraction associated to specimens with different porosity categories.

Since no degradation layer thickness measurements or cross-sectional analysis were performed in the present work, it is difficult to comment on the density of the formed degradation layer for different porous specimens. However, porosity dependent changes in the nature of degradation layer can be qualitatively inferred from Figure 5-20 A and B. In specimens with porosities $\leq 10\%$, the amount of formed degradation layer remains fairly constant, irrespective of immersion time. This, in combination with the low osmolality

change (Figure 5-20 A) and low degradation rates (< 0.3 mm/year) in these specimens indicates a probable uniformity in the formed degradation layer. At specimen porosity $\geq 12\%$, a non-uniformity in the layer formed due to an increase in the exposed surface area with increased specimen porosity can be witnessed. Since material losses can occur during handling of specimens with degradation layer, this analysis remains fairly qualitative. However, the results are indicative that low porosity ($< 10\%$) Mg-0.6Ca (Mg/Mg-10Ca) specimens tend to form a stable degradation products layer compared to the higher porous specimens due to less exposed surface area to the cell culture medium.

The degradation rate values obtained in the present work (< 0.3 mm/year) is lower than the degradation rates reported for specimens with no surface defects i.e., dense specimens [187]. Even at 10% specimen porosity, the present work showed that the degradation rate of porous Mg-0.6Ca specimens is only three fold higher than the bulk pure magnesium (DR of 0.09 mm/year), under similar degradation test conditions to the present work [99]. This result is important as it establishes that PM Mg-0.6Ca specimen porosity in its pure numerical value does not directly indicate an inferior degradation performance and that there are other forces at work like degradation layer and the surface open pore fraction that control degradation rate despite the specimen porous nature. The results also display a robust Mg-0.6Ca material fabricated by PM technique that degrades homogeneously with low degradation rates irrespective to changes in process parameter like sintering temperature, provided sintering temperatures are ≥ 570 °C.

6.2.2 Pore shape and pore size distribution

The 2D pore assessment through microstructures in sintered specimens reported in the literature indicates that pores are either cylindrical or spherical at higher sinter densities [190, 191]. This is, however, not completely true as shown by a combined focused ion beam and electron microscopy characterization of evolving pores during solid state sintering of ZnO nanoparticles by Chen et al. [192] and in Zirconia by Xia et al. [193]. Their 3D pore tortuosity calculations, based on a series of inflexion points depending on the interconnected nature of pores, indicated that pores do exhibit a certain tortuosity value even at sinter densities as high as 96%. This means that certain large pores have non-spherical shapes even though the total specimen porosity is low. Though a threshold pore size below which the spherical pore nature prevails was not determined in the present work, similar observations to the above findings like convoluted pore structures were illustrated in Figure 5-7 and represented in the form of surface curvature measurements in Figure 5-8. The reason for the difference in shapes of all segmented pores to that of the largest pore within the specimen of same porosity (as example, in Figure 5-8 G to H) is presumed to be due to an enhanced rearrangement densification due to increased localized liquid phase activity occurring at sintering temperatures > 570 °C [43, 194]. In addition, at these high temperatures, pores in sizes of 45 - 63 μm can be formed at random sites where master alloy particles liquify that may variably spread into the surroundings due to grain size dependent capillary forces [43, 195]. Therefore, the final shape of the large pores is dictated

by the combination of primary and secondary pores formed between pure magnesium particles and master alloy melting, respectively, that can expectedly be convoluted and non-spherical in nature. Combining the results of curvature distributions of all segmented pore volumes in specimens with $\leq 12\%$ porosities (Figure 5-8 E, G and I) to their respective pore size distributions in Figure 5-9 A, it can be inferred that the observed spherical pore morphology attributes to the formation of small pores during sintering. This, as expected, agrees with general postulate that majority of isolated small pores obtain a spheroidal shape during final stages of sintering [196].

From curvature measurements, the largest pore in specimens with $\leq 12\%$ porosity tends to possess a pit type or concave saddle type surfaces that may favor further degradation due to their high specific surface compared to a flat one, if liquid is able to access these pores (Figure 5-8; right column). The surface area to volume ratio of non-spherical geometrical shapes is high, indicating that these large pores may expose a higher surface at some point during progressive material degradation [187]. In this regard, such large pores, though insignificant in number, can be detrimental to specimen degradation. As mentioned in equation (15), the largest pore volume in these specimens with $\leq 12\%$ porosity corresponds to the pore interconnectivity value i.e., $< 10\%$. In a separate measurement, it is also observed that the overall volume contribution from the ten largest pores does not exceed 15% of the total investigated pore volume ($700 \mu\text{m} \times 700 \mu\text{m} \times 500 \mu\text{m}$) in these specimens. This indicates that the curvature of the largest pore, though different to that of the curvature distribution of rest of the pores, may not contribute significantly to specimen degradation. In view of material's degradation, the closed nature of pores is considered more important than the actual pore shape. In view of these observations, it is inferred that the shape effect of the large pores on degradation may not be as significant as the degradation effect arising from the surface open pores that are exposed directly to the cell culture medium. Additionally, from a practical standpoint, the ability of the liquid entering the pores and progressing degradation can depend on pore opening, surface tension, volume of the pore etc. [97]. It is, therefore, established from the present work observations that the pore interconnectivity is in fact the most important pore morphological feature that determines the degradation reproducibility in porous Mg-0.6Ca (Mg/Mg-10Ca) specimens. This value when it is $< 10\%$, ensures a reproducible degradation in PM Mg-0.6Ca system.

6.3 Generalized criterion for degradation reproducibility in view of magnesium material porosity

Based on the discussions in sections 6.2.1 and 6.2.2, to achieve a reproducible degradation result in PM magnesium materials, a low pore interconnectivity ($< 10\%$ in PM Mg-0.6Ca specimens) in addition to the fraction of surface open porosity has to be monitored ($< 45\%$ in PM Mg-0.6Ca specimens), as this determines the initial degradation during initial specimen immersion. As long as the majority of the formed pores are of smaller diameters ($< 20 \mu\text{m}$ in PM Mg-0.6Ca specimens), the shape of the pores appears to be less relevant for altering the degradation profiles in porous magnesium materials.

Contrary to the general concept of only high-density materials possessing good degradation results, the present work proved that porous PM Mg-0.6Ca specimens can exhibit reproducible degradation until threshold porosities nearing 12%, that are considered high porosity ranges in other PM metallic systems. Additionally, a robust PM Mg-0.6Ca material possessing homogeneous degradation and low degradation rates (< 0.3 mm/year) can be processed by sintering at any temperatures that are ≥ 574 °C. This is supported by the optimal combination of pore interconnectivity ($< 10\%$) and surface pore fraction ($< 45\%$) values in PM Mg-0.6Ca specimens. It should be noted that this absolute threshold porosity value for a reproducible degradation might vary for different porous magnesium systems due to alloying element concentrations, impurities and the nature of additives used for generating porosity etc. As degradation is affected by several other material features in addition to just porosity, postulating a certain set of morphological pore parameters for reproducible and homogeneous degradation based on experiments on single alloy system can be misleading. Nevertheless, the general conscience of low impurity concentrations (iron, copper, nickel < 29 ppm, 40 ppm, 12 ppm, respectively for porous PM Mg-0.6Ca specimens) and low pore interconnectivity ($< 10\%$ for PM Mg-0.6Ca specimens) in PM fabricated magnesium materials can provide a reliable initial step towards achieving both reproducible and homogeneous degradation properties.

6.4 Surface oxide and grain boundary pinning effects in PM Mg-0.6Ca

Grain growth is a usual occurrence during sintering and grain size is reported to increase with sintering time [39, 54]. However, in the present work, no significant grain growth is seen in Mg-0.6Ca (Mg/Mg-10Ca) specimens even after longer sintering durations of 63 h (Figure 5-10 A and B). In fact, similar observations were reported in MIM Mg-0.9Ca material where a fine grain structure is evident even after 63 h sintering [9]. This behavior, however, is altered in the present study in Mg-0.6Ca (Mg_{sieved}/Mg-10Ca) specimens when sieved pure magnesium powders are used in preparing Mg-0.6Ca powder mix and thereby Mg-0.6Ca specimens produced using this powder mix. In these specimens, a heterogeneous grain growth is observed (Figure 5-10 C and D). With the sintering conditions being essentially the same between these specimens (Figure 4-5 A; 627 °C), the disparity in the microstructure relates directly to the influence of sieved pure magnesium powders on promoting heterogeneous grain growth. Comparing pure magnesium powder surfaces in Figure 5-15 to Figure 5-16, it can be observed that impurity features on pure magnesium powder surfaces were reduced after the mechanical sieving treatment. They also suggest the removal of the impurity features that are only physically adsorbed on pure magnesium powder surface due to the aberrations created by the vibrating sieves. Table 3 quantifies this surface change to a near three-fold decrease in silicon concentration before (~ 221 ppm) and after (~ 84 ppm) sieving treatment of pure magnesium powders.

Though MgO is the most anticipated oxide that forms readily on pure magnesium surfaces, the possibility of other impurity oxides such as silicon or carbonaceous-type cannot be ignored [197]. Silicon is a commonly reported impurity existing in oxide form in

magnesium raw materials [117, 198]. Gas atomized powder surfaces are prone to different phase formations depending on the atmospheric impurities, alloying additions and degree of undercooling [199, 200]. In addition, magnesium powders may form hydroxides due to moisture present in the processing or storage atmosphere [8, 35]. These hydroxide and carbonaceous compounds are reported to vaporize or dissociate at sintering temperatures greater than 350 °C [201]. In the present work, the particle type oxides, however, are still seen on sieved pure magnesium powders probably due to the cold fusion of these particles on to the surfaces as shown in Figure 5-16 B, D, E and F. However, minimizing them in the early powder stage i.e., prior to specimen compaction step ensures an overall reduction in oxide concentration during sintering stage. This becomes essential as the reduced oxide content indicates less oxide pinning effect prevailing at the grain boundaries as these oxides are seen primarily along the grain boundaries of sintered microstructures as in Figure 5-6 A to D. It is plausible that different particle sizes of pure magnesium possess surface impurities in different quantities due to the differences in their surface areas. In addition, different powder sizes may not respond the same way to the aberrations caused by the vibratory sieves resulting in a difference in their oxide contents after sieving. This implies a variation in the pinning effect at different grain boundaries during sintering of Mg-0.6Ca ($Mg_{\text{sieved}}/Mg-10Ca$) specimens leading to a heterogeneous grain growth behavior. Local conditions favoring breakaway of the boundary from coherent or incoherent particles in a non-homogeneous manner are reported for the erratic and abrupt grain coarsening in metallic sintering systems [202]. Furthermore, the particle assisted heterogeneous grain growth is reported to be followed by an incubation time [58, 60, 203]. This is seen in present work in section 5.6.2, where heterogeneous grain growth is observed after 18 h sintering in Mg-0.6Ca ($Mg_{\text{sieved}}/Mg-10Ca$) specimens. Only recently it has been reported by Schaper et al. that grain growth is indeed occurred in Mg AZ81 specimens when specimens are heat treated for 10 h at 400 °C and was attributed to the reduced grain boundary pinning [7]. Similar reduction in pinning effect on grain boundaries is reported due to reduction in complex Ti-Zr oxynitride particles with overall reduction in nitrogen content in sintering atmosphere [55].

It is anticipated that there is potential for grains to further coarsen, probably in a heterogeneous way, also in these specimens if longer sintering times greater than 63 h are provided. However, in comparison, the reduced oxide pinning effect in Mg-0.6Ca ($Mg_{\text{sieved}}/Mg-10Ca$) specimens has brought down the sintering time for the onset of heterogeneous grain growth to 18 h (Table 6). This onset sintering time for grain growth, however, may be taken as only arbitrary. This is because it is difficult to pin point the exact sintering time when grain growth may occur due to the erratic nature of abnormal grain growth in particle assisted systems [204, 205]. The composition of these oxides on pure magnesium powders in the present study could not be determined by EDX as the strong pure magnesium signal superseded any other trace element on the surface due to higher depth of penetration of the electron beam into the material. In addition, the trials for oxygen content determination on pure magnesium powders by combustion analysis failed

due to the limitations that arouse from the reaction between magnesium vapor and carbon monoxide gas at the temperatures used during analysis [206]. In this regard, the oxide content discussion in the present study remains semi quantitative based on the differences in visual inspection of powder surfaces as shown in Figure 5-15 and Figure 5-16 and chemical analysis of pure magnesium powders listed in Table 3. However, based on the similarities of current observations to the reported literature, heterogeneous grain growth in the present study is attributed to the reduced oxide pinning effect at grain boundaries due to reduction in overall surface oxide content in sieved pure magnesium powders.

In liquid phase sintering systems like alumina with 5 wt.% talc composition, rapid densification is reported during the initial melt formation where maximum densification occurred after 2 h at relatively low sintering temperatures [59]. Liquid phase is known to promote faster solid particle rearrangement after its formation at desired temperatures. This becomes essential for pore filling by liquid where in the later stages of sintering, grains grow towards the liquid filled pore by material redeposition through liquid transport medium [207]. Grain growth is reported as an essential criterion for pore filling and that the liquid flows into the pores when grain size around the pore reaches a critical value. Pore filling is reported to occur in a chronological order subsequently leading to an increase in specimen density [207, 208]. However, as mentioned in Table 6, increase in specimen density with subsequent grain coarsening is not evident in the present work, despite a persistent liquid phase at 626 °C in Mg-0.6Ca system. This indicates that pore filling theory may not be the relevant mechanism for the heterogeneous grain growth observed in the present work. It should be noted that in Table 6, different Mg-0.6Ca green compacts were used for the different sintering runs instead of subjecting the same green specimens to sintering runs with increasing sintering times. Nevertheless, the sinter densities comparison is still valid as these specimens were processed the same way from the beginning raw powders, sieving treatment, sintering conditions (except for sintering times) and the resultant heterogeneous grain growth is observed consistently. After the initial heterogeneous grain growth at 18 h sintering time, the grain boundaries may have interfered with next wave of pinning particles leading to a stagnation of the grain growth indicating no significant grain structure differences between 18 h and 63 h (Figure 5-17 A to C).

The trapped gases in the pores and their solubility in the matrix at high sintering temperatures are reported to decline the final density of sintered part [209]. In the present work, no bloating, swelling or surface cracking is observed on the external surfaces of the as sintered specimens when sintered at 626 °C, as shown in Figure 4-3 B. This indicates an equilibrium pore pressure with respect to ambient furnace pressures by the employed high purity argon sintering atmosphere. Additionally, in Figure 5-11 A to C and Figure 5-12 A, the maximum pore sizes after sintering tend not to exceed the size of the liquid forming master alloy particle sizes 45 - 63 μm . These observations along with no sinter density change despite the use of different initial green compacts hold true for all Mg-0.6Ca ($\text{Mg}_{\text{sieved}}$ /Mg-10Ca) specimens, therefore indicating robustness in the employed process. The only

variable parameter is the sintering time that alters the onset of heterogeneous grain growth in these specimens due to the reduction in oxide content.

The present work also revealed that for a given sintering time, the size of the liquid forming Mg-10Ca master alloy powder also promotes heterogeneous grain growth in Mg-0.6Ca (Mg_{sieved}/Mg-10Ca) specimens (section 5.6.3). By comparing microstructures in Figure 5-18 A, B (Mg_{sieved}/Mg-10Ca size \rightarrow $< 45 \mu\text{m}$ / $< 32\mu\text{m}$) to Figure 5-17 C (Mg_{sieved}/Mg-10Ca size \rightarrow $< 45 \mu\text{m}$ / $45 - 63 \mu\text{m}$), it can be observed that at the approximate powder size ratio of 2 : 1 (Mg-10Ca : sieved pure magnesium), the heterogeneous grain growth initiates after 18 h of sintering. This ratio has been determined based on the d_{50} value of the as received pure magnesium and the average size of Mg-10Ca powders listed in Table 3. This indicates that high calcium rich liquid contents at localized sites of the compact may dominate the grain growth process. The fast distribution of such liquids may cause enhanced rearrangement CaO formation thereby suppressing the pinning effect from impurity oxide particles [8, 210]. These observations indicate that both liquid forming additive size and the magnesium powder surface oxide content play differing dominant roles in determining the final grain structure in PM Mg-0.6Ca specimens. In this regard, it is hypothesized that the heterogeneous grain growth during sintering may still occur, irrespective to the magnesium powder surface oxide content, when Mg-10Ca powder sizes are sufficiently large (compared to pure magnesium powder) to create localized superfluous liquids within the specimen. This is because solid particle rearrangement is reported to be enhanced by increased liquid phase activity during sintering that can effectively reduce the incubation time for grain growth [39, 210].

6.5 Effect of heterogeneous grain structure on PM Mg-0.6Ca degradation

Figure 5-22 illustrates that the mass loss and thereby the mean degradation depth of the Mg-0.6Ca (Mg_{sieved}/Mg-10Ca) specimens is accompanied by a huge disparity in the scatter of their MDD error bar values during the later stages of immersion i.e., after a week. This indicates a loss of degradation reproducibility in these specimens with progressive immersion times. Since the starting raw powders chemical compositions (Table 3), impurity concentrations of the specimens prior to immersion test (Table 4) and sintering parameters (Figure 4-5; 627 °C light green line) remain the same to that of Mg-0.6Ca (Mg/Mg-10Ca) specimens, the change in the degradation profiles of Mg-0.6Ca (Mg_{sieved}/Mg-10Ca) specimens compared to Mg-0.6Ca (Mg/Mg-10Ca) specimens can be majorly attributed to their differing grain structures as shown in Figure 5-10 A and C, respectively. As mentioned in section 4.3, the samples in powder and sinter compact forms were transformed to their solution forms prior to the chemical analysis by AAS. This gives an average impurity value for the measured powder sample and therefore the localized deposits of iron and/or copper on powder surfaces due to possible contamination from the sieves may be obscured. Despite no significant to a very slight increase in the average iron and copper values was observed on pure magnesium powders before and after sieving treatment (Table 3), a possible localization of impurities may still negatively impact the degradation resistance in PM Mg-

0.6Ca specimens. Hence, this possibility of sieving contaminations on pure magnesium powder surfaces cannot be ignored, though their effect on degradation is not explicitly evident in the present work. However, the impurity concentrations in both Mg-0.6Ca ($Mg_{\text{sieved}}/Mg-10Ca$) and Mg-0.6Ca ($Mg/Mg-10Ca$) specimens prior to immersion testing (Table 4) remain in the same quantities correlating the observed degradation in Figure 5-22 to the specimen heterogeneous grain structure.

With respect to the effect of grain size on degradation, the reported literature indicates that for a given cell culture medium, the degradation resistance of magnesium alloys may either improve or deteriorate with grain size refinement (see section 2.4.3). Material degradation is also generally reported to initiate at the grain boundaries as they are high energy regions. The introduction of grain boundaries then leads to an increase in the local anodic-cathodic areas and therefore degradation rate, supposedly, increases [148]. For a huge volume fraction of grain boundaries in a given area, as in fine-grained magnesium material, the degradation resistance is expected to be reduced in presence of an aggressive cell culture medium [156]. However, increased degradation resistance for fine-grained magnesium materials is attributed to the continuous formation of the passive MgO layer due to high volume fraction of grain boundaries and to the fast initial electrochemical reactions that favor an earlier formation of degradation products compared to the coarse-grained microstructures [74, 211]. The mix of fine- and coarse-grained structures within the same microstructure of specimen, as in the present work (Figure 5-11 and Figure 5-12), indicates the possibility of the variation in degradation due to varying grain sizes. However, the observations reported in the literature relate the magnesium alloy degradation only to the grain size variations and other phase changes associated with grain growth are not reported [74, 148, 156, 157, 211-213].

In the present work, it was also witnessed that the grain coarsening is adjoined by a non-homogeneous duplex microstructure that is possibly associated with the varying local calcium concentrations in magnesium matrix. This can be seen in Figure 5-11 through Figure 5-13, where certain matrix grain boundaries are composed of MgO and Mg₂Ca phase and the others additionally seen with eutectic lamellar structure $\alpha\text{-Mg} + \text{Mg}_2\text{Ca}$. The degradation in such specimens can be discussed based on the nature of secondary phases developed after sintering [120]. The presence of secondary phases in magnesium are considered to form galvanic couples that make magnesium grains preferentially degrading anodes [214]. However, recent studies by Liu et al. indicated that due to the high reactivity of secondary phase like Mg₂Ca, local cathodic sites appear nearby Mg₂Ca phase whilst Mg₂Ca itself behaves anodic when galvanically coupled to magnesium [80]. The authors suggested that this behavior can be beneficial in lowering the potential difference between anodic Mg₂Ca and cathodic magnesium, provided Mg₂Ca is finely dispersed in magnesium matrix avoiding local high Mg₂Ca/Mg ratios [215, 216]. This is the case in Mg-1.0Ca alloy system where Hou et al. [81] reported a highly localized corrosion attack at the micro eutectic Mg₂Ca/Mg lamellar sites [81]. This is also observed in Mg-0.8Ca system where eutectic structure resulted in speedy dissolution of Mg₂Ca phase resulting in an undercutting of magnesium

matrix [79]. In brief view of these recent reports, it can be expected that the duplex microstructure shown in Figure 5-11 through Figure 5-13 might exhibit certain regions inhibiting degradation while certain regions promoting localized attack leading to the disparity in mass loss between degrading specimens. The deviation in mass loss between degrading specimens was less within the first one week of immersion. This can be attributed to the used cell culture medium DMEM Glutamax. This medium in general is reported to promote slow degradation in magnesium alloys [4, 217]. With increasing immersion duration, however, new areas beneath the degrading surface may get exposed and alter the mass loss behavior in the overall specimen [218]. As shown in Figure 5-12 B and Figure 5-17 E and F, the eutectic structure itself is localized and the same localization at certain grain boundaries can be expected in the deeper layers of the specimen which can potentially cause variation in degradation and mass loss seen. In addition, the evidence of cathodic active sites of Mg/Ca/Si phase adjoining eutectic structure (Figure 5-11 through Figure 5-14) might contribute to variability in local degradation [116].

The microstructures at certain locations of Mg-0.6Ca (Mg_{sieved} /Mg-10Ca) specimens (like fine-grained areas in Figure 5-11) indicate a lower calcium composition leading to Mg_2Ca formation and other regions (like eutectic structure $\alpha\text{-Mg} + Mg_2Ca$) indicate a higher calcium concentration exceeding the calcium solubility limit in magnesium matrix (which is 0.74 wt.%). In addition, the specimens sinter densities do not change between 3 h till 12 h of sintering, indicating that microstructural homogeneity is indeed achieved (section 5.6.2). It is only after sintering for 18 h that the microstructural non-homogeneity occurred as shown in Figure 5-17 D to F, assisted with heterogeneously growing grains. In view of these observations, the microstructural non-homogeneity can be attributed to the calcium redistribution in the magnesium matrix due to heterogenous growing grains in Mg-0.6Ca (Mg_{sieved} /Mg-10Ca) specimens. The exact reasons for this eutectic structure formation, however, are not clear. As mentioned earlier, the heterogeneous grain growth is attributed to the reduced particle pinning effect at the grain boundaries of Mg-0.6Ca (Mg_{sieved} /Mg-10Ca) specimens. In addition, literature also suggests migration of grain boundary liquid particles/pockets due to grain boundary migrations during grain growth [219]. Such an effect is reported to exist due to the chemical inhomogeneity between the phases and the matrix or can be simply temperature induced. The resultant microstructures are reported to have an increased particle segregation along the moving boundaries [220, 221]. In the present work, Mg_2Ca phases are found also within the enlarged grains as shown in calcium elemental maps in Figure 5-13 and Figure 5-14, sometimes located along the boundaries of smaller sized grains prior to the heterogeneous grain growth initiation. This indicates a possibility for a weaker liquid phase migration in PM Mg-0.6Ca system. However, the conditions that favor eutectic structure formation in Mg-Ca system i.e., calcium contents greater than 0.74 wt.%, are closer to the equilibrium alloy concentration of the present work at 0.6 wt.% (Figure 2-5). Theoretically, even weaker liquid phase migrations can lead to calcium enriched areas resulting in calcium contents greater than 0.74 especially at grain boundary junctions as shown in Figure 5-13 A and B. It can be further seen in Figure 5-13 B

inset that the region in the vicinity of eutectic structure is devoid of calcium rich precipitation similar to literature observations where grain boundary movements created a denuded precipitate regions just behind the moving boundaries [219]. However, to confirm the liquid phase migration and to understand the behavior of calcium rich liquid phase during grain growth, further experiments will be necessary.

6.6 Degradation reproducibility in relation to grain size of PM Mg materials

The present work showed that the oxide impurities help towards attaining homogeneous grain sizes in Mg-0.6Ca (Mg/Mg-10Ca) specimens, that benefit positively the final degradation properties (section 5.7.1). However, when grain growth is inevitable to occur at a certain stage of sintering, it is now predictable that the growth can be heterogeneous in magnesium materials due to these very oxide impurities that previously showed benefits. The present work also showed that heterogeneous grain structure is associated with phase changes that deteriorate the degradation reproducibility in Mg-0.6Ca (Mg_{sieved}/Mg-10Ca) specimens (section 5.7.2). Such a heterogeneous grain growth behavior may not be limited just to the conventional 'press and sinter' specimens as in the present study but also to other AM techniques so long the starting powders possess an impurity oxide surface. Inert gas atomization for producing pure magnesium powders may be one possible route to minimize the surface oxide content. This might be interesting in the research perspective; however, it does increase the risk factor and cost of production from a practical standpoint. Therefore, from a material processing perspective, when using gas atomized magnesium powders for fabricating Mg-Ca alloy systems, the sintering time has to be optimized for the alloy of interest to achieve a homogeneous grain structure throughout the material. As the onset sintering time for the heterogeneous grain growth might vary depending on the powder surface oxide content, the surface characterization for powders has to be performed after subjecting the powders to treatments that may modify their surfaces physically or chemically. This is because, the present study showed that a simple and the most common way for powder size segregation like sieving can modify the pure magnesium powder surfaces causing heterogeneous grain growth. In addition, the use of fine liquid forming additive particle sizes in combination with fine pure magnesium powders is recommended to prevent localization of high concentrations of liquids during sintering. The size disparity in the used powders has the potential to cause heterogeneous grain growth at short sintering times (Figure 5-18). Additionally, the resulting large pore sizes can be detrimental to mechanical properties. The use of pre-alloyed magnesium powders can be an alternative to overcome the chemical inhomogeneity between different powder particles. However, huge size disparity between pre-alloyed powders within the compact may also cause high local liquefaction possibly causing undesirable microstructural features. In this regard, towards developing new magnesium alloys by PM for biomedical applications, powder blending route due to its versatility and cost saving is still viewed as a good initial point as long as starting powders of similar size ranges are chosen. The production of pre-alloyed powders for various test compositions, variable micro alloying and powder size

fractions without prior knowledge of the desired alloy composition may consume a huge amount of time and may involve a high cost of production.

6.7 Strength profiles of PM Mg-0.6Ca in relation to microstructure

Pores or other defects formed during material processing act as the plausible crack initiation sites during deformation loading [222]. The progress of deformation is then expected to follow the path of weakest resistance offered by the bulk material which is both bulk microstructure and struct thickness dependent [223]. In the present work, when overall specimen porosity decreased, the surface open porosity decreased with a simultaneous decrease in the sizes of the isolated pores (Figure 5-9). This qualitatively indicates an increased resistance of the material bulk to the deformation path following the crack initiation at the surface. From Table 5, a certain increase in the pore number is witnessed with decreasing specimen porosity. However, this pore number increase seems to have an insignificant effect on material tensile strengths. Obviously, the small size effect of the isolated pores is compensating for the increased pore numbers leading to an overall decrease in the pore volume of the specimens. This is finally seen as the improved strength profiles with decreasing specimen porosity in Mg-0.6Ca (Mg/Mg-10Ca) specimens. The recorded UTS and elongation to failure for specimens possessing porosity 3% and 6% are comparable to extruded Mg-0.6Ca specimens with zero porosity [224]. In fact, the linear extrapolation of UTS to 0% specimen porosity in Figure 5-24 B indicates that the bulk tensile strengths of PM Mg-0.6Ca specimens is similar to that of hot extruded Mg-0.54Ca that are reported to be 170 - 180 MPa with elongation to failure values of around 3%. In the present work, the enhanced elongation to failure values of 7 - 8% can also be attributed to the homogeneous alloy microstructure with no effect from texture, which is otherwise present in extruded specimens. The presence of oxides and Mg₂Ca precipitates at the grain boundaries are seen at all sintering temperatures in Figure 5-4 and Figure 5-6. Since the oxides are inert and brittle in nature and no grain growth is observed in the sintered specimens (section 5.3), this would mean a high particle pinning area per unit volume of the grain boundary. The enhanced mechanical properties can further be attributed to this particle pinning effect customary to sintered magnesium alloys [7].

Addition of calcium is reported to improve the hardness, mechanical strength of pure magnesium, however, calcium concentrations ≥ 1 wt.% decrease the ductility in the alloy [72, 77, 225]. In addition to existing phases, formation of new phases because of calcium could also favor this increase in mechanical properties [225]. Chino et al. also demonstrated high temperature strength by addition of 0.9 wt.% calcium to magnesium. The strength exhibited was more than twice compared to pure magnesium at temperature range of 473 - 673 K [226]. In as-cast Mg-Ca alloys, the increase of calcium improved the tensile and yield strengths at the cost of ductility as demonstrated by Kim et al. [216]. However, the work conducted by Li et al. [77] also demonstrated a drop in tensile strength and elongation in as cast Mg-Ca alloys with increasing calcium content. They observed a decrease in tensile ductility at about 1 wt.% Ca. More than 2 wt.% Ca resulted in brittle fracture. They

attributed the decrease in ductility to the formation of a continuous eutectic/ secondary phase along the grain boundaries which would accelerate the crack propagation. But such a decrease in neither tensile strength nor elongation to failure has not been observed in the present work in Mg-0.6Ca (Mg_{sieved}/Mg-10Ca) specimens which exhibited both eutectic α -Mg + Mg₂Ca structures and regular Mg₂Ca phases at grain boundaries (Figure 5-25). Clearly, the eutectic phase is not continuous and the presence of oxides is still seen in grain coarsened microstructures (Figure 5-13). Hence, the mechanical properties did not deteriorate but remained in the range similar to that of Mg-0.6Ca (Mg/Mg-10Ca) specimens possessing homogeneous grain structure. In addition, presence of oxide particles, as in within the heterogeneously coarsened grains may act as barriers, additional to the grain boundary phases, for the movement of dislocations or twins formed by premature deformation during tensile loading conditions.

In magnesium alloys, mechanical properties are known to be influenced by texture and twinning due to processing [114]. The dense packed basal plane of pure magnesium initiates the slip during deformation loading which possesses two active slip planes. Five independent slip systems are required to ensure a homogeneous deformation without formation of cracks according to Von Mises criterion. But the basal plane constitutes to only two active slips and is considered to be the reason for ductility issues in pure magnesium [227, 228]. However, polycrystalline magnesium alloys show higher elongation to fracture values (as example, $\sim 8\%$ in PM Mg-0.6Ca specimens, Figure 5-25) implying that Von Mises criterion is still fulfilled with the intervention of other slip systems like prismatic slip and pyramidal slip systems which accommodate 2 and 1 active slip planes, respectively. In addition, twinning in magnesium alloys is reported to influence the ductility [227]. In view of these observations, multiple deformation mechanisms are seen to play different roles that cause the strength and elongation to failure values that are shown in Figure 5-24 and Figure 5-25 for homogeneous and heterogeneous grain structures in PM Mg-0.6Ca specimens, respectively. However, it can be ascertained that mechanical properties are not deteriorated with respect to specimen grain size in the presented PM Mg-0.6Ca system.

6.8 Basic suitability of PM Mg-0.6Ca as bone implant material

The compressive strength of human cancellous bone is reported to be 2 - 80 MPa with pore sizes ranging up to 300 μm . Highest osteoblast proliferation was reported in collagen based scaffolds with mean pore sizes greater than 300 μm [229]. The threshold pore throat size, though material dependent, suitable for tissue ingrowth is reported to be nearly 52 μm in porous titanium constructs [230]. Effective bone ingrowth was reported at pore sizes of 20 μm in hydroxyapatite based scaffolds [231]. In addition, different cell migrations and cell-cell interactions might require a complex mix of pore size, cell-type dependent compatibility and permeability of scaffolds [232]. Micron sized pores (25 - 53 μm) induced into MgP scaffolds showed enhanced bone remodeling compared to the MgP scaffolds with only macro pores of 300 μm size [15]. The same is observed in CaP scaffolds where a higher bone volume fraction is observed *in vivo* in the scaffolds with additional micropores after

implantation in pig mandibles for three weeks. These reports indicate that micro porous structures in scaffolds provide micro capillary induced forces that promote bone ingrowth in relation to the scaffold biodegradation in vivo. However, many of such literature indicate that experiments are to be designed for specific target application with customized pore sizes and required strengths of materials. In the present work, the tensile strengths recorded for porous Mg-0.6Ca (Mg/Mg-10Ca) specimens are in the range of the human cancellous bone (Figure 5-24 and Table 9). Furthermore, the variation in mechanical properties with varying porosity implies material suitability for a broader range of applications. Mg-0.6Ca (Mg/Mg-10Ca) specimens with < 12% porosity can be promoted for load bearing implant applications where only slight variation in degradation rates are desired. Specimens with 12% porosity showed positive traits of degradation reproducibility and optimal mechanical properties. Possessing surface open pores of about 45%, they can be further improved for use in applications where high material release is required with less demanding mechanical properties. A word of caution is that high degradation rate of nearly 1.6 mm/year in these specimens may not be favorable for cell adhesion and subsequent treatments that improve cell adhesion properties may be required [4, 111]. The highly interconnected pore structures with acceptable degradation rates, though not homogeneous, and amendable mechanical properties in range of cancellous bone (i.e., specimens with 18% and 21% porosities) can be exploited further to produce altered or uniform pore sizes to test for their general applicability as scaffold materials.

7 Conclusions

The present work investigated the effects of material microstructural features, namely, grain size and porosity on the degradation behavior and tensile strength profiles of PM Mg-0.6Ca specimens. With the employment of spectroscopy, μ CT and extensive electron microscopy analyses combined with the findings from published literature, the crucial material parameter thresholds and therefore the processing conditions to achieve homogeneity and reproducibility in degradation behavior of PM Mg-0.6Ca specimens were realized. The conclusions of the work are as follows:

- A) The present study proved that porosity is not instantly detrimental to the degradation resistance of PM Mg-0.6Ca system. The threshold specimen porosity to achieve a homogeneous and reproducible degradation can be as high as 12%. If degradation rates of < 0.3 mm/year are desired, then the threshold porosity drops to 10%. This additionally shows PM Mg-0.6Ca material to be robust in its degradation characteristics until 10% porosity.
- B) Pore interconnectivity is the important factor controlling the homogeneity and degradation reproducibility in PM Mg-0.6Ca specimens. A pore interconnectivity value of $< 10\%$, found in specimens with porosities $\leq 12\%$, showed superior degradation resistance during *in vitro* physiological immersion test conditions compared to the specimens with high pore interconnectivities.
- C) The fraction of surface open porosity directly affects the degradation rate of PM Mg-0.6Ca specimens. Specimens with 12% porosity showed a low pore interconnectivity, however, their degradation rate was 1.6 mm/year due to their surface open pore fraction of 45%. In specimens with porosities $\leq 10\%$ the degradation rates were < 0.3 mm/year with their open surface pore fraction maxing out at 33%.
- D) The decrease in the overall impurity surface oxide content on the pure magnesium powders after mechanical sieving treatment is determined to be the root cause for heterogeneous grain growth in PM Mg-0.6Ca specimens. This is prompted by a decrease in the effective grain boundary pinning area by the impurity oxides present in the magnesium matrix.
- E) The loss in degradation reproducibility due to the heterogeneous grain growth in PM Mg-0.6Ca specimens is attributed to the additional eutectic α -Mg + Mg₂Ca structures formed at certain grain boundaries. It is therefore concluded that PM Mg-0.6Ca materials with homogeneous grain structures and uniform grain sizes shall be preferred to ensure degradation reproducibility.
- F) The present work proved that the PM Mg-0.6Ca system is also flexible to the changes induced by sintering parameters and that the final mechanical properties can be tailored by the choice of sintering path. Combined with low *in vitro* degradation rates, it is apparent that the powder-based processing technique is a potential route for magnesium implant material fabrication.

Outlook

Stated below are some ideas for exploring the mechanisms occurring during powder metallurgy processing of Mg-Ca materials

- A) The present work revealed the feasibility of altering material microstructure by changing sintering temperature and by changing the nature of pure magnesium powders used for Mg-Ca powder mix preparation. However, the underlying sintering mechanism, despite the evident oxide particles in sintered microstructures, is not still clear. Due to the complex nature of the used sintering setup, timely tracking of sintering progress and therefore the grain growth is practically hindered. Due to the missing baseline for the surface oxide quantification on pure magnesium powders, any surface characterizing measurement on magnesium powders before and after sieving treatment will remain still qualitative. However, it is of importance to understand the nature of oxides, like hydroxides, carbon type or other impurity oxides that are adsorbed on pure magnesium surfaces after powder production technique. An XPS measurement might be useful to identify magnesium related compounds on powder surfaces.
- B) Because the Mg-0.6Ca system exhibited a good sintering response in the present work, it is beneficial to discern the degradation mechanism due to the influence of pores. The use of space holder particles of varying particle sizes/shapes might be useful to generate geometric pore shapes after sintering to assess degradation in dependence to pore channel diameters and pore volumes.
- C) To understand the behavior of calcium rich liquid phase during heterogeneous grain growth, time sequential sintering runs with subsequent quenching treatments are necessary. This facilitates the understanding for the formation of eutectic structures that are exclusively observed during heterogeneous grain growth in Mg-Ca system.

References

- [1] M. Pogorielov, E. Husak, A. Solodivnik, S. Zhdanov, Magnesium-based biodegradable alloys: Degradation, application, and alloying elements, *Interv Med Appl Sci* 9(1) (2017) 27-38.
- [2] J. Walker, S. Shadanbaz, T.B.F. Woodfield, M.P. Staiger, G.J. Dias, Magnesium biomaterials for orthopedic application: A review from a biological perspective, *Journal of Biomedical Materials Research Part B: Applied Biomaterials* 102(6) (2014) 1316-1331.
- [3] M. Razavi, M. Fathi, O. Savabi, M. Borouni, A review of degradation properties of Mg based biodegradable implants, *Research and Reviews in Materials Science and Chemistry* 1 (2012) 15-58.
- [4] J. Gonzalez, R.Q. Hou, E.P.S. Nidadavolu, R. Willumeit-Römer, F. Feyerabend, Magnesium degradation under physiological conditions – Best practice, *Bioactive Materials* 3(2) (2018) 174-185.
- [5] H.B. Yao, Y. Li, A.T.S. Wee, An XPS investigation of the oxidation/corrosion of melt-spun Mg, *Applied Surface Science* 158(1) (2000) 112-119.
- [6] M. Wolff, T. Ebel, M. Dahms, Sintering of Magnesium, *Advanced Engineering Materials* 12(9) (2010) 829-836.
- [7] J. Schaper, M. Wolff, B. Wiese, T. Ebel, R. Willumeit, Powder Metal Injection Moulding and Heat Treatment of AZ81 Mg Alloy, *Journal of Materials Processing Technology* 267 (2019) 241-246.
- [8] P. Burke, Investigation of the sintering fundamentals of Magnesium powders, Department of process engineering and applied science, Dalhousie University, 2011, p. 150.
- [9] M. Wolff, J.G. Schaper, M.R. Suckert, M. Dahms, F. Feyerabend, T. Ebel, R. Willumeit-Römer, T. Klassen, Metal Injection Molding (MIM) of Magnesium and Its Alloys, *Metals* 6(5) (2016) 118-130.
- [10] E.P.S. Nidadavolu, F. Feyerabend, T. Ebel, R. Willumeit-Römer, M. Dahms, Degradation behavior of as cast and powder metallurgy processed Mg-Ca alloys *Journal of Medical Materials and Technologies* 1(2) (2017) 18-21.
- [11] P.E. Nidadavolu, F. Feyerabend, T. Ebel, R. Willumeit-Römer, M. Dahms, On the Determination of Magnesium Degradation Rates under Physiological Conditions, *Materials* 9(8) (2016) 627-634.
- [12] M. Qian, G.B. Schaffer, C.J. Bettles, 13 - Sintering of titanium and its alloys, in: Z.Z. Fang (Ed.), *Sintering of Advanced Materials*, Woodhead Publishing 2010, pp. 324-355.
- [13] CompuTherm LLC, 2017. <http://www.computherm.com>, PandatTM 2017 with PanMagnesium 2017 database.
- [14] S. Dutta, K. Bavya Devi, M. Roy, Processing and degradation behavior of porous magnesium scaffold for biomedical applications, *Advanced Powder Technology* 28(12) (2017) 3204-3212.
- [15] J.-A. Kim, J. Lim, R. Naren, H.-s. Yun, E.K. Park, Effect of the biodegradation rate controlled by pore structures in magnesium phosphate ceramic scaffolds on bone tissue regeneration in vivo, *Acta Biomaterialia* 44 (2016) 155-167.
- [16] R.N. Lumley, T.B. Sercombe, G.M. Schaffer, Surface oxide and the role of magnesium during the sintering of aluminum, *Metallurgical and Materials Transactions A* 30(2) (1999) 457-463.
- [17] P. Burke, G. Kipouros, Powder metallurgy of magnesium: Is it feasible?, *Magnesium Technology* (2010) 115-120.

- [18] J. Li, G.J. Kipouros, P. Burke, C. Bibby, Investigation of Surface Film Formed on Fine Mg Particles, *Microscopy and Microanalysis* 15(S2) (2009) 362-363.
- [19] P.J. Burke, Z. Bayindir, G.J. Kipouros, X-ray Photoelectron Spectroscopy (XPS) Investigation of the Surface Film on Magnesium Powders, *Applied Spectroscopy* 66(5) (2012) 510-518.
- [20] M. Wolff, W. Limberg, T. Ebel, R. Bormann, Powder Injection Moulding: Towards Producing Magnesium Parts by Powder Metal Injection Moulding (MIM), *The European Powder Metallurgy Association, Shrewsbury, 2008*, pp. 221-226.
- [21] M. Wolff, T. Gülck, T. Ebel, Sintering of Mg and MgCa alloys for biomedical applications, *Proceedings of the Euro International Powder Metallurgy Congress and Exhibition, Euro PM 2009 2* (2009).
- [22] P. Burke, G. Kipouros, D. Fancelli, V. Laverdiere, Sintering Fundamentals of Magnesium Powders, *Canadian Metallurgical Quarterly* 48 (2009) 123-132.
- [23] P. Burke, C. Petit, S. Yakoubi, G. Kipouros, Thermal Effects of Calcium and Yttrium Additions on the Sintering of Magnesium Powder, *Magnesium Technology* (2011) 481-484.
- [24] P. Burke, C. Petit, S. Yakoubi, G. Kipouros, Thermal Effects of Calcium and Yttrium Additions on the Sintering of Magnesium Powder, 2011, pp. 481-484.
- [25] H. Halbach, N.D. Chatterjee, An internally consistent set of thermodynamic data for twentyone CaO-Al₂O₃-SiO₂- H₂O phases by linear parametric programming, *Contributions to Mineralogy and Petrology* 88(1) (1984) 14-23.
- [26] G.B. Schaffer, T.B. Sercombe, R.N. Lumley, Liquid phase sintering of aluminium alloys, *Materials Chemistry and Physics* 67(1) (2001) 85-91.
- [27] L. Zhang, X. Chen, C. Chen, X. Qu, Microstructure of Metal Injection Molded MIM418 Using Master Alloy Technique, in: S.J. Ikhmayies, B. Li, J.S. Carpenter, J.-Y. Hwang, S.N. Monteiro, J. Li, D. Firrao, M. Zhang, Z. Peng, J.P. Escobedo-Diaz, C. Bai (Eds.), *Characterization of Minerals, Metals, and Materials 2016*, Springer International Publishing, Cham, 2016, pp. 35-41.
- [28] D.F. Heaney, T.W. Mueller, P.A. Davies, Mechanical properties of metal injection moulded 316L stainless steel using both prealloy and master alloy techniques, *Powder Metallurgy* 47(4) (2004) 367-373.
- [29] R. de Oro Calderon, E. Bernardo, M. Campos, C. Gierl-Mayer, H. Danninger, J.M. Torralba, Master alloys for liquid phase sintering: Some key points for the design, *Metal Powder Report* 71(3) (2016) 184-192.
- [30] E. Nidadavolu, Degradation behavior of as cast and powder metallurgy processed Mg-Ca alloys, *Material Science and Engineering*, University of Kiel, 2016.
- [31] M. Wolff, J.G. Schaper, M. Dahms, T. Ebel, K.U. Kainer, T. Klassen, Magnesium powder injection moulding for biomedical application, *Powder Metallurgy* 57(5) (2014) 331-340.
- [32] M. Wolff, T. Glück, T. Ebel, Sintering of Mg and Mg-Ca alloys for biomedical applications, *EURO PM 2009, EURO PM, 2009*, p. 417.
- [33] G.M. Randall, M. S.S., Sintering time and atmosphere influences on the microstructure and mechanical properties of Tungsten heavy alloys., *Metallurgical transactions A* 23(1) (1992) 211-219.
- [34] M. Momeni, C. Gierl, H. Danninger, Study of the oxide reduction and interstitial contents during sintering of different plain carbon steels by in situ mass spectrometry in nitrogen atmosphere, *Materials Chemistry and Physics* 129(1) (2011) 209-216.
- [35] J.G. Schaper, Magnesium Polyolefin Interactions during Thermal Debinding in the MIM Process of Magnesium, *Materialwissenschaft, University of Kiel, Kiel, 2019*.

- [36] J. Schaper, M. Wolff, T. Ebel, R. Willumeit, Sintering of Mg and its alloys under Hydrogen Atmospheres, Euro PM2018, Bilbao, Spain, 2018.
- [37] Y. Huang, L. Yang, S. You, W. Gan, K.U. Kainer, N. Hort, Unexpected formation of hydrides in heavy rare earth containing magnesium alloys, *Journal of Magnesium and Alloys* 4(3) (2016) 173-180.
- [38] M. Wolff, J.G. Schaper, M.R. Suckert, M. Dahms, T. Ebel, R. Willumeit-Römer, T. Klassen, Magnesium Powder Injection Molding (MIM) of Orthopedic Implants for Biomedical Applications, *JOM* 68(4) (2016) 1191-1197.
- [39] R.M. German, P. Suri, S.J. Park, Review: liquid phase sintering, *Journal of Materials Science* 44(1) (2009) 1-39.
- [40] R.M. German, Phase Diagrams in Liquid Phase Sintering Treatments, *JOM* 38(8) (1986) 26-29.
- [41] L. Dejonghe, M. Rahaman, 4.1 Sintering of Ceramics, 2003, pp. 187-264.
- [42] R.M. German, Intermediate Stage Processes: Solution-Reprecipitation, Liquid Phase Sintering, Springer US, Boston, MA, 1985, pp. 101-126.
- [43] J. Liu, R.M. German, Rearrangement densification in liquid-phase sintering, *Metallurgical and Materials Transactions A* 32(12) (2001) 3125-3131.
- [44] O.-H. Kwon, G.L. Messing, Kinetic Analysis of Solution-Precipitation During Liquid-Phase Sintering of Alumina, *Journal of the American Ceramic Society* 73(2) (1990) 275-281.
- [45] J.-K. Park, S.-J.L. Kang, K.Y. Eun, D.N. Yoon, Microstructural change during liquid phase sintering of W-Ni-Fe alloy, *Metallurgical Transactions A* 20(5) (1989) 837-845.
- [46] W. Dong, H. Jain, M.P. Harmer, Liquid Phase Sintering of Alumina, I. Microstructure Evolution and Densification, *Journal of the American Ceramic Society* 88(7) (2005) 1702-1707.
- [47] E. Salahinejad, R. Amini, M. Marasi, M.J. Hadianfard, The effect of sintering time on the densification and mechanical properties of a mechanically alloyed Cr-Mn-N stainless steel, *Materials & Design* 31(1) (2010) 527-532.
- [48] N.M. Hwang, Y.J. Park, D.Y. Kim, D.Y. Yoon, Activated sintering of nickel-doped tungsten: approach by grain boundary structural transition, *Scripta Materialia* 42(5) (2000) 421-425.
- [49] E. Aghion, Y. Perez, Effects of porosity on corrosion resistance of Mg alloy foam produced by powder metallurgy technology, *Materials Characterization* 96 (2014) 78-83.
- [50] J. Čapek, D. Vojtěch, Effect of sintering conditions on the microstructural and mechanical characteristics of porous magnesium materials prepared by powder metallurgy, *Materials Science and Engineering: C* 35 (2014) 21-28.
- [51] N.C. Kothari, Grain Growth during Sintering of Tungsten, *Journal of Applied Physics* 38(5) (1967) 2395-2396.
- [52] R.M. German, Coarsening in Sintering: Grain Shape Distribution, Grain Size Distribution, and Grain Growth Kinetics in Solid-Pore Systems, *Critical Reviews in Solid State and Materials Sciences* 35(4) (2010) 263-305.
- [53] K.S. Venkataraman, R.A. DiMilia, Predicting the Grain-Size Distributions in High-Density, High-Purity Alumina Ceramics, *Journal of the American Ceramic Society* 72(1) (1989) 33-39.
- [54] M. Shirdel, H. Mirzadeh, M. Habibi Parsa, Microstructural Evolution During Normal/Abnormal Grain Growth in Austenitic Stainless Steel, *Metallurgical and Materials Transactions A* 45(11) (2014) 5185-5193.

- [55] J. Janis, K. Nakajima, A. Karasev, H. Shibata, P.G. Jönsson, An experimental study on the influence of particles on grain boundary migration, *Journal of Materials Science* 45(8) (2010) 2233-2238.
- [56] V. Kumar, Z.Z. Fang, S.I. Wright, M.M. Nowell, An analysis of grain boundaries and grain growth in cemented tungsten carbide using orientation imaging microscopy, *Metallurgical and Materials Transactions A* 37(3) (2006) 599-607.
- [57] J. Bruno, P.R. Rios, The grain size distribution and the detection of abnormal grain growth of austenite in an eutectoid steel containing niobium, *Scripta Metallurgica et Materialia* 32(4) (1995) 601-606.
- [58] E.A. Holm, T.D. Hoffmann, A.D. Rollett, C.G. Roberts, Particle-assisted abnormal grain growth, *IOP Conference Series: Materials Science and Engineering* 89 (2015) 012005.
- [59] H.-Y. Kim, J.-A. Lee, J.-J. Kim, Densification Behaviors of Fine-Alumina and Coarse-Alumina Compacts during Liquid-Phase Sintering with the Addition of Talc, *Journal of the American Ceramic Society* 83(12) (2000) 3128-3134.
- [60] B.K. Yoon, B.-A. Lee, S.-J. Kang, Growth Behavior of Rounded (Ti,W)C and Faceted WC Grains in a Co Matrix during Liquid Phase Sintering, *Acta Materialia* 53 (2005) 4677-4685.
- [61] P.R. Rios, D. Zöllner, Critical assessment 30: Grain growth – Unresolved issues, *Materials Science and Technology* 34(6) (2018) 629-638.
- [62] I. MacLaren, R.M. Cannon, M.A. Gülgün, R. Voytovych, N. Popescu-Pogrion, C. Scheu, U. Täffner, M. Rühle, Abnormal Grain Growth in Alumina: Synergistic Effects of Yttria and Silica, *Journal of the American Ceramic Society* 86(4) (2003) 650-59.
- [63] H.-Y. Lee, R. Freer, Abnormal grain growth and liquid-phase sintering in Sr_{0.6}Ba_{0.4}Nb₂O₆ (SBN40) ceramics, *Journal of Materials Science* 33(7) (1998) 1703-1708.
- [64] I.-J. Bae, S. Baik, Abnormal Grain Growth of Alumina, *Journal of the American Ceramic Society* 80(5) (1997) 1149-1156.
- [65] J. Jung, S. Baik, Abnormal Grain Growth of Alumina: CaO Effect, *Journal of the American Ceramic Society* 86(4) (2003) 644-49.
- [66] A.J. Rayner, S.F. Corbin, Grain growth activation during supersolidus liquid phase sintering in a metal injection molded nickel-base superalloy, *Materials Today Communications* (2020) 101769.
- [67] D. Zhao, F. Witte, F. Lu, J. Wang, J. Li, L. Qin, Current status on clinical applications of magnesium-based orthopaedic implants: A review from clinical translational perspective, *Biomaterials* 112 (2017) 287-302.
- [68] J.A. Cowan, Structural and catalytic chemistry of magnesium-dependent enzymes, *Biometals* 15(3) (2002) 225-235.
- [69] S. Wallach, Availability of body magnesium during magnesium deficiency, *Magnesium* 7(5-6) (1988) 262-70.
- [70] I.o. Medicine, Dietary Reference Intakes for Calcium, Phosphorus, Magnesium, Vitamin D, and Fluoride, The National Academies Press, Washington, DC, 1997.
- [71] I. Almeida Paz, L. Bruno, Bone mineral density: review, *Brazilian Journal of Poultry Science* 8 (2006) 69-73.
- [72] S.E. Harandi, M. Mirshahi, S. Koleini, M.H. Idris, H. Jafari, M.R.A. Kadir, Effect of calcium content on the microstructure, hardness and in-vitro corrosion behavior of biodegradable Mg-Ca binary alloy, *Materials Research* 16 (2013) 11-18.
- [73] N. Kirkland, N. Birbilis, J. Walker, T. Woodfield, G. Dias, M. Staiger, In-vitro dissolution of magnesium-calcium binary alloys: Clarifying the unique role of calcium additions in

- bioresorbable magnesium implant alloys, *Journal of biomedical materials research. Part B, Applied biomaterials* 95(1) (2010) 91-100.
- [74] N. Birbilis, K.D. Ralston, S. Virtanen, H.L. Fraser, C.H.J. Davies, Grain character influences on corrosion of ECAPed pure magnesium, *Corrosion Engineering, Science and Technology* 45(3) (2010) 224-230.
- [75] H.R.B. Rad, M.H. Idris, M.R.A. Kadir, S. Farahany, Microstructure analysis and corrosion behavior of biodegradable Mg–Ca implant alloys, *Materials & Design* 33 (2012) 88-97.
- [76] F. Locatelli, D. Fouque, O. Heimbürger, T.B. Drüeke, J.B. Cannata-Andía, W.H. Hörl, E. Ritz, Nutritional status in dialysis patients: a European consensus, *Nephrology Dialysis Transplantation* 17(4) (2002) 563-572.
- [77] Z. Li, X. Gu, S. Lou, Y. Zheng, The development of binary Mg–Ca alloys for use as biodegradable materials within bone, *Biomaterials* 29(10) (2008) 1329-1344.
- [78] Y.-F. Ding, C. Wen, P. Hodgson, Y. Li, Effects of alloying elements on the corrosion behavior and biocompatibility of biodegradable magnesium alloys: A review, *J. Mater. Chem. B* 2 (2014).
- [79] A. Mohamed, A.M. El-Aziz, H.-G. Breiterger, Study of the degradation behavior and the biocompatibility of Mg–0.8Ca alloy for orthopedic implant applications, *Journal of Magnesium and Alloys* 7(2) (2019) 249-257.
- [80] Y. Liu, X. Liu, Z. Zhang, N. Farrell, D. Chen, Y. Zheng, Comparative, real-time in situ monitoring of galvanic corrosion in Mg-Mg₂Ca and Mg-MgZn₂ couples in Hank's solution, *Corrosion Science* 161 (2019) 108185.
- [81] R.-Q. Hou, C.-Q. Ye, C.-D. Chen, S.-G. Dong, M.-Q. Lv, S. Zhang, J.-S. Pan, G.-L. Song, C.-J. Lin, Localized Corrosion of Binary Mg–Ca Alloy in 0.9 wt% Sodium Chloride Solution, *Acta Metallurgica Sinica (English Letters)* 29(1) (2016) 46-57.
- [82] A. Drynda, T. Hassel, R. Hoehn, A. Perz, F.-W. Bach, M. Peuster, Development and biocompatibility of a novel corrodible fluoride-coated magnesium-calcium alloy with improved degradation kinetics and adequate mechanical properties for cardiovascular applications, *J Biomed Mater Res A* 93(2) (2010) 763-775.
- [83] Y. Wan, G. Xiong, H. Luo, F. He, Y. Huang, X. Zhou, Preparation and characterization of a new biomedical magnesium–calcium alloy, *Materials & Design* 29(10) (2008) 2034-2037.
- [84] M. Deng, L. Wang, D. Höche, S.V. Lamaka, C. Wang, D. Snihirova, Y. Jin, Y. Zhang, M.L. Zheludkevich, Approaching “stainless magnesium” by Ca micro-alloying, *Materials Horizons* (2020).
- [85] A. Atrens, G.-L. Song, M. Liu, Z. Shi, F. Cao, M.S. Dargusch, Review of Recent Developments in the Field of Magnesium Corrosion, *Advanced Engineering Materials* 17(4) (2015) 400-453.
- [86] G. Song, A. Atrens, Understanding Magnesium Corrosion—A Framework for Improved Alloy Performance, *Advanced Engineering Materials* 5(12) (2003) 837-858.
- [87] T. Cain, L.G. Bland, N. Birbilis, J.R. Scully, A Compilation of Corrosion Potentials for Magnesium Alloys, *Corrosion* 70(10) (2014) 1043-1051.
- [88] G.L. Song, 1 - Corrosion behavior and prevention strategies for magnesium (Mg) alloys, in: G.-L. Song (Ed.), *Corrosion Prevention of Magnesium Alloys*, Woodhead Publishing 2013, pp. 3-37.
- [89] M. Esmaily, J.E. Svensson, S. Fajardo, N. Birbilis, G.S. Frankel, S. Virtanen, R. Arrabal, S. Thomas, L.G. Johansson, Fundamentals and advances in magnesium alloy corrosion, *Progress in Materials Science* 89 (2017) 92-193.

- [90] J.D. Hanawalt, C.E. Nelson, J.A. Peloubet, Corrosion Studies Of Magnesium And Its Alloys, The American Institute of Mining, Metallurgical, and Petroleum Engineers, 1941.
- [91] F. Witte, N. Hort, C. Vogt, S. Cohen, K.U. Kainer, R. Willumeit, F. Feyerabend, Degradable biomaterials based on magnesium corrosion, *Current Opinion in Solid State and Materials Science* 12(5) (2008) 63-72.
- [92] R. Willumeit, J. Fischer, F. Feyerabend, N. Hort, U. Bismayer, S. Heidrich, B. Mihailova, Chemical surface alteration of biodegradable magnesium exposed to corrosion media, *Acta Biomaterialia* 7(6) (2011) 2704-2715.
- [93] D. Tie, F. Feyerabend, N. Hort, R. Willumeit, D. Hoeche, XPS Studies of Magnesium Surfaces after Exposure to Dulbecco's Modified Eagle Medium, Hank's Buffered Salt Solution, and Simulated Body Fluid, *Advanced Engineering Materials* 12(12) (2010) B699-B704.
- [94] A. Yamamoto, S. Hiromoto, Effect of inorganic salts, amino acids and proteins on the degradation of pure magnesium in vitro, *Materials Science and Engineering: C* 29(5) (2009) 1559-1568.
- [95] R. Hou, F. Feyerabend, R. Willumeit, Proteins and Medium Flow Conditions: How They Influence the Degradation of Magnesium, *Surface Innovations* 8 (2019) 1-10.
- [96] A. International, Standard Guide for Laboratory Immersion Corrosion Testing of Metals, ASTM NACE / ASTM G31-12a, West Conshohocken, PA, 2012, p. 10.
- [97] G. Jia, C. Chen, J. Zhang, W. Yinchuan, Y. Rui, B. Luthringer, R. Willumeit, H. Zhang, M. Xiong, H. Huang, G. Yuan, F. Feyerabend, In vitro degradation behavior of Mg scaffolds with three-dimensional interconnected porous structures for bone tissue engineering, *Corrosion Science* 144 (2018) 301-312.
- [98] C. Ning, L. Zhou, Y. Zhu, Y. Li, P. Yu, S. Wang, T. He, W. Li, G. Tan, Y. Wang, C. Mao, Influence of Surrounding Cations on the Surface Degradation of Magnesium Alloy Implants under a Compressive Pressure, *Langmuir* 31(50) (2015) 13561-13570.
- [99] M. Dahms, D. Höche, N. Ahmad Agha, F. Feyerabend, R. Willumeit-Römer, A simple model for long-time degradation of magnesium under physiological conditions, *Materials and Corrosion* 69(2) (2018) 191-196.
- [100] B.A. Shaw, ASM Handbook, Volume 13A Corrosion: Fundamentals, Testing and Protection, ASM International 2003.
- [101] J.D. Hanawalt, C. Nelson, J.A. Peloubet, Transactions of the American Institute of Mining and Metallurgical Engineers. Corrosion studies of magnesium and its alloys, Philadelphia: Institute of Metals Division, 1942.
- [102] A. Atrens, G. Ling Song, Review: Corrosion Mechanisms of Magnesium alloys, *Advanced Engineering Materials*, No. 1 (1999).
- [103] D. Höche, C. Blawert, S.V. Lamaka, N. Scharnagl, C. Mendis, M.L. Zheludkevich, The effect of iron re-deposition on the corrosion of impurity-containing magnesium, *Physical Chemistry Chemical Physics* 18(2) (2016) 1279-1291.
- [104] C. Blawert, D. Fechner, D. Höche, V. Heitmann, W. Dietzel, K.U. Kainer, P. Zivanovic, C. Scharf, A. Ditze, J. Gröbner, R. Schmid-Fetzer, Magnesium secondary alloys: Alloy design for magnesium alloys with improved tolerance limits against impurities., *Corrosion Science* 52(7) (2010) 2452-2468.
- [105] M. Liu, G.-L. Song, Impurity control and corrosion resistance of magnesium–aluminum alloy, *Corrosion Science* 77 (2013) 143-150.
- [106] D.S. Tawil, Proc. Conf. Magnesium Technology, Institute of Metals, London, 1987, pp. 66-74.

- [107] J.E. Hillis, S.O. Shook, Composition and performance of an improved Magnesium AS41 alloy, SAE Technical paper series #890 (1989) 205.
- [108] W.E. Mercer II, J.E. Hillis, The critical contaminant limits and salt water corrosion performance of Magnesium AE42 alloy, SAE Technical paper series # 920 (1992).
- [109] J. Kim, H.N. Nguyen, B.S. You, Y. Kim, Effect of Y addition on removal of Fe impurity from magnesium alloys, *Scripta Materialia* 162 (2019) 355-360.
- [110] G.L. Makar, J. Kruger, Corrosion of magnesium, *International Materials Reviews* 38(3) (1993) 138-153.
- [111] I. Marco, A. Myrissa, E. Martinelli, F. Feyerabend, R. Willumeit-Römer, A.M. Weinberg, O. Van der Biest, In vivo and in vitro degradation comparison of pure Mg, Mg-10Gd and Mg-2Ag: a short term study, *European cells & materials* 33 (2017) 90-104.
- [112] Y. Dai, X. Chen, T. Yan, A. Tang, D. Zhao, Z. Luo, C.-q. Liu, R. Cheng, F. Pan, Improved Corrosion Resistance in AZ61 Magnesium Alloys Induced by Impurity Reduction, *Acta Metallurgica Sinica (English Letters)* 33 (2019) 225-232.
- [113] H. Matsubara, Y. Ichige, K. Fujita, H. Nishiyama, K. Hodouchi, Effect of impurity Fe on corrosion behavior of AM50 and AM60 magnesium alloys, *Corrosion Science* 66 (2013) 203-210.
- [114] J. Harmuth, B. Wiese, J. Bohlen, T. Ebel, R. Willumeit-Römer, Wide Range Mechanical Customization of Mg-Gd Alloys With Low Degradation Rates by Extrusion, *Frontiers in Materials* 6(201) (2019).
- [115] J. Kubásek, D. Vojtěch, Structural and corrosion characterization of biodegradable Mg-RE (RE=Gd, Y, Nd) alloys, *Transactions of Nonferrous Metals Society of China* 23(5) (2013) 1215-1225.
- [116] G. Ben-Hamu, D. Eliezer, K.S. Shin, The role of Si and Ca on new wrought Mg-Zn-Mn based alloy, *Materials Science and Engineering: A* 447(1) (2007) 35-43.
- [117] Y. Jin, C. Blawert, F. Feyerabend, J. Bohlen, M. Silva Campos, S. Gavras, B. Wiese, D. Mei, M. Deng, H. Yang, R. Willumeit-Römer, Time-sequential corrosion behaviour observation of micro-alloyed Mg-0.5Zn-0.2Ca alloy via a quasi-in situ approach, *Corrosion Science* 158 (2019) 108096.
- [118] Y. Jin, C. Blawert, H. Yang, B. Wiese, F. Feyerabend, J. Bohlen, D. Mei, M. Deng, M.d.R. Silva Campos, N. Scharnagl, K. Strecker, J. Bode, C. Vogt, R. Willumeit, Microstructure-corrosion behaviour relationship of micro-alloyed Mg-0.5Zn alloy with the addition of Ca, Sr, Ag, In and Cu, *Materials & design* 195 (2020) 108980.
- [119] Y.G. Na, D. Eliezer, K.S. Shin, Corrosion of new wrought magnesium alloys, *Materials Science Forum*, 2005, pp. 839-844.
- [120] A.D. Südholz, N.T. Kirkland, R.G. Buchheit, N. Birbilis, Electrochemical Properties of Intermetallic Phases and Common Impurity Elements in Magnesium Alloys, *Electrochemical and Solid-State Letters* 14(2) (2011) C5.
- [121] L. Yang, G. Liu, L. Ma, E. Zhang, X. Zhou, G. Thompson, Effect of iron content on the corrosion of pure magnesium: Critical factor for iron tolerance limit, *Corrosion Science* 139 (2018) 421-429.
- [122] S. Li, P. Wu, W. Zhou, T. Ando, Kinetics of heterogeneous nucleation of gas-atomized Sn-5mass%Pb droplets, *Materials Science and Engineering: A* 473(1) (2008) 206-212.
- [123] C. Song, K. Li, K. Xie, W. Lu, S. Zhao, Q. Han, Q. Zhai, The effect of the nucleation ability on solidified microstructures of gas-atomized Fe-6.5wt.%Si alloy powder, *Powder Technology* 263 (2014) 31-36.

- [124] F. Nilsén, I. Aaltio, Y. Ge, T. Lindroos, S.P. Hannula, Characterization of Gas Atomized Ni-Mn-Ga Powders, *Materials Today: Proceedings* 2 (2015) S879-S882.
- [125] J. Čapek, D. Vojtěch, Properties of porous magnesium prepared by powder metallurgy, *Materials Science and Engineering: C* 33(1) (2013) 564-569.
- [126] C.E. Wen, Y. Yamada, K. Shimojima, Y. Chino, H. Hosokawa, M. Mabuchi, Compressibility of porous magnesium foam: dependency on porosity and pore size, *Materials Letters* 58(3) (2004) 357-360.
- [127] Y. Bi, Y. Zheng, Y. Li, Microstructure and mechanical properties of sintered porous magnesium using polymethyl methacrylate as the space holder, *Materials Letters* 161 (2015) 583-586.
- [128] S.F. Aida, H. Zuhailawati, A.S. Anasyida, The Effect of Space Holder Content and Sintering Temperature of Magnesium Foam on Microstructural and Properties Prepared by Sintering Dissolution Process (SDP) Using Carbamide Space Holder, *Procedia Engineering* 184 (2017) 290-297.
- [129] M. Wolff, M. Luczak, J.G. Schaper, B. Wiese, M. Dahms, T. Ebel, R. Willumeit-Römer, T. Klassen, In vitro biodegradation testing of Mg-alloy EZK400 and manufacturing of implant prototypes using PM (powder metallurgy) methods, *Bioactive Materials* 3(3) (2018) 213-217.
- [130] J. Dong, Y. Li, P. Lin, M.A. Leeflang, S. van Asperen, K. Yu, N. Tümer, B. Norder, A.A. Zadpoor, J. Zhou, Solvent-cast 3D printing of magnesium scaffolds, *Acta Biomaterialia* 114 (2020) 497-514.
- [131] X. Zhang, X.-W. Li, J.-G. Li, X.-D. Sun, Preparation and mechanical property of a novel 3D porous magnesium scaffold for bone tissue engineering, *Materials Science and Engineering: C* 42 (2014) 362-367.
- [132] F. Witte, H. Ulrich, M. Rudert, E. Willbold, Biodegradable magnesium scaffolds: Part 1: Appropriate inflammatory response, *Journal of Biomedical Materials Research Part A* 81A(3) (2007) 748-756.
- [133] A.H. Aghajanian, B.A. Khazaei, M. Khodaei, M. Rafienia, Fabrication of Porous Mg-Zn Scaffold through Modified Replica Method for Bone Tissue Engineering, *Journal of Bionic Engineering* 15(5) (2018) 907-913.
- [134] P. Burke, Z. Bayindir, G. Kipouros, X-ray Photoelectron Spectroscopy (XPS) Investigation of the Surface Film on Magnesium Powders, *Applied spectroscopy* 66 (2012) 510-8.
- [135] T. Neu, M. Mukherjee, F. García-Moreno, J. Banhart, Magnesium and magnesium alloy foams [C], *Porous Metals and Metallic Foams* (2011) 133-140.
- [136] K. Bobe, E. Willbold, I. Morgenthal, O. Andersen, T. Studnitzky, J. Nellesen, W. Tillmann, C. Vogt, K. Vano, F. Witte, In vitro and in vivo evaluation of biodegradable, open-porous scaffolds made of sintered magnesium W4 short fibres, *Acta Biomaterialia* 9(10) (2013) 8611-8623.
- [137] M.-H. Kang, H.-D. Jung, S.-W. Kim, S.-M. Lee, H.-E. Kim, Y. Estrin, Y.-H. Koh, Production and bio-corrosion resistance of porous magnesium with hydroxyapatite coating for biomedical applications, *Materials Letters* 108 (2013) 122-124.
- [138] X. Zhang, X.W. Li, J.G. Li, X.D. Sun, Preparation and Mechanical Properties of a Novel Biomedical Magnesium-Based Scaffold, *Key Engineering Materials* 544 (2013) 276-280.
- [139] F. Geng, L. Tan, B. Zhang, C. Wu, Y. He, J. Yang, K. Yang, Study on β -TCP Coated Porous Mg as a Bone Tissue Engineering Scaffold Material, *J. Mater. Sci. Technol* 25 (2009).

- [140] X.N. Gu, W.R. Zhou, Y.F. Zheng, Y. Liu, Y.X. Li, Degradation and cytotoxicity of lotus-type porous pure magnesium as potential tissue engineering scaffold material, *Materials Letters* 64(17) (2010) 1871-1874.
- [141] T. Nguyen, M. Staiger, G. Dias, T. Woodfield, A Novel Manufacturing Route for Fabrication of Topologically-Ordered Porous Magnesium Scaffolds, *Advanced Engineering Materials* 13 (2011) 872-881.
- [142] H. Zhuang, Y. Han, A. Feng, Preparation, mechanical properties and in vitro biodegradation of porous magnesium scaffolds, *Materials Science and Engineering: C* 28 (2008) 1462-1466.
- [143] N. Zou, Q. Li, Mechanical Properties of Lightweight Porous Magnesium Processed Through Powder Metallurgy, *JOM* 70(5) (2018) 650-655.
- [144] B. WANG, K. LI, Y. ZHANG, B. YAN, W. LU, CHARACTERIZATION OF POROUS Mg-Zn ALLOY USING X-RAY TOMOGRAPHY AND ITS DRUG-LOADING BEHAVIOR, *Modern Physics Letters B* 27(19) (2013) 1341009.
- [145] M. Yazdimamaghani, M. Razavi, D. Vashaei, L. Tayebi, Surface modification of biodegradable porous Mg bone scaffold using polycaprolactone/bioactive glass composite, *Materials Science and Engineering: C* 49 (2015) 436-444.
- [146] A.H.M. Sanchez, B.J.C. Luthringer, F. Feyerabend, R. Willumeit, Mg and Mg alloys: How comparable are in vitro and in vivo corrosion rates? A review, *Acta Biomaterialia* 13 (2015) 16-31.
- [147] A. Juliawati, W.S.W. Harun, M.A. Hassan, A Review on the Preparation of Magnesium-Based Alloys Prepared by Powder Metallurgy and the Evolution of Microstructure and Mechanical Properties, *Key Engineering Materials* 796 (2019) 3-10.
- [148] G.R. Argade, S.K. Panigrahi, R.S. Mishra, Effects of grain size on the corrosion resistance of wrought magnesium alloys containing neodymium, *Corrosion Science* 58 (2012) 145-151.
- [149] K.D. Ralston, N. Birbilis, Effect of Grain Size on Corrosion: A Review, *Corrosion* 66(7) (2010) 075005-075005-13.
- [150] H.S. Kim, W.J. Kim, Enhanced corrosion resistance of ultrafine-grained AZ61 alloy containing very fine particles of Mg₁₇Al₁₂ phase, *Corrosion Science* 75 (2013) 228-238.
- [151] S. Izumi, M. Yamasaki, Y. Kawamura, Relation between corrosion behavior and microstructure of Mg-Zn-Y alloys prepared by rapid solidification at various cooling rates, *Corrosion Science* 51(2) (2009) 395-402.
- [152] Y. Xiyu, J. Tang, Y. Zhou, A. Atrens, M. Dargusch, B. Wiese, T. Ebel, M. Yan, Surface modification of biomedical Mg-Ca and Mg-Zn-Ca alloys using selective laser melting: corrosion behaviour, microhardness and biocompatibility, *Journal of Magnesium and Alloys* (2020) 1-14.
- [153] P. Minárik, R. Král, M. Janeček, Effect of ECAP processing on corrosion resistance of AE21 and AE42 magnesium alloys, *Applied Surface Science* 281 (2013) 44-48.
- [154] H. Wang, Y. Estrin, Z. Zúberová, Bio-corrosion of a magnesium alloy with different processing histories, *Materials Letters* 62(16) (2008) 2476-2479.
- [155] Y. Lu, A.R. Bradshaw, Y.L. Chiu, I.P. Jones, Effects of secondary phase and grain size on the corrosion of biodegradable Mg-Zn-Ca alloys, *Materials Science and Engineering: C* 48 (2015) 480-486.
- [156] N. Saikrishna, G. Pradeep Kumar Reddy, B. Munirathinam, B. Ratna Sunil, Influence of bimodal grain size distribution on the corrosion behavior of friction stir processed biodegradable AZ31 magnesium alloy, *Journal of Magnesium and Alloys* 4(1) (2016) 68-76.

- [157] D. Song, A. Ma, J. Jiang, P. Lin, D. Yang, J. Fan, Corrosion behavior of equal-channel-angular-pressed pure magnesium in NaCl aqueous solution, *Corrosion Science* 52(2) (2010) 481-490.
- [158] T. Elemental, AAS, GFAAS, ICP or ICP-MS ? Which technique should I use? An elementary overview of elemental analysis., Thermo Fischer Scientific, USA.
- [159] R.D. Beaty, J.D. Kerber, Concepts , Instrumentation and Techniques in Atomic Absorption Spectrophotometry, 1997.
- [160] S. LAB, Stationary metal analyzers. <https://www.spectro.com/products/optical-emission-spectroscopy/arc-spark-stationary-oes-working-principle>.
- [161] S. Global, Analytical and measuring instruments. <https://www.shimadzu.com/an/products/elemental-analysis/oes-app/principle-of-optical-emission-spectrometry/index.html>.
- [162] J. Schindelin, I. Arganda-Carreras, E. Frise, V. Kaynig, M. Longair, T. Pietzsch, S. Preibisch, C. Rueden, S. Saalfeld, B. Schmid, J.-Y. Tinevez, D.J. White, V. Hartenstein, K. Eliceiri, P. Tomancak, A. Cardona, Fiji: an open-source platform for biological-image analysis, *Nature Methods* 9(7) (2012) 676-682.
- [163] J.D. Boerckel, D.E. Mason, A.M. McDermott, E. Alsberg, Microcomputed tomography: approaches and applications in bioengineering, *Stem Cell Res Ther* 5(6) (2014) 144-144.
- [164] K. Heim, F. Bernier, R. Pelletier, L.P. Lefebvre, High resolution pore size analysis in metallic powders by X-ray tomography, *Case Studies in Nondestructive Testing and Evaluation* 6 (2016) 45-52.
- [165] S.C. T.W. Ridler, Picture Thresholding Using an Iterative Selection Method, *IEEE Transactions on Systems, Man, and Cybernetics* 8(8) (1978) 630-632.
- [166] S. Bolte, F.P. Cordelieres, A guided tour into subcellular colocalization analysis in light microscopy, *Journal of microscopy* 224(3) (2006) 213-232.
- [167] N.C.W. Kuijpers, J. Tirel, D.N. Hanlon, S. van der Zwaag, Quantification of the evolution of the 3D intermetallic structure in a 6005A aluminium alloy during a homogenisation treatment, *Materials Characterization* 48(5) (2002) 379-392.
- [168] D. Tolnai, P. Townsend, G. Requena, L. Salvo, J. Lendvai, H.P. Degischer, In situ synchrotron tomographic investigation of the solidification of an AlMg4.7Si8 alloy, *Acta Materialia* 60(6) (2012) 2568-2577.
- [169] J.-K. Lee, S.K. Kim, Effect of CaO composition on oxidation and burning behaviors of AM50 Mg alloy, *Transactions of Nonferrous Metals Society of China* 21 (2011) s23-s27.
- [170] L.C. Lim, P.M. Wong, M. Jan, Microstructural evolution during sintering of near-monosized agglomerate-free submicron alumina powder compacts, *Acta Materialia* 48(9) (2000) 2263-2275.
- [171] W.D. KINGERY, E. NIKI, M.D. NARASIMHAN, Sintering of Oxide and Carbide-Metal Compositions in Presence of a Liquid Phase, *Journal of the American Ceramic Society* 44(1) (1961) 29-35.
- [172] S.-H. Ha, J.-K. Lee, S.K. Kim, Effect of CaO on Oxidation Resistance and Microstructure of Pure Mg, *Materials Transactions - MATER TRANS* 49 (2008) 1081-1083.
- [173] F. Czerwinski, Oxidation Characteristics of Magnesium Alloys, *JOM* 64(12) (2012) 1477-1483.
- [174] M.M. Jalilvand, M. Akbarifar, M. Divandari, H. Saghafian, On the dynamically formed oxide films in molten Mg, *Journal of Magnesium and Alloys* 8(1) (2020) 219-230.

- [175] A. Bachmaier, R. Pippan, Effect of oxide particles on the stabilization and final microstructure in aluminium, *Materials Science and Engineering: A* 528(25) (2011) 7589-7595.
- [176] S.-J. Cho, S.-J.L. Kang, D.N. Yoon, Effect of entrapped inert gas on pore filling during liquid phase sintering, *Metallurgical Transactions A* 17(12) (1986) 2175-2182.
- [177] R.J. Low, I.M. Robertson, G.B. Schaffer, Excessive porosity after liquid-phase sintering of elemental titanium powder blends, *Scripta Materialia* 56(10) (2007) 895-898.
- [178] R.M. German, Supersolidus liquid-phase sintering of prealloyed powders, *Metallurgical and Materials Transactions A* 28(7) (1997) 1553-1567.
- [179] P.F. Murley, R.M. German, *Advances in Powder Metallurgy*, Metal Powder Industries Federation, Princeton, NJ, 1989, pp. 103-120.
- [180] R. Tandon, Y. Liu, R.M. German, Role of Initial Powder Characteristics in Supersolidus Liquid Phase Sintering, *Advances in powder metallurgy and particulate materials* 3 (1994) 251-266.
- [181] C.J. Kong, P.D. Brown, S.J. Harris, D.G. McCartney, Analysis of microstructure formation in gas-atomised Al–12wt.% Sn–1wt.% Cu alloy powder, *Materials Science and Engineering: A* 454-455 (2007) 252-259.
- [182] L. Sang, Y. Xu, P. Fang, H. Zhang, Y. Cai, X. Liu, The influence of cooling rate on the microstructure and phase fraction of gas atomized NiAl₃ alloy powders during rapid solidification, *Vacuum* 157 (2018) 354-360.
- [183] P. Shukla, R.K. Mandal, S.N. Ojha, Non-equilibrium solidification of undercooled droplets during atomization process, *Bulletin of Materials Science* 24(5) (2001) 547-554.
- [184] J.H. Perepezko, M.J. Uttormark, Undercooling and Nucleation during Solidification, *ISIJ International* 35(6) (1995) 580-588.
- [185] R. Hou, R. Willumeit-Römer, V.M. Garamus, M. Frant, J. Koll, F. Feyerabend, Adsorption of Proteins on Degradable Magnesium—Which Factors are Relevant?, *ACS Applied Materials & Interfaces* 10(49) (2018) 42175-42185.
- [186] I. Johnson, H. Liu, A Study on Factors Affecting the Degradation of Magnesium and a Magnesium-Yttrium Alloy for Biomedical Applications, *PLOS ONE* 8(6) (2013) e65603.
- [187] F. Cao, Z. Shi, G.-L. Song, M. Liu, M.S. Dargusch, A. Atrens, Influence of casting porosity on the corrosion behaviour of Mg0.1Si, *Corrosion Science* 94 (2015) 255-269.
- [188] G. Song, A. Atrens, M. Dargusch, Influence of microstructure on the corrosion of diecast AZ91D, *Corrosion Science* 41(2) (1998) 249-273.
- [189] S. Caines, F. Khan, J. Shirokoff, Analysis of pitting corrosion on steel under insulation in marine environments, *Journal of Loss Prevention in the Process Industries* 26(6) (2013) 1466-1483.
- [190] S.-J.L. Kang, K.-H. Kim, D.N. Yoon, Densification and Shrinkage During Liquid-Phase Sintering, *Journal of the American Ceramic Society* 74(2) (1991) 425-427.
- [191] D. Veljović, R. Jančić-Hajneman, I. Balać, B. Jokić, S. Putić, R. Petrović, D. Janačković, The effect of the shape and size of the pores on the mechanical properties of porous HAP-based bioceramics, *Ceramics International* 37(2) (2011) 471-479.
- [192] B. Chen, Z. Xia, K. Lu, Understanding sintering characteristics of ZnO nanoparticles by FIB-SEM three-dimensional analysis, *Journal of the European Ceramic Society* 33(13) (2013) 2499-2507.
- [193] Z. Xia, B. Chen, K. Lu, 3D microstructure construction and quantitative evaluation of sintered ZrO₂ under different sintering conditions, *Journal of Materials Science* 48(17) (2013) 5852-5861.

- [194] L. Anestiev, L. Froyen, Model of the primary rearrangement processes at liquid phase sintering and selective laser sintering due to biparticle interactions, *Journal of Applied Physics* 86 (1999) 4008-4017.
- [195] N.K. Xydas, L.A. Salam, Transient liquid phase sintering of high density Fe₃Al using Fe and Fe₂Al₅-FeAl₂ powders Part 2 – Densification mechanism analysis, *Powder Metallurgy* 49(2) (2006) 146-152.
- [196] R.M. German, K.S. Churn, Sintering Atmosphere Effects on the Ductility of W- Ni- Fe Heavy Metals, *Metallurgical Transactions A* 15(4) (1984) 747-754.
- [197] D. Ochs, M. Brause, B. Braun, W. Maus-Friedrichs, V. Kempter, CO₂ chemisorption at Mg and MgO surfaces: a study with MIES and UPS (He I), *Surface Science* 397(1) (1998) 101-107.
- [198] J. Hofstetter, E. Martinelli, S. Pogatscher, P. Schmutz, E. Povoden-Karadeniz, A.M. Weinberg, P.J. Uggowitzner, J.F. Löffler, Influence of trace impurities on the in vitro and in vivo degradation of biodegradable Mg-5Zn-0.3Ca alloys, *Acta Biomaterialia* 23 (2015) 347-353.
- [199] P. Oslanec, M. Skrobjan, PECULARITIES OF GAS ANALYSIS IN AL AND MG POWDERS, 2017.
- [200] Y.E. Kalay, L.S. Chumbley, I.E. Anderson, R.E. Napolitano, Characterization of Hypereutectic Al-Si Powders Solidified under Far-From Equilibrium Conditions, *Metallurgical and Materials Transactions A* 38(7) (2007) 1452-1457.
- [201] R. Salomão, V. Pandolfelli, Magnesia Sinter Hydration-Dehydration Behavior in Refractory Castables, *Ceramics International - CERAM INT* 34 (2008) 1829-1834.
- [202] M.P. Harmer, S.J. Bennison, C. Narayan, Microstructural Characterization of Abnormal Grain Growth Development in Al₂O₃, in: D.R. Rossington, R.A. Condrate, R.L. Snyder (Eds.), *Advances in Materials Characterization*, Springer US, Boston, MA, 1983, pp. 309-320.
- [203] J.B. Koo, D.Y. Yoon, Abnormal grain growth in bulk Cu—The dependence on initial grain size and annealing temperature, *Metallurgical and Materials Transactions A* 32(8) (2001) 1911-1926.
- [204] P.R. Rios, Abnormal grain growth in materials containing particles, *Acta Metallurgica et Materialia* 42(3) (1994) 839-843.
- [205] P.R. Rios, Abnormal growth in the presence of coarsening particles, *Acta Metallurgica et Materialia* 40(4) (1992) 649-651.
- [206] A. Tsuge, H. Achiwa, H. Morikawa, M. Uemoto, W. Kanematsu, Determination of Oxygen Content in Magnesium and Its Alloys by Inert Gas Fusion-Infrared Absorptiometry, *Analytical Sciences* 27(7) (2011) 721-721.
- [207] S.-M. Lee, S.-J.L. Kang, Theoretical analysis of liquid-phase sintering: Pore filling theory, *Acta Materialia* 46(9) (1998) 3191-3202.
- [208] H.-H. Park, S.-J. Cho, D.N. Yoon, Pore filling process in liquid phase sintering, *Metallurgical and Materials Transactions A* 15(6) (1984) 1075-1080.
- [209] I. Amato, The effect of gas trapped within pores during sintering and density regression of ceramic bodies, *Materials Science and Engineering* 7(1) (1971) 49-53.
- [210] J.L. Johnson, J.J. Brezovsky, R.M. German, Effects of tungsten particle size and copper content on densification of liquid-phase-sintered W-Cu, *Metallurgical and Materials Transactions A* 36(10) (2005) 2807-2814.
- [211] M. Alvarez-Lopez, M.D. Pereda, J.A. del Valle, M. Fernandez-Lorenzo, M.C. Garcia-Alonso, O.A. Ruano, M.L. Escudero, Corrosion behaviour of AZ31 magnesium alloy with different grain sizes in simulated biological fluids, *Acta Biomaterialia* 6(5) (2010) 1763-1771.

- [212] G.B. Hamu, D. Eliezer, L. Wagner, The relation between severe plastic deformation microstructure and corrosion behavior of AZ31 magnesium alloy, *Journal of Alloys and Compounds* 468(1) (2009) 222-229.
- [213] H. Wang, Y. Estrin, H. Fu, G. Song, Z. Zúberová, The Effect of Pre-Processing and Grain Structure on the Bio-Corrosion and Fatigue Resistance of Magnesium Alloy AZ31, *Advanced Engineering Materials* 9(11) (2007) 967-972.
- [214] W.-C. Kim, J.-G. Kim, J.-Y. Lee, H.-K. Seok, Influence of Ca on the corrosion properties of magnesium for biomaterials, *Materials Letters* 62(25) (2008) 4146-4148.
- [215] J.W. Seong, W.J. Kim, Development of biodegradable Mg–Ca alloy sheets with enhanced strength and corrosion properties through the refinement and uniform dispersion of the Mg₂Ca phase by high-ratio differential speed rolling, *Acta Biomaterialia* 11 (2015) 531-542.
- [216] Y.S. Jeong, W.J. Kim, Enhancement of mechanical properties and corrosion resistance of Mg–Ca alloys through microstructural refinement by indirect extrusion, *Corrosion Science* 82 (2014) 392–403.
- [217] D. Mei, S.V. Lamaka, J. Gonzalez, F. Feyerabend, R. Willumeit-Römer, M.L. Zheludkevich, The role of individual components of simulated body fluid on the corrosion behavior of commercially pure Mg, *Corrosion Science* 147 (2019) 81-93.
- [218] J.-Y. Jung, S.-J. Kwon, H.-S. Han, G.F. Yang, J.-Y. Lee, S.-J. Yang, S.-Y. Cho, P.-R. Cha, Y.-Y. Kim, Y.-C. Kim, H.-K. Seok, J.-P. Ahn, Rapid In Vitro Corrosion Induced by Crack-Like Pathway in Biodegradable Mg–10% Ca Alloy, *Microscopy and Microanalysis* 19(S5) (2013) 210-214.
- [219] R. Kainuma, I. Ohnuma, K. Ishida, Dragging of Liquid Bi Particles Induced by Grain Boundary Migration in Al-Bi Alloys, *MATERIALS TRANSACTIONS* 44(9) (2003) 1768-1773.
- [220] B. Young-Joon, D.N. Yoon, Migration of liquid film and grain boundary in Mo-Ni induced by temperature change, *Acta Metallurgica* 33(10) (1985) 1911-1917.
- [221] M.F. Ashby, R.M.A. Gentamore, The dragging of small oxide particles by migrating grain boundaries in copper, *Acta Metallurgica* 16(9) (1968) 1081-1092.
- [222] T. Davis, D. Healy, A. Bubeck, R. Walker, Stress concentrations around voids in three dimensions: The roots of failure, *Journal of Structural Geology* 102 (2017) 193-207.
- [223] E.-J. Lee, Y.-H. Koh, B.-H. Yoon, H.-E. Kim, H.-W. Kim, Highly porous hydroxyapatite bioceramics with interconnected pore channels using camphene-based freeze casting, *Materials Letters* 61(11) (2007) 2270-2273.
- [224] R.-C. Zeng, W.-C. Qi, H.-Z. Cui, F. Zhang, S.-Q. Li, E.-H. Han, In vitro corrosion of as-extruded Mg–Ca alloys—The influence of Ca concentration, *Corrosion Science* 96 (2015) 23-31.
- [225] W. Qudong, C. Wenzhou, Z. Xiaoqin, L. Yizhen, D. Wenjiang, Z. Yanping, X. Xiaoping, M. Mabuchi, Effects of Ca addition on the microstructure and mechanical properties of AZ91magnesium alloy, *Journal of Materials Science* 36(12) (2001) 3035-3040.
- [226] Y. Chino, M. Kobata, H. Iwasaki, M. Mabuchi, Tensile Properties from Room Temperature to 673 K of Mg-0.9 mass%Ca Alloy Containing Lamella Mg₂Ca, *MATERIALS TRANSACTIONS* 43(10) (2002) 2643-2646.
- [227] Y. Chino, K. Sassa, M. Mabuchi, Enhancement of tensile ductility of magnesium alloy produced by torsion extrusion, *Scripta Materialia* 59(4) (2008) 399-402.
- [228] J. Koike, Enhanced deformation mechanisms by anisotropic plasticity in polycrystalline Mg alloys at room temperature, *Metallurgical and Materials Transactions A* 36(7) (2005) 1689-1696.

- [229] C.M. Murphy, M.G. Haugh, F.J. O'Brien, The effect of mean pore size on cell attachment, proliferation and migration in collagen–glycosaminoglycan scaffolds for bone tissue engineering, *Biomaterials* 31(3) (2010) 461-466.
- [230] B. Otsuki, M. Takemoto, S. Fujibayashi, M. Neo, T. Kokubo, T. Nakamura, Pore throat size and connectivity determine bone and tissue ingrowth into porous implants: Three-dimensional micro-CT based structural analyses of porous bioactive titanium implants, *Biomaterials* 27(35) (2006) 5892-5900.
- [231] T. Dutta Roy, J.L. Simon, J.L. Ricci, E.D. Rekow, V.P. Thompson, J.R. Parsons, Performance of hydroxyapatite bone repair scaffolds created via three-dimensional fabrication techniques, *Journal of Biomedical Materials Research Part A* 67A(4) (2003) 1228-1237.
- [232] I. Bružauskaitė, D. Bironaitė, E. Bagdonas, E. Bernotienė, Scaffolds and cells for tissue regeneration: different scaffold pore sizes—different cell effects, *Cytotechnology* 68(3) (2016) 355-369.